HIGH POWER LITHIUM ION BATTERY CHARACTERIZATION

By

Mitchell Gregory
Candidate MASc. Mechanical Engineering
Mt233244@dal.ca
B00773084

Submitted in partial fulfilment of the requirements for the degree of Master of Applied Science

at

Dalhousie University
Halifax, Nova Scotia
December 2024

Dalhousie University is located in Mi’kma’ki, the
ancestral and unceded territory of the Mi’kmaq.
We are all Treaty people.

Table Of Contents

List of Tables

List of Figures

Abstract

Lithium-ion batteries used for motive transport applications need to reliably charge at ultra high charge rates below 10 minutes. Charge performance testing data mapped across the usable range of temperature and charge rate is required to make informed decisions in multiple battery system developmental phases including cell selection, battery management system parameterization, thermal management system design, and charge profile selection. Ultra fast full charging requires new cell characterization techniques due to the high heat generation. This thesis develops and demonstrates techniques used for parameterizing high-power lithium-ion battery cells in 21-70 cell format. Molicel P45B cells are dissected and geometries of internal components such as electrode, current collector, and tab geometry are measured to confirm high power cell design. Electrode chemical composition of active materials was analysed using inductively coupled plasma, computed tomography, and scanning electron microscopy techniques. Cells are cycled at high charge rate in traditional air chamber and in isothermal conditions to identify differences in parameterization results. A T-type thermocouple was inserted and sealed into the center of the cell core which provided direct measurement of inner jellyroll wall. Cell core to wall temperature gradients are evaluated in both conditions. An 8 ˚C core to wall temperature difference was measured during 20-minute fast charge. A novel cell holder and high-rate cell cycler are used to cycle cells in a range of isothermal wall temperatures and rates to parameterize properties and quantify operational trade-offs. The affect of applying temperature profiles during cycling is investigated using multiple profiles and showed that elevated constant voltage stage charge temperatures reduced charge time significantly. Relationships quantifying key cell cycle metrics with respect to the temperatures range of 25 to 55 ˚C and charge rates from 1 hour to 5 minutes were experimentally quantified. The techniques developed in this study support future experimental performance comparisons of degradation response to different electrical and thermal conditioning profiles.

List of abbreviations, acronyms, symbols, and units

Term	**Description**
ATM	Asymmetrical Temperature Modulation
BMS	Battery Management System
CID	Current Interrupt Device
C-rate	Discharge current / nominal discharge capacity
DOE	Design Of Experiments
EV	Electric Vehicle
IR	Internal Resistance
LIB	Lithium-ion Battery
LFP	Lithium Iron Phosphate
NCA	Nickel Cobalt Aluminum
NMC	Nickel-Manganese-Cobalt
RESL	Renewable Energy Storage Laboratory
RPT	Reference Performance Testing
RTG	Radial Temperature Gradient
SOCΔ	State of Charge Delta
TMS	Battery Thermal Management System
T_{core}	Cell core temperature, ˚C
T_{wall}	Cell wall temperature, ˚C
XFC	Extreme Fast Charge

Acknowledgement

I would like to thank my supervisor Dr. Lukas Swan for his mentorship, guidance, and for providing me with this tremendous experience.

Thanks to Litens Automotive Group of Ontario who provided invaluable research inspiration, critical testing equipment, and financial support. It was my pleasure to collaborate with Andrew, Sean, and their team from Litens. Funding for this work was provided by an NSERC Alliance Grant in partnership with Litens Automotive Group.

This work would not have been possible without the RESL team and Dalhousie battery research community who have inspired me to dig deeper and ask big questions. Dan Baker at the Dalhousie Minerals Engineering Laboratory helped with material analysis. Eric Moreau from the Dalhousie Engineering Scanning Electron Microscopy – Focused Ion Beam (SEM-FIB) Facility helped with CT scanning.

Extra special thanks to my family and partner Jo for support along the way.

Chapter 1 Introduction

Lithium-ion batteries are becoming widely used for transportation applications. Although ultra fast charging can add upwards of 200 km of range in 5 minutes, vehicle battery cells and thermal systems are stressed in the process. New techniques are needed to evaluate the chemical, physical, and electrochemical properties of high-power battery cells and their impact on fast charging performance. Ultra high current testing is different than conventional techniques because considerations need to be made for thermal, electrical, and chemical non-uniformities. Above all, the most important parameter is cell temperature because the key metrics of cell resistance, energy efficiency, degradation, and safety are highly dependent on it. Rapid charging batteries causes substantial heat generation within the cell which can cause the cell to reach the upper temperature limit (Often 60 ˚C). System designers must be able to identify and select the optimal temperature and charge current profiles to minimize charge time. Understanding how key performance metrics are influenced by temperature and charge rate are needed to select an optimal charging condition.

Control over cell temperature throughout the charging session is critical to maintain ideal operational conditions. The high heat generation during charging requires high heat transfer capabilities. In early model electric vehicles, fast charging a battery has been shown to reduce battery life, especially in hot environments (Myall, 2018). In the case of the Nissan Leaf, passively cooled architecture did not support successive fast charges. However, modern vehicles are better equipped to manage effects of fast charging. More powerful cooling systems such as those utilizing immersion heat transfer methods have potential for maintaining ideal temperature and temperature uniformity conditions under high heat generation rates. Immersion cooling is more powerful because pumping dielectric oil through a container holding cells results in very high convective heat transfer rates compared to other methods. Development of high heat transfer rate thermal control systems provides the motivation for this thesis to develop techniques for parameterizing high-power batteries and rapidly identify their ideal charge condition. Furthermore, rapid characterization techniques are instrumental in supporting battery system developers comparing and selecting cells for tailored applications.

1.1 Fast charging strategies

Numerous fast charge capable commercial vehicles are available on the market with battery usable energy ranging from 80 kWh to 1 MWh (Al-Hanahi, 2021). In recent years, direct current fast chargers (DCFC) have been deployed in high traffic areas around the world with a general trend of increasing power capabilities (Tu, 2019). The term extreme fast charge (XFC) has been used to describe charging at 400 kW (Michelbacher, 2017). Additional standards focused on heavy duty truck charging at the megawatt level are under development as described by the J3271 standard (SAE, 2021). During a fast-charging session, the power a single cell experiences is dependant on the battery pack configuration, defined operational window, and selected charge profile. The vehicle battery management system (BMS) communicates a maximum charge current limit to the charger through the connector as defined by standards such as IEC 61851-1 and ISO 15118 (Suarez, 2019). Simultaneously, the BMS also controls the thermal management system (TMS) to maintain battery temperature to a setpoint. The selected electrical and thermal profiles used throughout a charge session is of key importance to optimizing charge time, battery longevity, and safety. Vehicle thermal and electrical limitations are now commonly constraining the charge rate instead of the charger itself**.** Thus, improved charge times can be obtained by developing battery systems capable of making use of all available XFC charger power.

Developing fast charge capable batteries requires knowledge of the ideal cell operational window and optimized control over electrical and thermal conditions. Cell level charge limitations are inevitable and can be attributed to resistance, lithium plating, and temperature limits. Recent efforts to improve battery fast charging capabilities focus on a few key areas including cell current collector and tab resistance, ion diffusion in active materials, charge transfer dynamics with electrolyte salts, and increasing temperature limits. The use of multiple tabs or tab-less designs has reduced ohmic resistance. Electrode design using advanced coatings, fine particles, and low tortuosity has reduced cell ionic resistance. Analysis of salt depletion/saturation in electrodes has informed electrolyte design and supported reduced charge transfer resistance. Experimentation with electrolyte solvents and additives has increased maximum temperature limitations. Although numerous studies have demonstrated the individual impact of each design variable, quantifying commercially available cell level performance is fundamental to cell selection and system design.

Beyond cell design, the electrical and thermal profiles during a charge have been shown to significantly impact charge performance (Teng Liu, 2021). Many of the improvements have been demonstrated with laboratory scale half cells, coin cells, or small format pouch cells (Bandhauer, 2011). There is a need for commercial scale cell format ultra fast charge characterization techniques with both electrical power and cell temperature profile analysis. One difficulty with increasing cell size is managing the heat generation and presence of thermal gradients within larger format cells. Evaluation of internal temperature gradients is needed to ensure safety and longevity of large format cells.

Improved test apparatuses are needed to fully map the performance profile of fast charging lithium-ion cells with respect to cell temperature and rate. Forced air thermal chambers have been commonly used to cycle cells in an isoperibolic convective heat transfer condition. As higher power charging is employed, charge rate limitations associated with methods utilizing convection based thermal chambers limits the parameterizable operational window of cells due to their inability to maintain cell temperature. The use of convection to control temperature leads to a significant difference between the surface of the cell and the chamber set point which contributes to substantial cycle life and single cycle performance differences (Landini, 2022). The difference from setpoint is further exacerbated by the presence of a radial temperature gradient (RTG) from cell core to wall during cycling. Internal cell temperature is higher than the external cell temperature during heat rejection due to internal heating throughout the jellyroll. Measurement of the cell internal temperature is needed to inform charge rate limitation analysis. Figure 1 illustrates the location of cell core temperature and cell wall temperature locations.

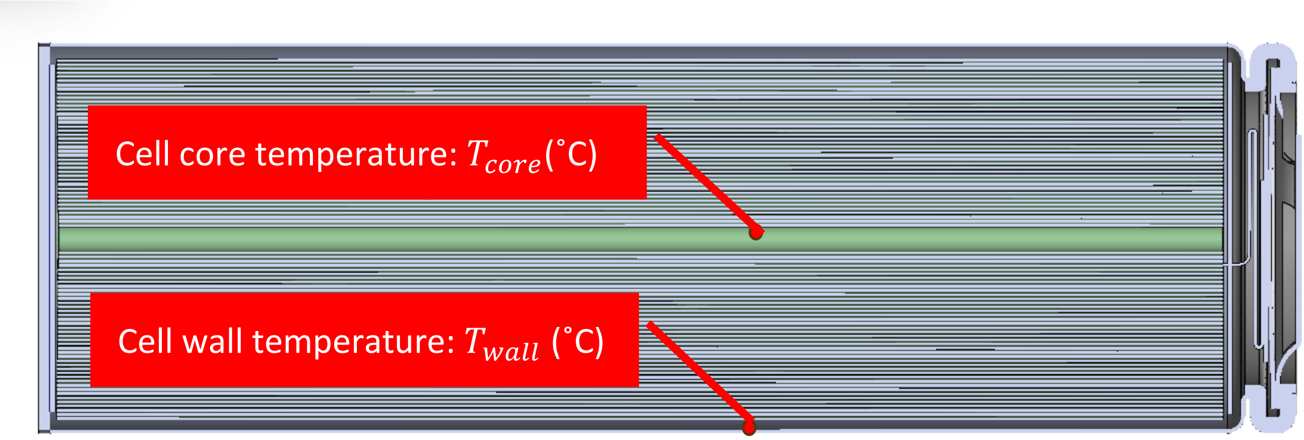

Figure 1 Axial Cross section of 21-70 cell core and cell wall temperature locations.

Pre-conditioning is when a TMS is used to increase cell temperature prior to a charge session to place the cell in the ideal temperature regime. Advanced thermal profiles require rapid cell temperature changes especially during thermal pre-conditioning. Currently, indirect heat transfer methods such as channel or plate cooling are widely used to transfer heat. However, the heat transfer power of indirect methods is limited due to thermal resistances and manufacturing capabilities. Active conduction based thermal controllers using peltier elements are an improved technique to maintain the isothermal wall condition. An isothermal cell holder also provides the ability to measure the heat transfer required to maintain temperature which can inform heat transfer system design especially as to when throughout the cycle heat is generated. Quantifying the heat transfer required to maintain temperature under different conditions supports selection and design of heat transfer mechanisms. In this study, a novel isothermal cell holder with high power thermal control is used to evaluate the charging performance of high-power batteries.

1.2 Research approach

This study focuses on developing techniques to characterize cell fast charge performance in isothermal conditions using the commercially available Molicel P45B cylindrical 21-70 cell with NCA/Graphite chemistry. This cell was selected due to its high-power cell design and relevance to multiple existing commercially available vehicles.

New cells were dissected and analysed with a scanning electron microscope (SEM) to visualize electrode design and condition. Electrode material was analysed with inductively coupled plasma mass spectrometry (ICP) to determine chemical composition. The general physical construction of the cells was also measured to provide a basis for comparing to theoretical current, capacity, and energy limitations.

Charge performance results for different electrical and isothermal wall conditions were compared. Instantaneous and cycle specific key metrics are compared over a state of charge (SOC) range of 0 – 100 % while charging at rates ranging from 1 hour (slow) to 5 minutes (ultra fast) and in isothermal temperature conditions ranging from 25 ˚C to 60 ˚C. Full 0-100 % SOC cycling at various rates and isothermal temperatures enables investigating the relationship between key metrics of charge rate, temperature, coulombic efficiency, energy efficiency, and capacity as a function of condition. The resulting 3-dimensional surfaces for each metric provides insight into incremental change in performance for increasing charge rate or temperature. The surfaces support the definition of a cell power operational envelope and help identify an ideal charging temperature range.

Asymmetric temperature profiles were applied during cycling to quantify how increasing temperature at different times throughout a charge cycle impacts the charge performance. Step change thermal profiles were used to increase cell temperature by 20 ˚C within 1 minute at three different times during a charge. The results demonstrate how important and when it is important that the cell temperature be elevated.

A thermocouple temperature sensor was inserted into the cell core to provide a measurement for comparing cell internal to external wall temperature during cycling. The location and effect of probe insertion on current collectors was investigated with computed tomography (CT) scanning. Probed cells were subjected to three charge rates and four temperature conditions to characterize thermal gradients and core temperature when cycled in the convection condition and in the isothermal condition.

In summary, this study aims to develop and demonstrate methods to thoroughly and rapidly characterize lithium-ion cell performance while subject to ultra fast charging. The results provide new information on cell internal temperature and key metric performance during isothermal and convection condition fast charging. This study does not include testing and analysis of lithium plating or degradation.

Results of characterization may be used in cell selection, to define safe thermal and electrical operational windows, and to select thermal and electrical profiles which optimize battery charge performance.

This study aims to:

1. Quantify chemical, physical, and electrochemical properties of Molicel P45B 21-70 cell to connect electrochemical cycling trends with physical design.
2. Measure internal temperature during fast charging in both isothermal and isoperibolic conditions to evaluate how internal temperature depends on charge rate.
3. Compare key metrics during charging in novel isothermal cell holder to quantify cell performance and identify optimal charge profile.
4. Evaluate the impact of thermal profile on charge performance to identify affect of rapid pre-conditioning on charge time.

Chapter 2 Literature review

This chapter will explore numerous concepts pertinent to fast charging lithium-ion battery such as cell design and electrochemical relationships. The impact that battery design properties including electrode chemistry, physical geometry, and current collector design has on fast charging capability is contextualized with support from classical physics-based models. Heat generation and internal to cell heat transfer is discussed. Finally, the impact of BMS controlled thermal and electrical profiles on charge performance is presented. This chapter concludes with a summary of key research points.

2.1 Internal temperature, heat generation, and heat transfer

The impact of cell internal temperature on cell performance is significant. The internal temperature evolution during cycling is fundamentally related to its own heat generation and heat transfer conditions. This chapter outlines the physical and electrochemical relationships which describe heat generation, heat transfer, and discusses techniques for measuring internal temperature.

2.1.1 Internal temperature

Measurement of cell internal temperature is difficult because the technique used must not significantly interfere electrochemically or it may alter heat generation and internal temperature. Even in isothermal wall conditions, cell internal temperature increases during fast charges due to heat generation in the electrode stack. In practice, high-rate cycling can result in a substantial temperature difference (e.g. 5+ ˚C) between the internal and external surface (Amietszajew 2018). Previous methods to estimate or measure internal temperature have used Electrical Impedance Spectroscopy (EIS) (Ezahedi, 2024), fiber Bragg grating (FBG) (Yang G. L., 2013), resistance temperature detectors (RTD) (Vincent, 2021), and thermocouples (Gulsoy, 2022). Figure 2 illustrates the four methods mention above.

Method	Diagram	Source
A) EIS	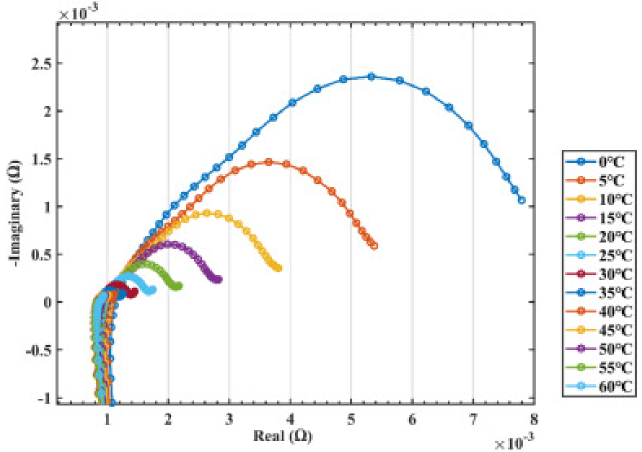	(Ezahedi, 2024)
B) FBG	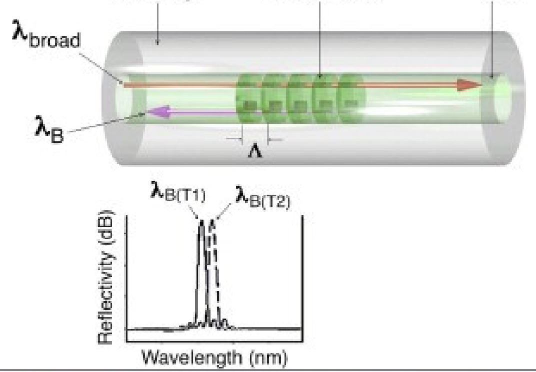	(Yang G. L., 2013)
C) RTD	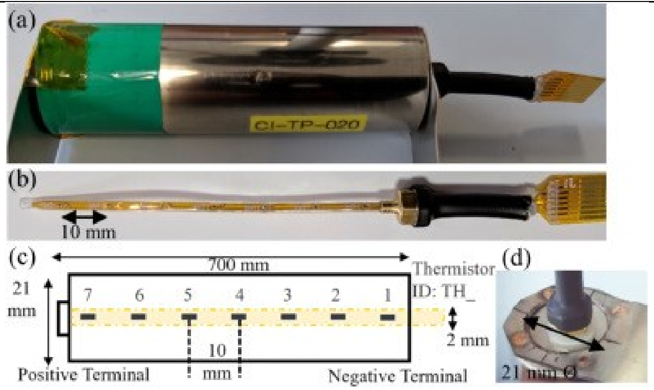	(Vincent, 2021)
D) Thermocouple	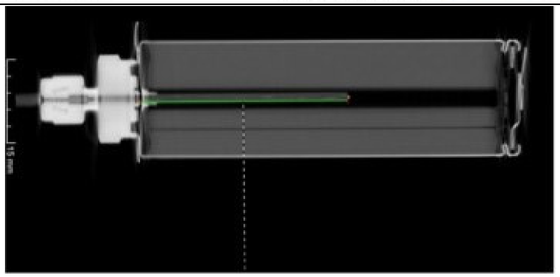	(Gulsoy, 2022)

Figure 2 Methods for measurement of internal temperature.

The EIS method uses correlation of internal temperature and impedance to estimate the cell internal temperature. The EIS method is notable for being the only method which does not require insertion of a sensor. However, EIS does require substantial calibration and is not directly measuring the cell temperature. Fiber Bragg method uses an optical fiber which is sensitive to temperature. FBGs are extremely narrow (~100µm diameter) immune to electromagnetic interference, are non-conductive and chemically inert. FBGS are highly accurate but require extensive equipment for signal processing. RTD and Thermocouple are lower cost simplistic methods. RTD use ultra fine platinum wound wire or surface plated platinum to create a temperature dependant resistor which is easily measured and correlated to temperature. Thermocouples operate on the Seeback Effect. When the junction of two dissimilar metal wires is heated, measurement of temperature dependent voltage can be achieved at the opposite end of the dissimilar metal wires. Thermocouples are generally smaller than RTD which can help with minimizing impact on the cell.

The measurement accuracy and precision required for internal temperature sensing depends on the end use of the data. In this work, temperature measurement is used for comparing the internal to external wall temperature. Thus, the 0.5 ˚C uncertainty associated with thermocouple measurement techniques is acceptable. If internal temperature measurements were used for calculating heat generation, then far higher accuracy is required.

2.1.2 Heat generation

Internal heating during charge and discharge comes from two sources, reversible and irreversible heating. Irreversible heating is comprised of heat generated from ohmic, kinetic, and mass transport sources. Ohmic sources include heat generated from electron movement in the electrodes and current collectors and includes ion transport through the solid electrolyte interphase (SEI), electrolyte, and separator. Kinetic heating comes from charge transfer interactions associated with ion intercalation into active material particles. Mass transport heating is associated with ion transport within the electrode and contributes to nonlinear cell resistance and heating at high rates. For modeling purposes, each of the irreversible heating components can be lumped into a single resistance term. Figure 3 shows the different resistances to ion transport present within the cell stack.

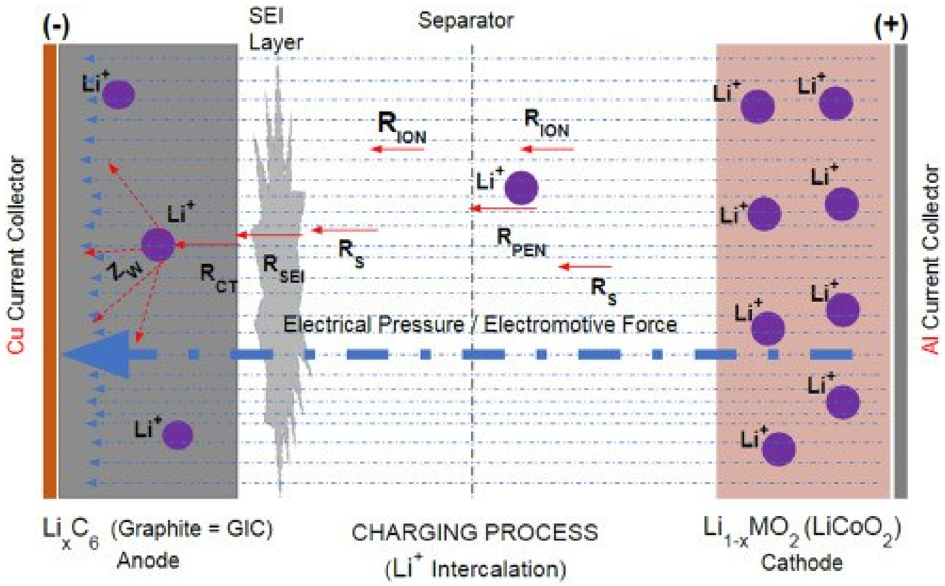

Figure 3 Resistance to charging a battery. Adapted without modification (Thusitha, 2022)

Table 1 defines the resistances present when charging a battery.

Table 1 Cell resistance

Symbol	Name
R_{ION}	Ionic resistance
R_S	Solution resistance
R_{CT}	Charge Transfer resistance
R_{PEN}	Penetration resistance
R_{SEI}	Solid Electrolyte Interphase resistance
Z_W	Warburg resistance (Diffusion)

The total cell resistance is the sum of all resistances depicted in Table 1. Irreversible heat is modeled using the product of current (I) squared and resistance (R_{tot}).

$$Q_{Irr} = I^2 R_{tot} \tag{1}$$

The resistance term is highly dependant on SOC and moderately dependant on temperature. At low to moderate charge rates (<1 hour charge) and constant temperature, resistance is stable throughout the charge session until approaching the end of charge where it increases. Near fully charged, charge transfer and diffusion resistance increase due to the electrodes nearing their filled/empty state and saturation effects. Total cell resistance reduces with increasing temperature. Increasing temperature increases diffusion in the electrodes.

Reversible heating occurs in the electrodes due to reversible material phase transitions. Reversible heating exhibits endothermic and exothermic behavior depending on the direction of charge and state of charge. The reversible heat, given in equation 2, is modeled with the state of charge dependant entropy coefficient $\left(\frac{dU}{dT}\right)$ which is determined by the change in open circuit voltage (dU) over the change in temperature (dT).

$$Q_{rev} = -IT\,\frac{dU}{dT} \tag{2}$$

The entropy coefficient has been shown to be heavily state of charge dependant (Minseok, 2022). In lithium-ion batteries, reversible heating phenomenon is net exothermic on charge and net endothermic on dis-charge (Bedürftig, 2021). However, both charging and discharging have exothermic and endothermic stages. Figure 4 shows the dependency of entropy coefficient on state of charge and its evolution over cycling. Endothermic reversible effect has been shown to absorb the irreversible heat generation at low charge rates (4 hour) (Cheng, 2021).

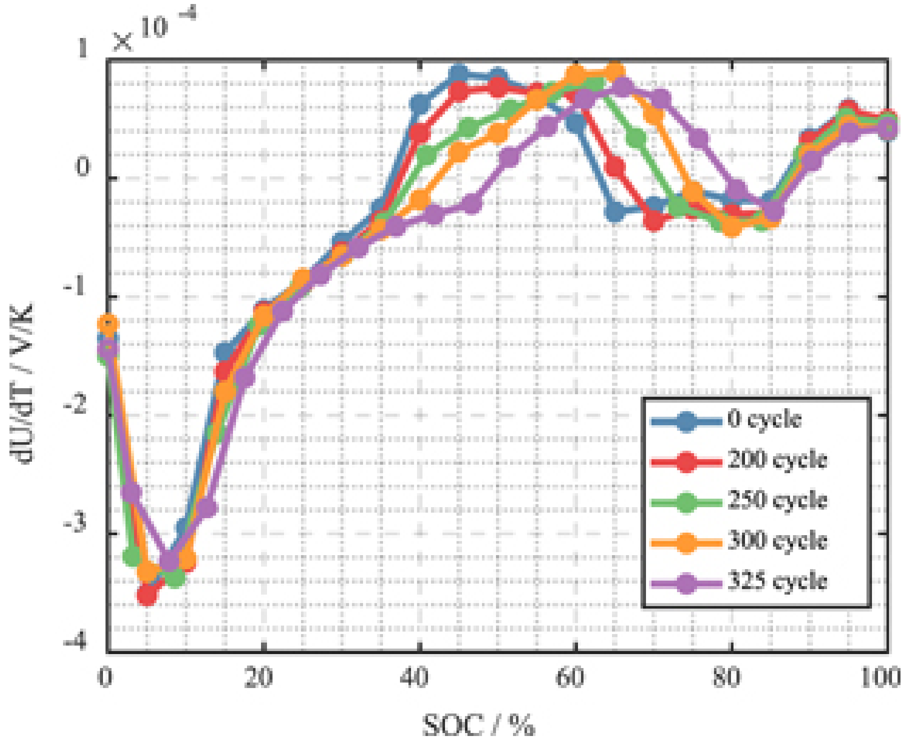

Figure 4 Entropy coefficient as a function of state of charge vs cycles (Minseok, 2022)

Total heat generation is the sum of reversible and irreversible heat components is given in Equation 3.

$$Q_{Tot} = Q_{rev} + Q_{Irr} = I^2 R_{tot} - IT\,\frac{dU}{dT} \tag{3}$$

The main variables contributing to the heat generation are therefore current (I), resistance (R), temperature (T), and entropy coefficient ($\frac{dU}{dT}$). The irreversible heat generation dominates reversible heat generation during high charge rates.

One key metric for quantifying cell heat generation is the energy efficiency. Because full cycle energy efficiency does not provide information on instantaneous heat generation, other methods for evaluating heat generation are needed. Full cycle energy efficiency for NCA/graphite chemistry is very high (>95 %) at low rates (<1C), especially for high power cells (Edoardo, 2021). To achieve high energy efficiency at high rates, low resistance electrodes are needed. Heat generation in cylindrical cells has been evaluated in literature with model-based and direct measurement methods. Most model-based techniques use a variation of the pseudo-two-dimensional (P2D) or an equivalent circuit model and operate using established thermally coupled electrochemical relationships (Eze, 2024). Calculation of cell heat generation and other cell states over time is achieved using measured properties such as cell resistance, entropy coefficient, and cell physical properties such as electrode thickness and chemistry. Verification of models is often achieved by comparing calculated temperature versus measured cell temperature over different cycling conditions.

2.1.3 Heat transfer

Maintaining isothermal cell conditions during cycling requires heat transfer. Heat transfer is driven by the internal cell temperature deviating from the wall temperature. Heat transfer can be analysed from internal or external to the cell. Internal analysis is focused on thermal gradients throughout the jellyroll and current collectors. External heat transfer is focused on heat flow to and from the surface of the cell.

Externally, the highest performing options for transferring heat to and from the cell include cooling plate, microchannel extrusion, and immersion cooling. Authors have studied a range of heat transfer mechanisms for the 21-70 cell format (Dubey, 2021; Ahmadian-Elmi, 2024). Other methods which are not used at scale but have been widely reported on include forced air and heat pipes. Figure 5 illustrates commonly used cylindrical cell cooling methods where the blue colour distinguishes coolant pathways.

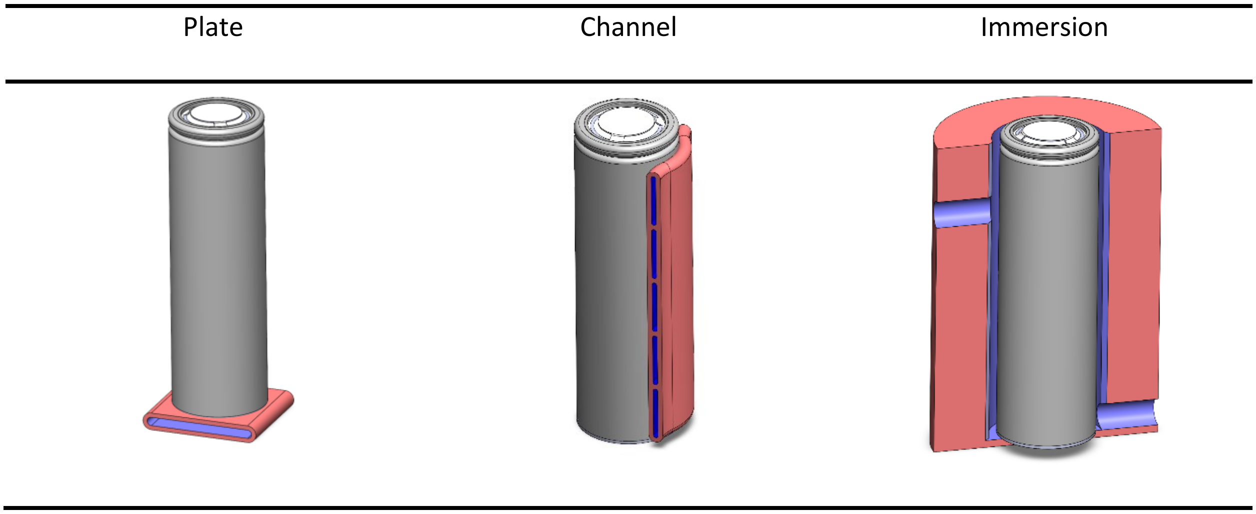

Figure 5 Heat transfer methods used for 21-70 cell

Microchannel extrusion and cooling plates rely on conduction of heat through the cell, through channel material (often aluminium), and into the heat transfer fluid (often glycol/water with additives). The reliance on a long conduction path and presences of multiple material interfaces limits heat transfer in comparison to immersion cooling where the heat transfer fluid is in direct contact with the cell wall. Such limitations to heat transfer contribute to temperature gradients both axially and radially.

Internally, the high thermal conductivity of the copper and aluminum current collectors transfer heat well axially. However, heat transfer through the radial direction is limiting due to the separator placement between the electrodes. Full cell radial and axial thermal conductivity was measured to be 0.83 W/mK and 6.93 W/mK respectively (Todys, 2020). Although axial temperature gradients are present, the lower radial conductivity results in a predominant radial temperature gradient from jellyroll center to cell wall during natural convection cooling.

Each heat transfer method leads to differing temperature gradients. Li modeled temperature evolution during 20 minute discharge for top/base and side cooling and found that side cooling results in a predominantly radial gradient whereas top/base cooling results in an axial gradient (Li R. L., 2022). The resulting gradients contribute to uneven electrode wear and localized hotspots especially at high charge rates. Furthermore, charging at high rates with gradients present can cause accelerated degradation (Carter, 2021). Figure 6 illustrates battery temperature gradients expected with plate and channel cooling.

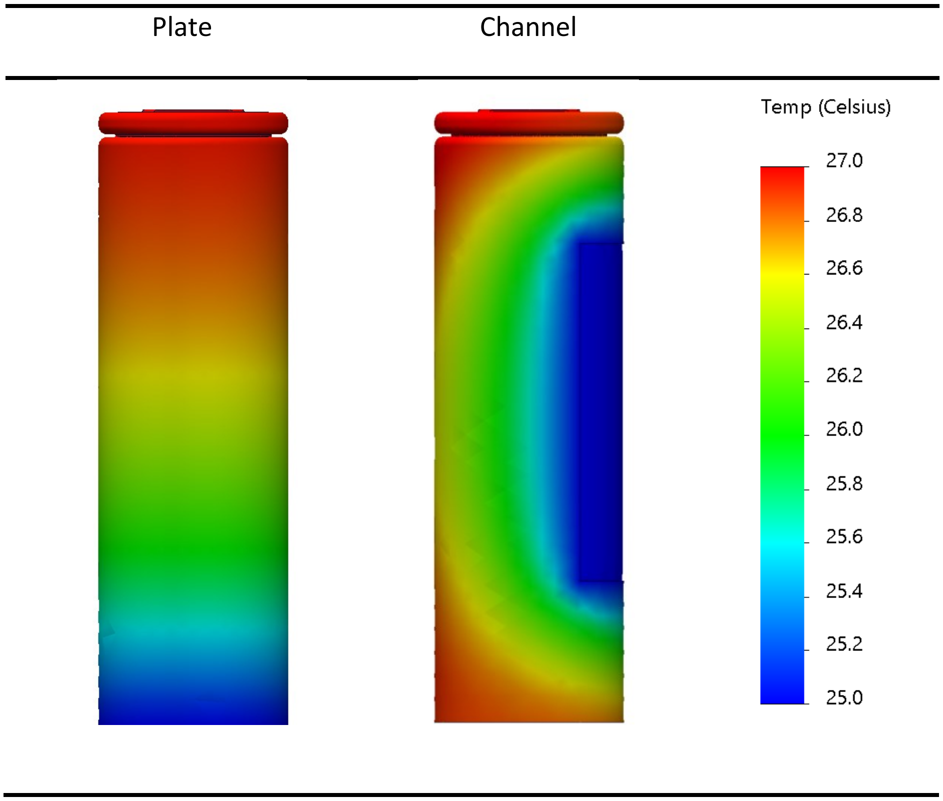

Figure 6 Simplified cross-sectional temperature gradient for plate and channel cooling. Based on with modification from (Li S. K., 2021)

The immersion cooling method is widely regarded as the superior heat transfer method for maximum heat transfer capability (Thakur, 2023). It is expected that gradients in immersion cooling systems are similar to the side cooling method where the cell wall temperature is maintained, and the dominant gradient is from cell internal to cell wall. Very rapid heat transfer capabilities provide the system improved control over cell temperature which achieves conditions approaching near isothermal wall temperatures.

2.2 Cell design and selection considerations

The 21-70 cell format can be assembled with any lithium-ion chemistry without major physical changes to the cell design. The main components within the cell include electrodes, current collectors and tabs, and electrolyte.

Figure 7 shows the cell internal components and their locations within the cell.

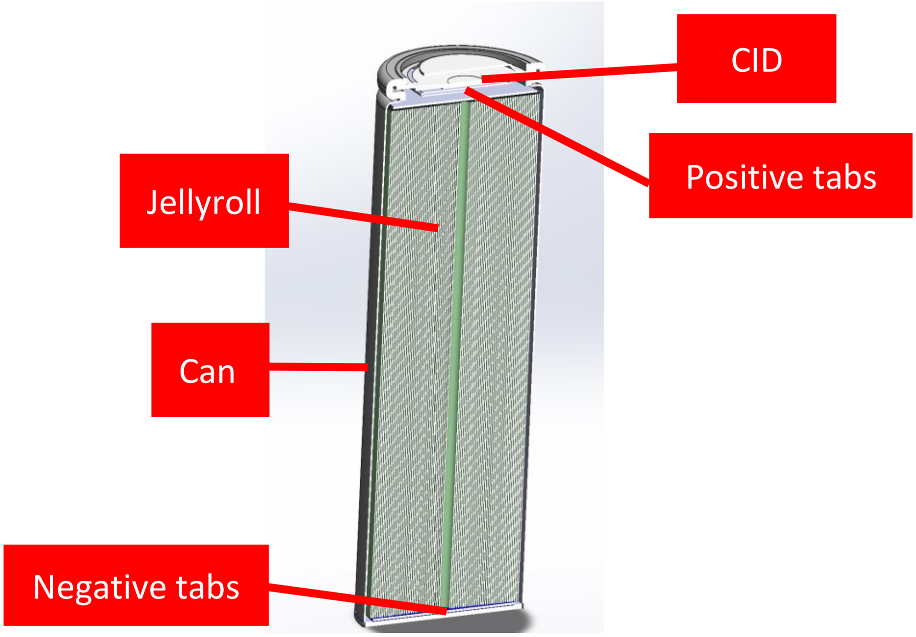

Figure 7 Cell internal component locations

Cell design significantly impacts the ideal operational temperature, current, and voltage required for minimizing charge time because small differences in design and material properties can contribute to charge rate limiting conditions. Alterations to the chemistry or the electrode geometry, current collector, and tab thickness can significantly affect the energy density, power capabilities, internal resistance, voltage profile, lifespan, and more. Thus, quantifying the exact physical and chemical design of a cell to be studied is important to provide context when comparing to other cells. Key controllable design variables are discussed in the following sections.

2.2.1 Electrodes

Electrode material selection and design is the most critical feature defining cell power capabilities. Selection of electrode loading, loading ratio, particle size, and coatings each have considerable impact on overall cell power and energy capabilities. Major electrode properties will be defined and discussed below.

2.2.1.1 Active material and precursors

Selection of electrode active materials and their design properties can be used to tailor a cell to a specific charge rate and energy requirements. The negative electrode is crucially important with respect to fast charging because it is where lithium plating occurs. In most lithium-ion cells, the negative electrode active material is a carbon-based powder adhered with a binding agent such as polyvinylidene fluoride (PVDF), and acetylene black. This combination has proven to be safe, reliable, low cost, and have high cycling stability.

Traditional precursor materials for graphite anodes are hard or soft carbons. Hard carbons are sourced from organic compounds such as resin, or lignin, where soft carbons are sourced from petroleum products such as pitch-derived coke. In the past, soft carbons have been preferred for use in battery anodes due to their ability to form crystalline graphite readily through heat treatment processes. On the commercial scale easy to graphitize material such as soft carbon remain the most widely used. However, other candidates such as carbon microspheres, hard carbon based, silicon, or hybrid combination are alternatives (Kumar, 2023). Hard carbon materials show promise in fast charge applications because their unordered turbostratic structure has low resistance at the cost of low specific capacity (Gottschalk, 2023). Titanium oxide coated carbon microspheres formed using advanced heat treatment and processing of soft carbons have been increasingly used but have additional steps to produce and are thus the more costly alternative (Hyeon, 2022). Hyeon Found that an experimental anode consisting of titanium oxide coated carbon spheres maintained 67% capacity at 20 C compared to 0.5 C and retained 83 % capacity after 1000 cycles (Hyeon, 2022). Silicon anodes have extremely high theoretical capacity (∼4200 mA h g^{-1}) (Sehrawat, Recent trends in silicon/graphene nanocomposite anodes for lithium-ion batteries. , 2021). However, achieving over 1000 cycles with pure silicon anode has not been shown in literature due to the extreme SOC dependant particle expansion (Delong Ma, 2014).

The most common positive active materials are Lithium Iron Phosphate (LFP), Nickel Manganese Cobalt (NMC) and Nickel Cobalt Aluminum (NCA) (Kraft, 2021). The elevated specific capacity of high nickel content NCA chemistries may provide justification for using charge rate increasing design choices (multiple tabs, coatings, high binder content) which tend to reduce overall capacity.

2.2.1.2 Loading and loading ratio

Electrode loading is known to be strongly related to cell power capability. Electrode loading, expressed in $\mathrm{Ah/cm^2}$ is determined by active material thickness, density, and specific capacity. The loading ratio is the ratio of loaded negative active material to positive active material. Low power cells may be designed with a loading ratio (N/P) of 1.1 whereas high power cells may have a loading ratio near 1.2. Increasing the loading ratios reduces cell energy density. Tuning the loading ratio of is known to contribute to a reduction in lithium plating risk (Zhang, 2020). Constructing cells with more negative active material results in less chance of plating because the negative electrode is at a greater voltage throughout the charge process. Active material thickness ratio is analogous to the loading ratio but is impacted by variance in material properties and calendaring. Electrode thickness can range from 30 µm for thin electrodes up to 250 µm for thick electrodes (Singh, 2022). Thin electrodes are more powerful because they have reduced electrolyte gradients, shorter ion transport path, improved diffusivity (Wenlong Xie, 2024). Thick electrodes contribute to high overpotential and concentration gradients (Tomaszewska 2019).

2.2.1.3 Electrode composition and coatings

Powerful cells have fine particle sizes. Nonhomogeneous mixtures of large and small particles are often used to improve energy density. Low resistance electrodes made with low loading and fine particles reduce the chance of particle cracking. Low resistance electrodes also have reduced chance of lithium plating at beginning of life (BOL) but the solid electrolyte interphase (SEI) has been shown to grow deep into electrode pores causing a subsequent rapid increase in the rate of lithium plating approaching end of life (EOL) (X. G. Yang, 2017).

2.2.2 Current collectors and tabs

Current collectors are thin foil of copper (~10 µm thick) and aluminium (~20 µm thick) for the negative and positive electrodes, respectively. Placement of tabs can impact local current densities. Non uniform current densities may result in uneven wear or dangerous high localized current densities. At high currents, the current collectors and tabs can have significant impact on overall cell potential. Voltage drop in the tabs and collectors caused by high currents can cause a difference between the electrode potential and the overall cell potential.

Generally, for the 21-70 cell format, a spot-welded strip connects the negative tabs to the nickel coated can. The positive terminal is connected with a laser welded tab to the bottom of the positive terminal where the current interrupt device (CID) is located. The current carrying path of the positive tab can be interrupted with the CID. All the cell current must flow through the tabs and thus they must be appropriately sized such that the maximum charge current does significantly impact cell voltage. The quantity of tabs is dependant on the target design power of the cell. In general, higher power cells have more tabs (Lain M. J., 2019). Waldman recently conducted an experimental comparison of five different tab designs and demonstrated how tab design significantly impacts cell heating, cycle life, and power capabilities (Waldmann, 2023). Multiple welded tabs and tab-less designs were demonstrated to be the best performers. Figure 8 shows the different tab and tab-less designs current used.

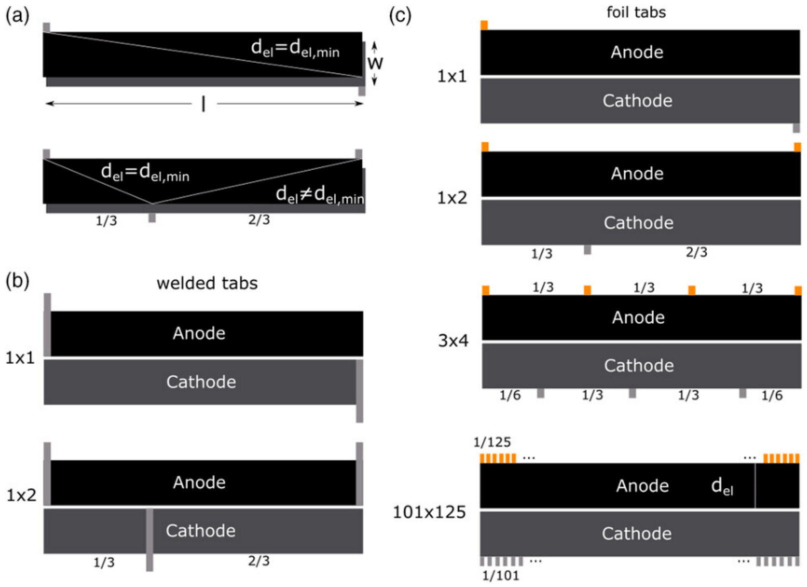

Figure 8 Tab and Tab-less designs. a) Definition of d_{el}, $d_{el,min}$, electrode width w, and electrode length *l*. b) Tab configurations for welded tabs and c) for foil tabs. The 101×125 foil tabs show the shortest distance d_{el}. Adapted without modification from (Waldmann, 2023)

Sturm modeled electrode impedance and found that during a 20 minute charge, the tab design can reduce in-plane impedance by a factor of four resulting in 23% greater capacity charged during the constant current (CC) phase. The use of tabs has also been shown to stress jelly roll and can contribute to delamination near the core (Sabri Baazouzi, 2023).

2.2.3 Electrolyte

The electrolytes used today are comprised of an organic solvent and a lithium salt. Additives may be included to improve SEI passivity, reduce flammability, reduce effects of over charging, to improve fast charging, and many other functions (Haregewoin, 2016). During cell formation, some of the electrolyte is consumed to create a passivating layer between the negative electrode and separator called the solid electrolyte interface (SEI). The SEI consists of organic compounds formed by the base organic solvent and additives. Over a cell life the SEI will grow, consuming more electrolyte solvents, salts, and lithium in the process. Unfortunately, some lithium salt can be consumed during the processes leading to loss of available lithium. SEI growth is also related to cell internal resistance growth and therefore may limit fast charge capabilities. Recent works have focused on how negative electrode expansion during charging impacts electrolyte movement. Aiken showed how at high states of charge, the material expansion of silicon containing graphite negative electrodes can push electrolyte out of the jellyroll and into the cell core (Aiken, 2023). The electrolyte movement shows a pumping effect where during discharge the electrolyte returns to the jellyroll. Although the effects shown by Aiken demonstrate how long durations at high states of charge can cause reduction of electrolyte concentration, this affect is not likely to impact cells which are allowed sufficient time to reach equilibrium. Nevertheless, analysis of electrolyte movement during fast charging is of interest especially with respect to its impact on charge rate limitation.

2.3 Rate limiting factors

Thermodynamic and electrochemical relationships limit the maximum charge rate. Fast charge rate limiting factors such as cell resistance, risk of lithium plating, and temperature limits are the most constraining. This chapter will explore charge rate limiting factors and the impact of temperature and SOC on charge rate limitations.

2.3.1 Internal resistance

Cell resistance is the greatest factor limiting charge current. Fundamentally, at a given temperature and SOC, the current that forces the cell voltage to the maximum limit is the maximum charge current. Cell resistance is dynamic and as described in chapter 2.1.1, it changes with temperature and state of charge. However, resistance can rapidly rise if electrolyte saturation/depletion occurs. When a high current is applied, the electrolyte becomes polarized resulting in electrolyte transport. Polarization causes an electrolyte concentration gradient through the thickness of the cell stack. As charge rate increases, the concentration gradient of electrolyte within the electrodes also increases. Figure 9 shows Colclasure's model of electrolyte salt concentration throughout the NCA/Graphite stack for low and high loading cells.

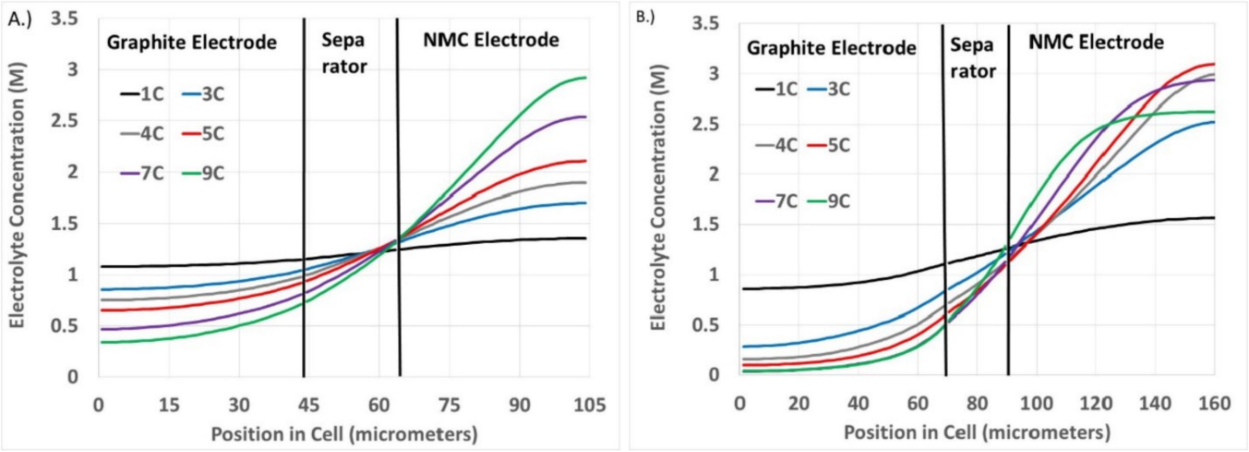

Figure 9 Model predicted electrolyte concentration profiles for (A.) Low loading and (B.) moderate loading cells at the end of CC charging to 4.1V. Adapted without modification (Colclasure, 2020).

There is a maximum current which will eventually result in zero concentration of transport salt at the back side of the electrode (current collector side). Colclasure also modeled Ionic conductivity and electrolyte diffusivity against electrolyte concentration which is shown in Figure 10.

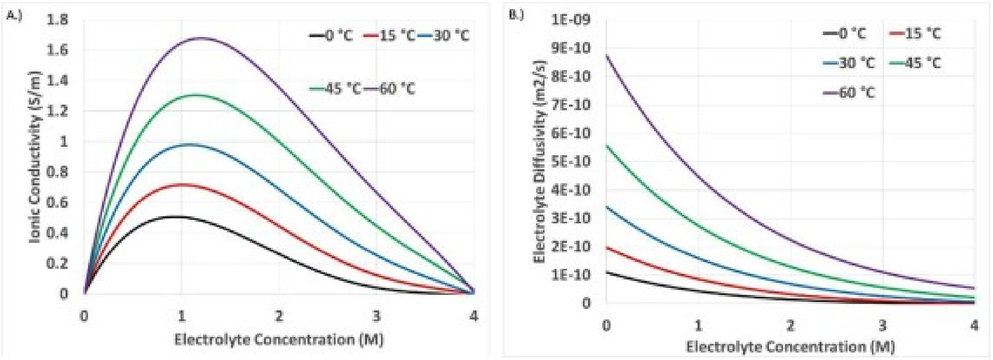

Fig. 1. Modified fits for "Gen2" (A.) ionic conductivity and (B.) diffusivity between 0 and 60 °C.

Figure 10 Figure of conductivity (A.) and diffusivity (B.) vs concentration. Adapted without modification (Colclasure, 2020).

Low local concentration of electrolyte results in low diffusion within the electrode and therefore limits ion transport and increases resistance. Conversely extremely high concentration is also limiting. The onset of salt depletion causes a rapid rise in electrode resistance and can result in accelerated lithium plating.

Electrolyte gradients and salt depletion is not an instantaneous process as rapid gradient increase can take multiple minutes to develop even at rates approaching the limit. Shah et al experimentally evaluated electrolyte/separator overpotential in symmetric lithium cells and demonstrated the relationship between time, rate, and overpotential. Figure 11 shows how overpotential can rapidly increase within a few minutes of charging above a sustainable threshold current.

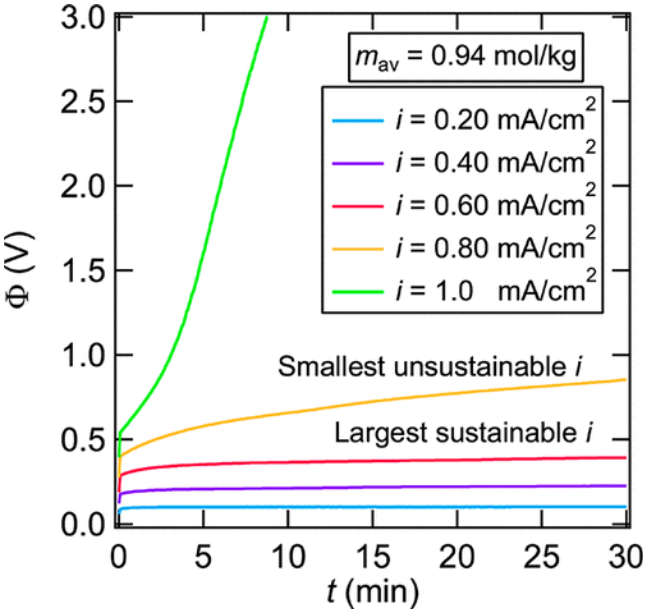

Figure 11 Time dependant potential response to applied current densities for C8-DMC/LiFSI with average salt concentration of 0.94 mol/kg. Adapted without modification from (Deep B Shah, 2019)

Measurement of diffusion can be conducted with galvanostatic intermittent titration technique (GITT) (Chien, 2023). GITT involves applying a brief pulse of current and monitoring the voltage response. Lain used a modified GITT to demonstrate the impact of electrode surface saturation on cell impedance. Figure 12 shows the electrode voltage response to a GITT pulse and illustrates the initial resistance drop followed by diffusion limitation, followed by surface saturation leading to lithium plating.

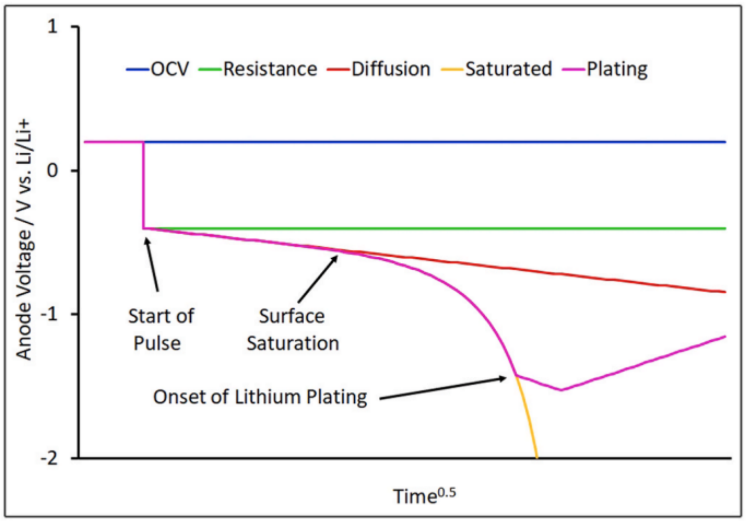

Figure 12 Rate limiting processes (Lain M. J., 2021)

Increased temperature improves electrolyte diffusion and ion conductivity. Improved electrolyte diffusion increases the maximum sustainable rate and thereby extends the time before surface saturation occurs. Further research into the effect of surface saturation within the usable cell temperature and SOC regime is needed to accurately define the maximum current due to resistance.

2.3.2 Lithium plating

Lithium plating is relevant to fast charging due its occurrence at high charge rates. Lithium plating occurs when the negative electrode resistance overcomes the electrode open circuit potential and causes the electrode to become less than 0 V vs $\mathrm{Li}/\mathrm{Li}^{+}$. Figure 13 shows the graphite electrode voltage with respect to charged capacity and the various stages of intercalation. The highest risk of plating is when the anode particles are in phases 1, 2, and 2L where the open circuit potential is the lowest.

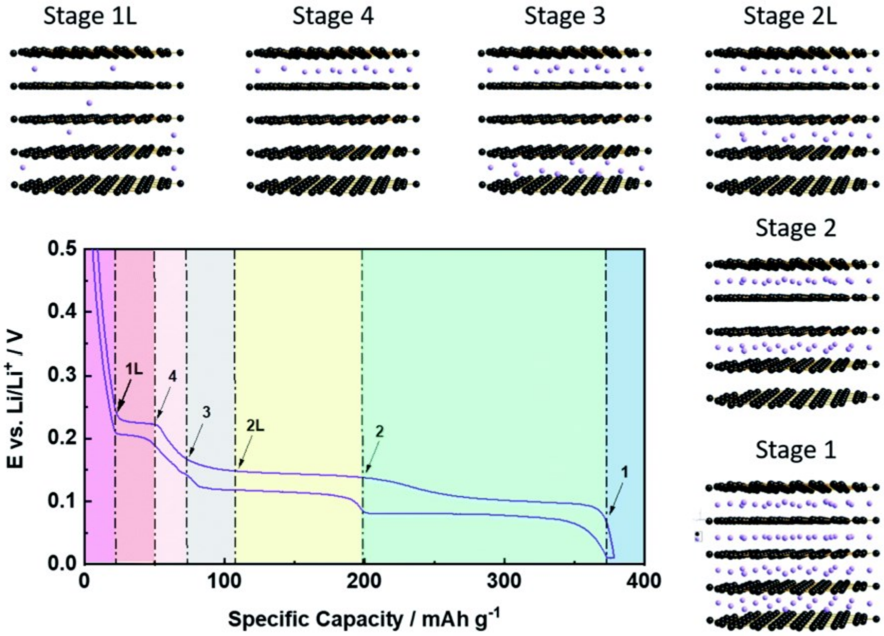

Figure 13 Staging of Li+ intercalation into graphite. Adapted without modification from (J. Asenbauer, 2020)

The risk of plating results in a need to reduce the charge current to a level which does not cause the electrode overpotential to go above the open circuit potential. High charge rates can cause lithium plating even at moderate temperatures (Teng Liu, 2021). Sieg et al used electrode material from a commercially available energy cell and a reference electrode (third electrode) to measure the real time negative electrode voltage. The maximum current required to force the negative electrode to 0 V vs. Li/Li^+ defined the maximum current as a function of SOC and temperature. Figure 14 shows the maximum current which could be applied before causing lithium to plate at different temperatures.

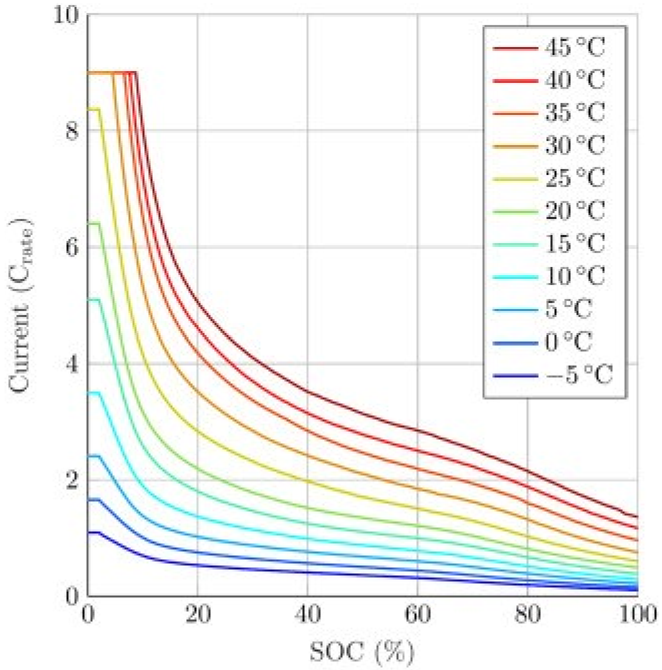

Figure 14 Maximum fast charging current over SOC at different temperatures (characteristic map) determined by fast charging 3-electrode cells with current control to 1 mV anode potential. Adapted without modification from (Sieg, 2019)

Seig et al showed that elevated temperatures are critical to reduce negative electrode resistance and thereby plating risk. The maximum initial charge rate at 45 ˚C is over 8 C whereas the limit is 1.4 C at 0 ˚C.

When lithium plates onto the surface of the negative electrode, the available lithium content is depleted. Plating can also lead to consumption of electrolyte via SEI growth over the plated lithium which further exacerbates the problem by increasing resistance. Although lithium plating can be reversible it predominantly causes severe accelerated electrode damage and can result in the growth of dangerous separator piercing dendrites. Yang et al suggests that the drop of anode porosity associated with SEI growth causes increased localized impedance and initiates the onset of lithium plating (Yang X. G., 2017).

2.3.3 Temperature

A charge session rate may become limited if a cell goes above or below critical temperature range, such as approaching the bounds of the datasheet recommended 0 - 60 ˚C. Thermal based charge rate limitations are primarily imposed due to safety and degradation concerns. The high level of energy, high heat generation, and elevated temperature causes cells to be at an increased level of risk when fast charging. At lower temperatures, where cell resistance is higher, the main concern is lithium plating.

Increased cell degradation occurs at elevated temperatures. Side reactions between electrolyte, SEI, and active materials result in loss of lithium inventory, salt depletion, and SEI growth. Degradation at high temperatures is proportional to the time spent at elevated temperatures and the magnitude of the temperature. Limiting charge current to appropriate levels such that the TMS can reduce temperature to safe levels is an effective method to reduce safety concerns and degradation at the cost of charge time.

2.4 Impact of charge profile on charge performance

There are two main interconnected systems for controlling battery state during a charge session: thermal control and electrical control. The setpoint temperature and current over time comprises the thermal and electrical charge profiles. Both profiles have significant impact on charge performance in their own ways. This chapter will introduce how the charge profile impacts charge performance.

2.4.1 Thermal profile

The thermal profile during charging is controlled by the BMS and is dependant on the TMS. A TMS consists of a heat transfer mechanism to and from the cell, a transport mechanism, and heat rejection mechanism. The sizing of the thermal system is dependant on the cell heat generation, electrical profile, and cell architecture. Characterizing cell heat generation and its dependency on rate, SOC, and state of health (SOH) is required to appropriately size cooling system components and is thus a key focus of this research.

In practice, pre-conditioning to a setpoint temperature before charging and transitioning to cooling during charging is common. Pre-conditioning is used before charging to place the battery in a temperature range with reduced resistance and risk of lithium plating. Pre-conditioning is achieved by heating or cooling the battery to a specific temperature using the onboard TMS. The ideal pre-charge setpoint temperature varies by battery, TMS, and charge profile but is often in the range of 35 to 45 ˚C. Cooling the battery at some point during the charge is required depending on charge rate, environmental conditions, and TMS configuration. Heat generated during the charge may increase battery temperature if the TMS is not powerful enough to transfer heat away and thus improper selection of pre-charge setpoint and thermal system power may result in derating due to high cell temperature.

Thermal profiles investigated in literature primarily focus on adiabatic and isothermal. Recent works by Lui et all used GT -AutoLion simulation software show the dependency of battery behavior with respect to cell temperature condition during charge (Teng Liu, 2021). The deposition potential during charging at 60 ˚C remains above the critical 0 V threshold throughout the charge. Whereas the 30 ˚C condition results in high risk of lithium plating after only 25 % of the charge was completed. Figure 15 shows battery temperature, voltage, heat dissipation, and lithium deposition potential vs time during 20 minute charging.

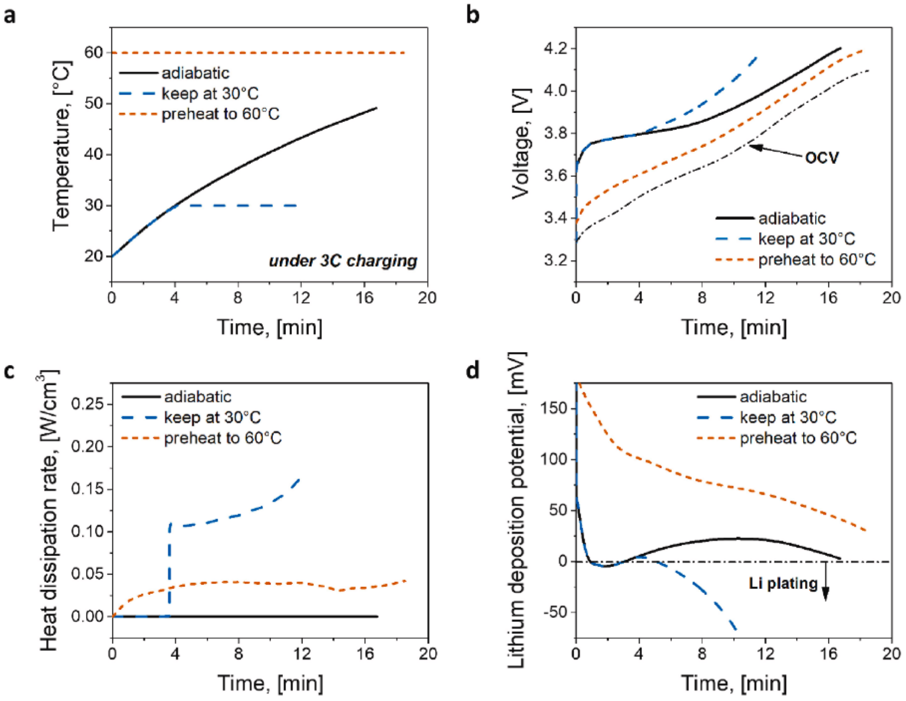

Figure 15 Battery behaviors under 3C fast charging with different thermal environments. (a) temperature profiles. (b) voltage profiles. (c) requisite volumetric heat dissipation rates. (d) evolution of lithium deposition potentials. Adapted without modification from (Teng Liu, 2021).

Figure 15 shows how maintaining a pre heated temperature of 60 ˚C maintains greater than 25 mV lithium deposition potential and that the adiabatic condition also reduces the lithium deposition potential to near 0 throughout the charge. These findings suggest that elevated temperatures are required to avoid lithium plating. In summary, optimizing the temporal profile can reduce energy spent on thermal control, increase safe charge rate, and reduce charge time.

2.4.2 Electrical profile

In literature the most common charging profile is the two-stage algorithm where the charge session consists of a CC to constant voltage (CV), or constant power (CP) to CV. During the first stage, the battery voltage gradually rises until reaching its maximum voltage where it begins the CV phase. In the final stage, the charger does not operate near its power or current limit as the current tapers off to maintain constant battery voltage.

Three alternative charge profiles include multistage constant current (MSCC), boost charging (BC), and pulse charging (PC) are shown in Figure 16.

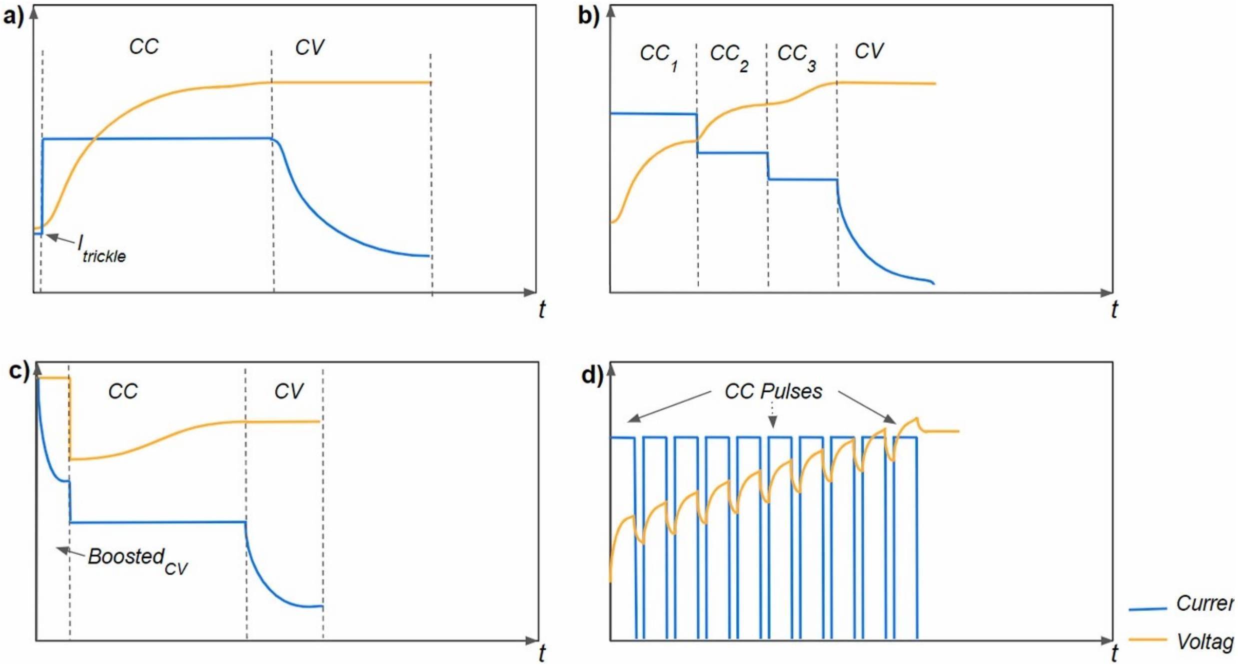

Figure 16 Electrical charge profiles. a) CC-CV, b) Multistage CC-CV, c) Boost charging, d) Pulse charging. Adapted without modification (Thusitha, 2022).

The latest charge profiles observed in commercially available electric vehicles feature an initial ramp up of power followed by a constant period of maximum power, finishing with a near linear reduction of power until reaching the target SOC. This type of charging is similar to boost charging (BC) in literature. BC takes advantage of the high negative electrode potential at low SOC by charging at a high rate at low SOC.

2.5 Key research points

The literature review above explored high power cell design, cell electrochemical relationships and their impact on cell performance, state of the art battery management system architecture, and battery management characterization techniques. In summary, safe and controlled fast charging of lithium-ion batteries requires characterizing a wide spread of battery parameters to inform advanced thermal and electrical control system operation and models. This study intends to develop and demonstrate multiple methods useful for benchmarking fast charging cell performance. The following chapters will present methods and findings in the following key research areas:

1. Cell construction and design

   Cell cycle performance data is often reported without detailed analysis of cell design and material composition. Cell electrode composition and geometry and tab design provides insight into the power capabilities and contextualizes cycle performance with respect to rate. Cell properties such as particle size and active material thickness are critical metrics for comparison.

2. Rapid cell performance mapping:

   Traditional methods of characterizing cell performance using repeated cycles at fixed charge rate and temperature conditions take substantial time and resources to produce results. Rapid cell characterization in as few as one hundred cycles using isothermal holders and an increasing charge rate approach substantially reduces cell characterization time and measures relationships between temperature, rate, and multiple key metrics such as charge time and energy efficiency.

3. Cell performance due to asymmetric temperature

   Pre-conditioning cell temperature prior to fast charging is frequent practice in electric vehicles. Many existing pack level thermal control systems do not have the ability to rapidly re-position pack temperatures and require multiple minutes to pre-condition. There is little prior art exploring what happens to cell charge performance in response to ultra fast temperature transitions during fast charging. This study will investigate cell response to rapidly altered cell temperature before start of charge, before CV phase, and during CV phase.

4. Convective AIR chamber versus isothermal cell holder:

   Characterizing fast charging cell performance in convective air chambers results in non isothermal data collection. Investigating use of isothermal cell holders' impact on charge performance is of interest. Traditional cell performance benchmarking methods often report cell performance relative to environmental chamber ambient temperature and neglect the affects of temperature gradients within the cell.

5. Cell internal temperature:

   The relationship between internal cell temperature and wall temperature, and cell charge rate is needed for identifying safe operational rates. Internal cell temperature measurement has been widely studied at low to moderate cell charge rates with small format cells (e.g. 18-65). However, further study of the internal temperature of cells designed for high power operating in ultra high charge conditions is necessary for identification of safe temperature gradient thresholds.

Chapter 3 Experimental equipment

This chapter outlines the experimental equipment used to investigate the performance of high-power cells charging at ultra high rates in isothermal and air chamber conditions.

Experimentation was conducted at the Renewable Energy Storage Laboratory located on Dalhousie University's Sexton campus in Halifax, Nova Scotia, Canada. The equipment used in this study was a Neware CT-4008 Battery Cycler, an Associated Environmental ZBHD-508 air thermal chamber, custom cylindrical 2170 cell holders, a novel Isothermal cell holder built by Litens automotive, and Omega SCPSS-020U-12 thermocouple probes. Figure 17 and Figure 18 show the air chamber and isothermal cell holders.

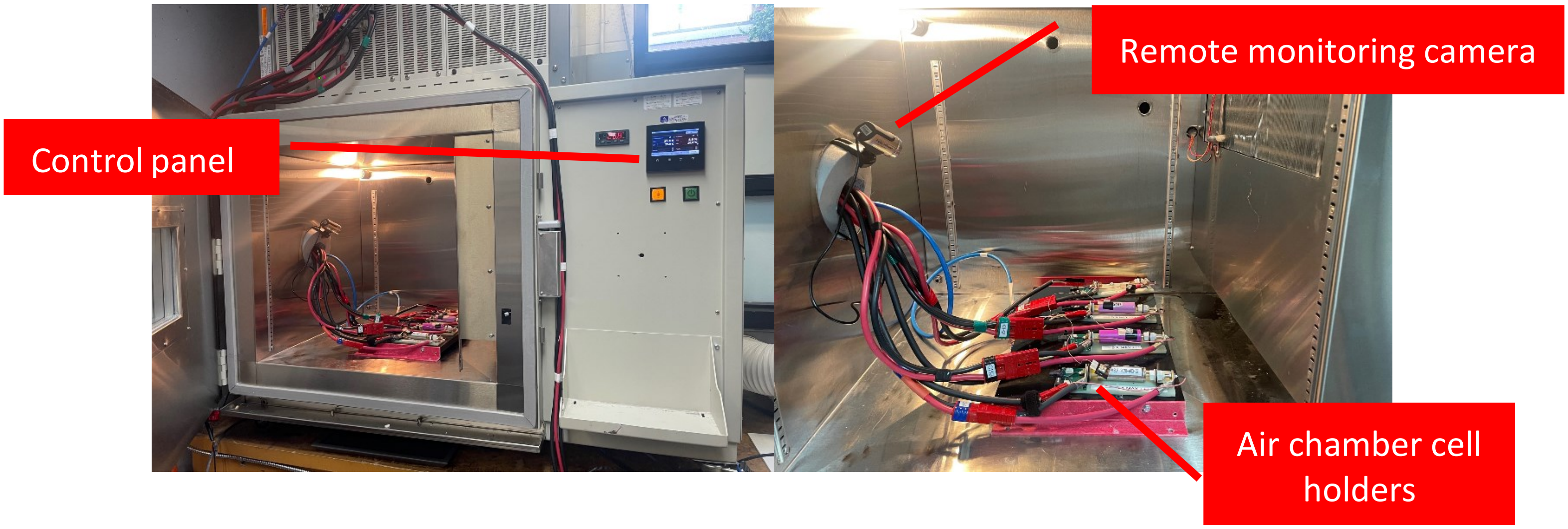

Figure 17 Air chamber with air chamber cell holders

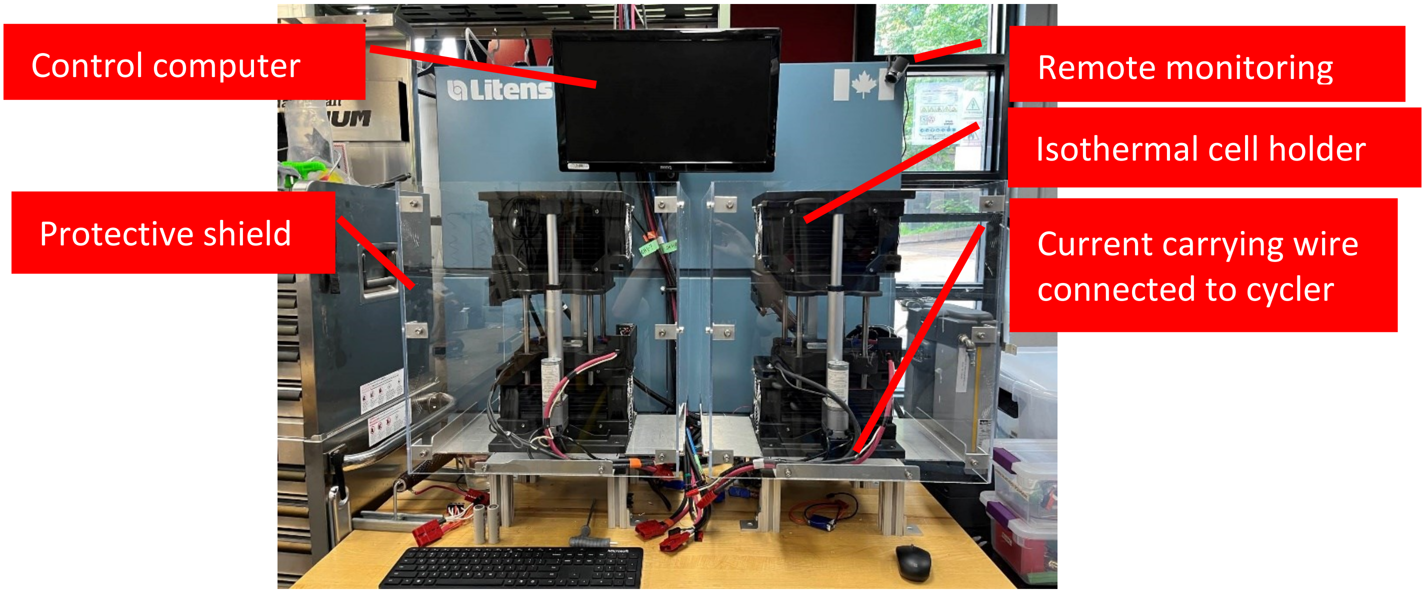

Figure 18 Isothermal cell holder apparatus

3.1 Cell information

The following cell specifications are recommended by Molicel for the P45B cell (Molicel, 2020).

Table 2 Molicel P45B datasheet parameters

Parameter	Value	Unit
Maximum voltage	4.2	V
Minimum voltage	2.5	V
Capacity	4.5	Ah
Energy	16.2	Wh
Impedance (AC)	7	mΩ
Resistance (DC)	15	mΩ
Maximum charging current	13.5	A
Nominal charging current	4.5	A
Maximum discharge current	45	A
Maximum temperature	60	˚C
Minimum temperature	-20	˚C
Minimum charge temperature	0	˚C

3.1.1 Cell Conditioning

Since new commercially available cells used in this study may not have a fully formed SEI, conditioning cycling prior to performance measurement was necessary. To confirm performance stability, twenty cycles of 1 h discharge and 1 h charge were completed. Throughout the twenty cycles the internal resistance is expected to decrease. Evidence of DC internal resistance decrease is inferred by an observed increase and plateau of energy efficiency and maximum cell temperature was measured to drop from 31.5 to 30 ˚C from the first to last cycle. Figure 19 shows the energy efficiency and cell temperature plateau during conditioning cycling.

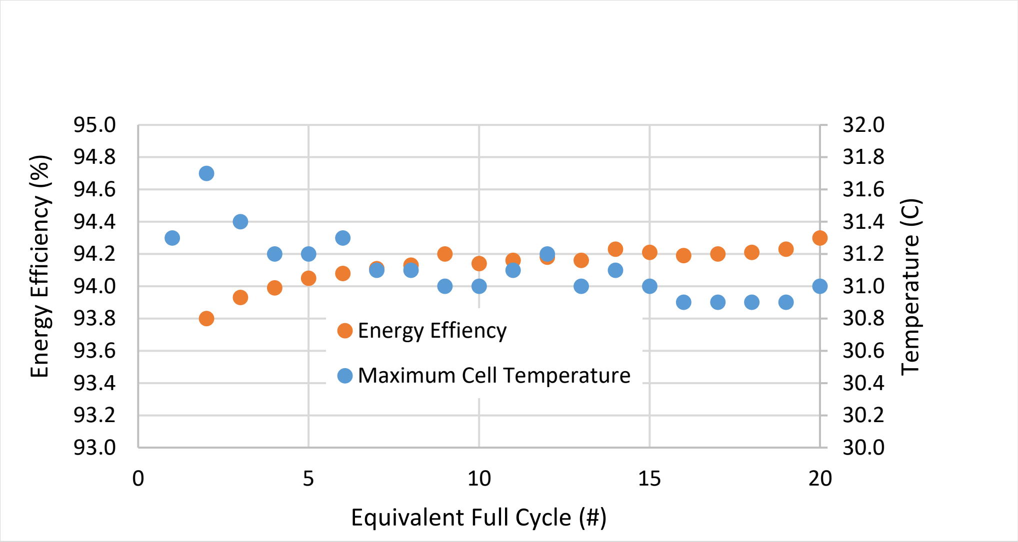

Figure 19 Energy efficiency and maximum cell temperature during twenty conditioning cycles.

3.2 Cycling equipment

3.2.1 Battery test cycler

The eight channel Neware CT-4008-5V50A Battery Testing System with 5 V 50 A rating was used in this study and is pictured in Figure 20. The unit was calibrated and verified prior to cell testing. Additional cycler specifications including measurement uncertainties can be found in Appendix B.

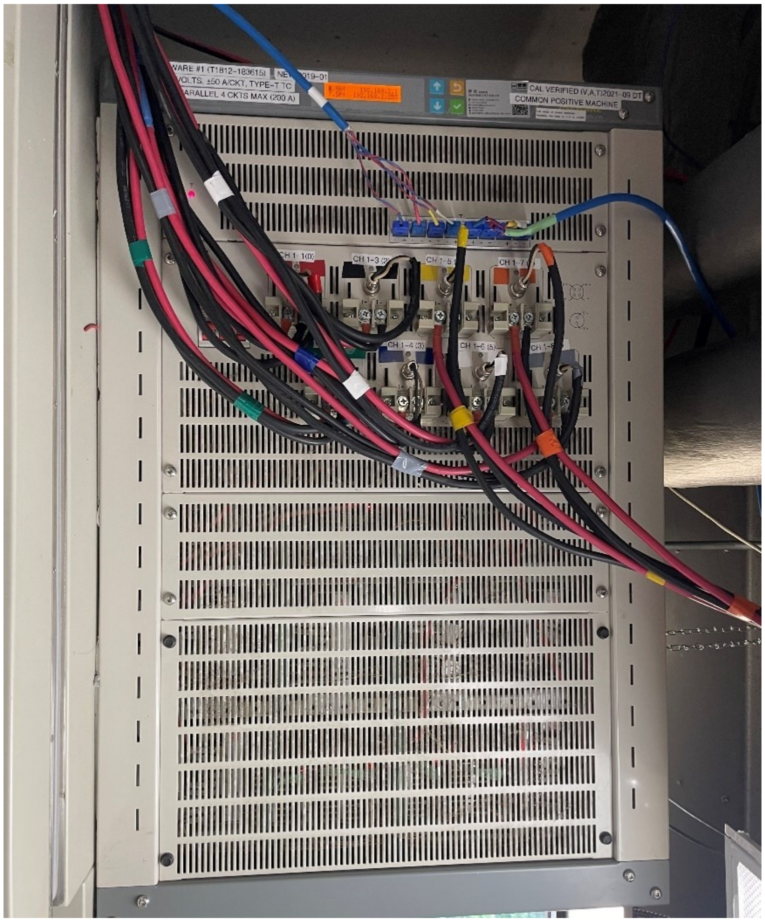

Figure 20 Neware Battery Testing System 8 Channel 5 V 50 A

3.2.2 Cell holders

This study cycled cells using four different cell holder apparatus. At high rates, cell temperature is sensitive to the current carrying method due to slight variability in contact and conductor resistance. Generic cell holders were modified for high current use in convection condition cycling whereas custom high current contacts were used in isothermal condition cycling. Instrumentation of cells using the negative cell end does not permit easy access to that surface for current carrying and voltage measurement. Thus, spot-welded nickel strips were used to carry current and measure voltage. Description of customized generic cell holders, high current probes used in isothermal testing, and spot-welded tabs follows.

3.2.2.1 Customized generic cell holders used for conditioning and convection condition cycling

For air chamber cycling custom cylindrical cell holders were used. This design features a large (10 mm diameter) current carrying contact, and a much smaller (3 mm diameter) probe located concentrically inside the larger probe for voltage measurement. Initially, 20 awg wire was used to carry current and voltage measurement to a proprietary circuit board. Due to the high rate of charge used in this study existing wire ring terminal crimps were replaced with cable lugs and 4 awg wires were terminated with Anderson connectors. A 50 A rated Anderson SB50 connector was used for current and a 15 A rated Anderson PP15 was used for voltage measurement. Figure 9 illustrates the custom cell holders used for convection condition cycling.

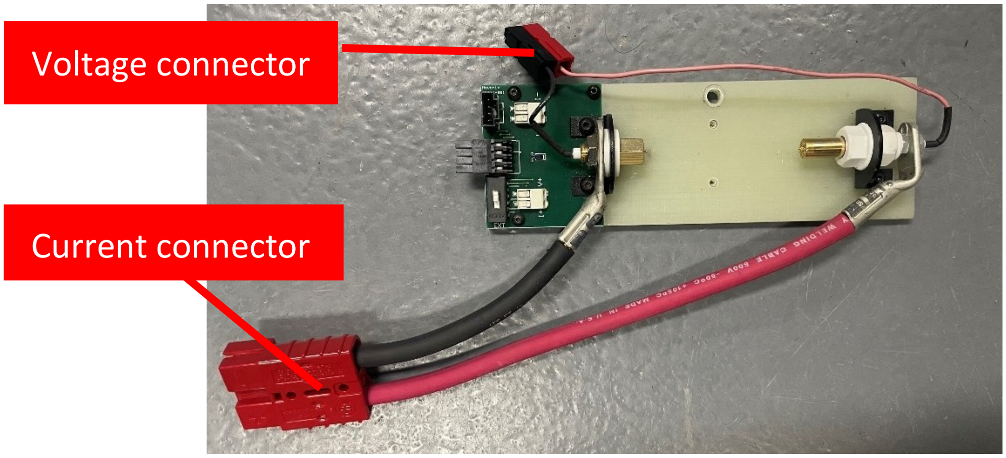

Figure 21 Customized cell holders with four wire connection

3.2.2.2 High current contacts used for isothermal condition cycling

Spring loaded high current contacts were used in the isothermal condition case. Once again Anderson SB50 and PP15 connectors were used for power and voltage wires which in this case were set screw terminated with ferrules in copper probes. The positive copper probe was spring loaded and the negative remained fixed as shown in Figure 22.

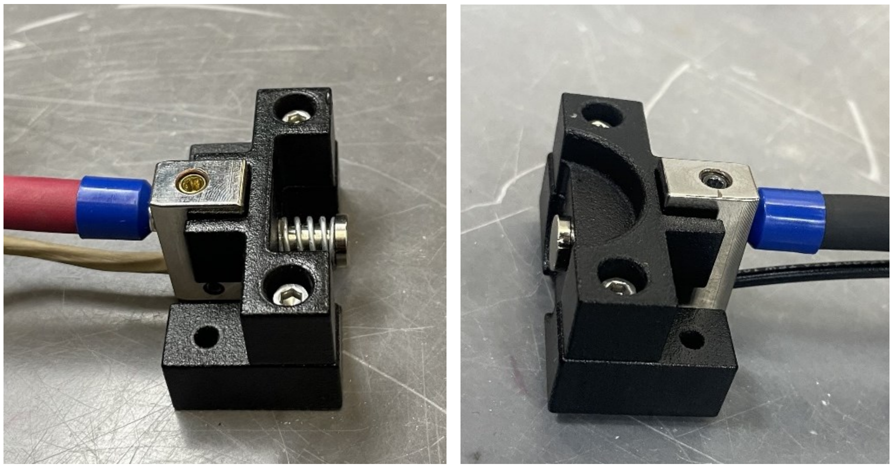

Figure 22 Cell contacts used in isothermal condition

3.2.2.3 Spot welded high current nickel strips

A spot-welded nickel strip was used during internal temperature measurement tests because the sensor location impeded the use of a traditional positive probe contact. This type of strip was spot welded to the outer rim of the cell cap. The 0.25 mm thick nickel strips were made as wide as possible (25 mm at widest) to allow for low conductor resistance and were insulated with Kapton and 3M super 88 tape.

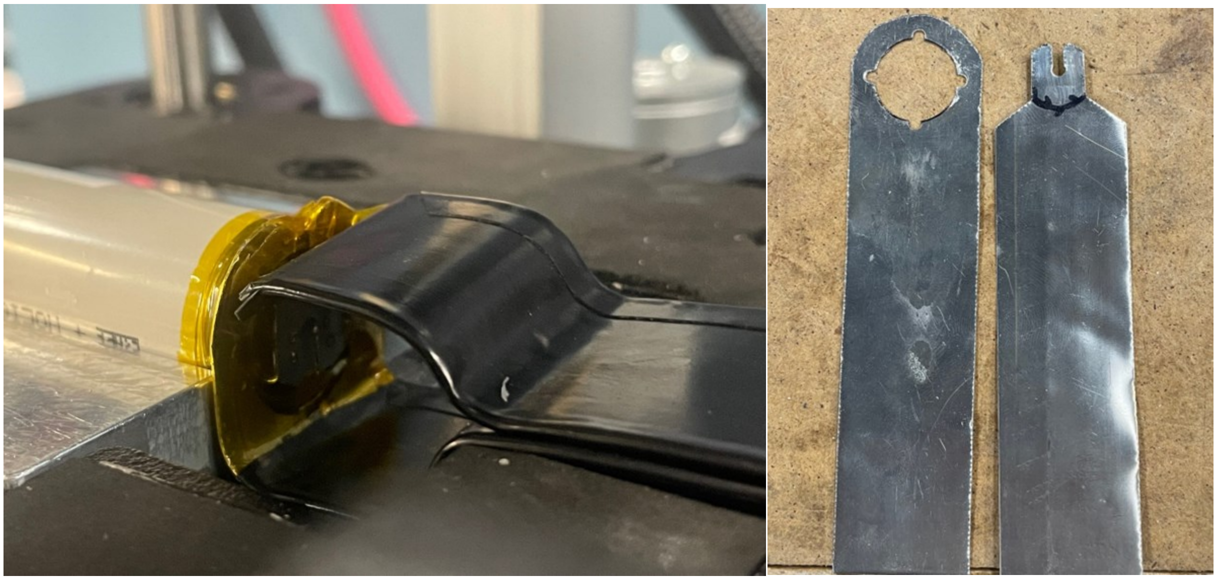

Figure 23 Spot welded strips

3.2.3 Air chamber

An Associated Environmental Systems BHD-508 Air chamber was used with air temperature control over the range of -20 to 60 ˚C. The chamber used was shown previously in Figure 17.

3.2.4 Isothermal rig

A novel isothermal cell holder was supplied by Litens Automotive Group of Ontario. This system can control cell wall temperature to within 1 ˚C throughout high current charges. The cell holder consists of two mirrored assemblies which enclose the cell. Each assembly has a cell holder comprised of a billet aluminium machined block, a Peltier heating and cooling element, a heat sink, cell temperature sensor, and heat flux sensor. The blocks are machined for a tight tolerance fit (0.125 mm radial clearance) between the cell (with jacket) and block wall. Each block temperature is independently controlled with a proportional integral differential (PID) controller. A software package enabled setpoint and timeseries temperature control. The software also recorded isothermal rig operational parameters such as cell temperature, Peltier electrical properties, and heat flux using National Instruments CompactDAQ data acquisition logger. Figure 15 shows the isothermal rig and components in more detail.

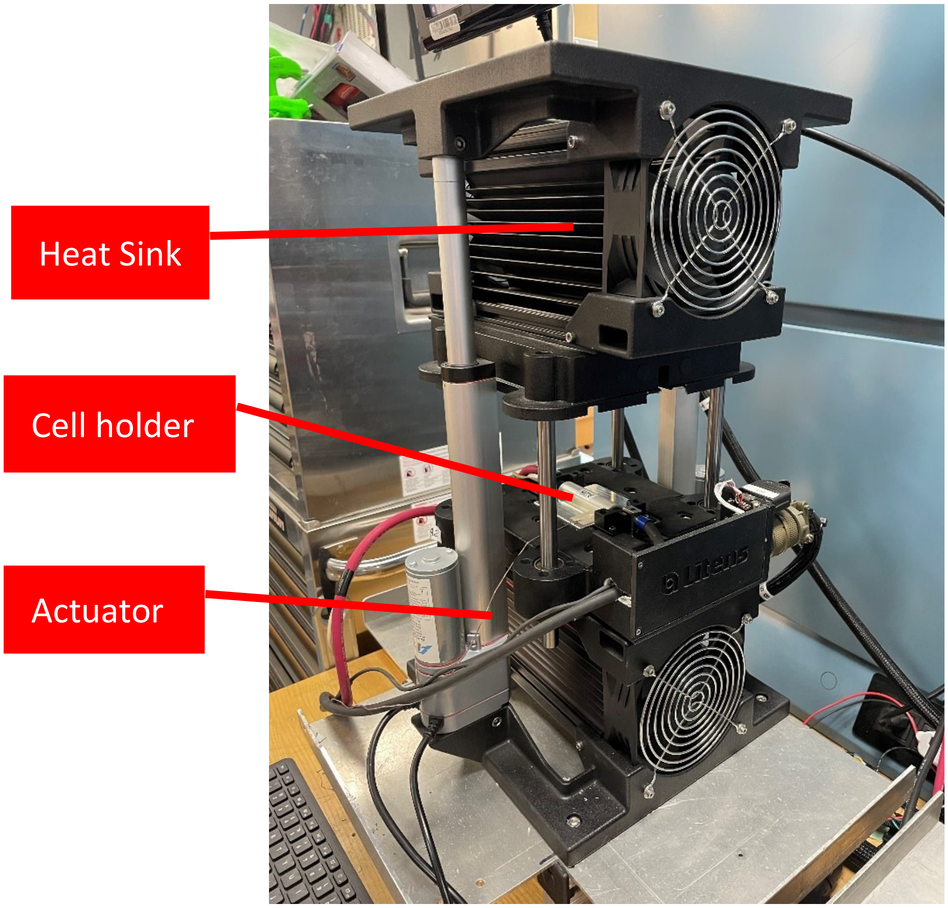

Figure 24 Isothermal rig

Chapter 4 Cell physical, chemical, and electrochemical properties

Cell current collector geometry and active material chemistry dictates current, energy delivered, and thermal response during charging. To quantify the physical and chemical properties of the cells used in this study cell dissection, inspection of surface morphology using SEM, chemical analysis with ICP, and CT scanning were used.

4.1 Dissection and inspection

Prior to dissection, cells are first discharged to reduce the stored energy and then shorted to reduce the risk of a spark igniting electrolyte. The dissection process started with a 4.5A CC-CV discharge ending in a CV hold at 1 V with 0.1 A cutoff. The cells were held at 1 V for an additional 12 h to remove as much lithium from the negative electrode as possible. The cells were then connected in parallel with a 5-ohm 50 W resistor until terminal voltage was <0.1 V. The cell cannister was then cut with fine-tooth saws until jellyroll, cap, and tabs were removable. Precision cuts are made at locations to reduce the chance of damaging electrode or shorting the cell.

The following cuts were made to dissect the cell:

1. A fine bladed coping saw is used for the first two cuts which were around the cell and are located at either end of the jellyroll where a plastic separator was.
    - The first cut wraps around the positive end of the cell just below the crimp.
    - The first cut enables removal of the positive terminal and safety devices. After the first cut the positive tabs are visible and undamaged as shown in Figure 25.
2. The second cut was made around the negative end of the cell just below the jelly roll.
3. An oscillating tool with fine blade is used to cut down the length of the cell. Care is taken to only cut the steel can and not cut into the jellyroll.
4. Once the three cuts were made, the central can section is removed, and the tabs cut.

Figure 25 shows the cutting tools used for cell dissection.

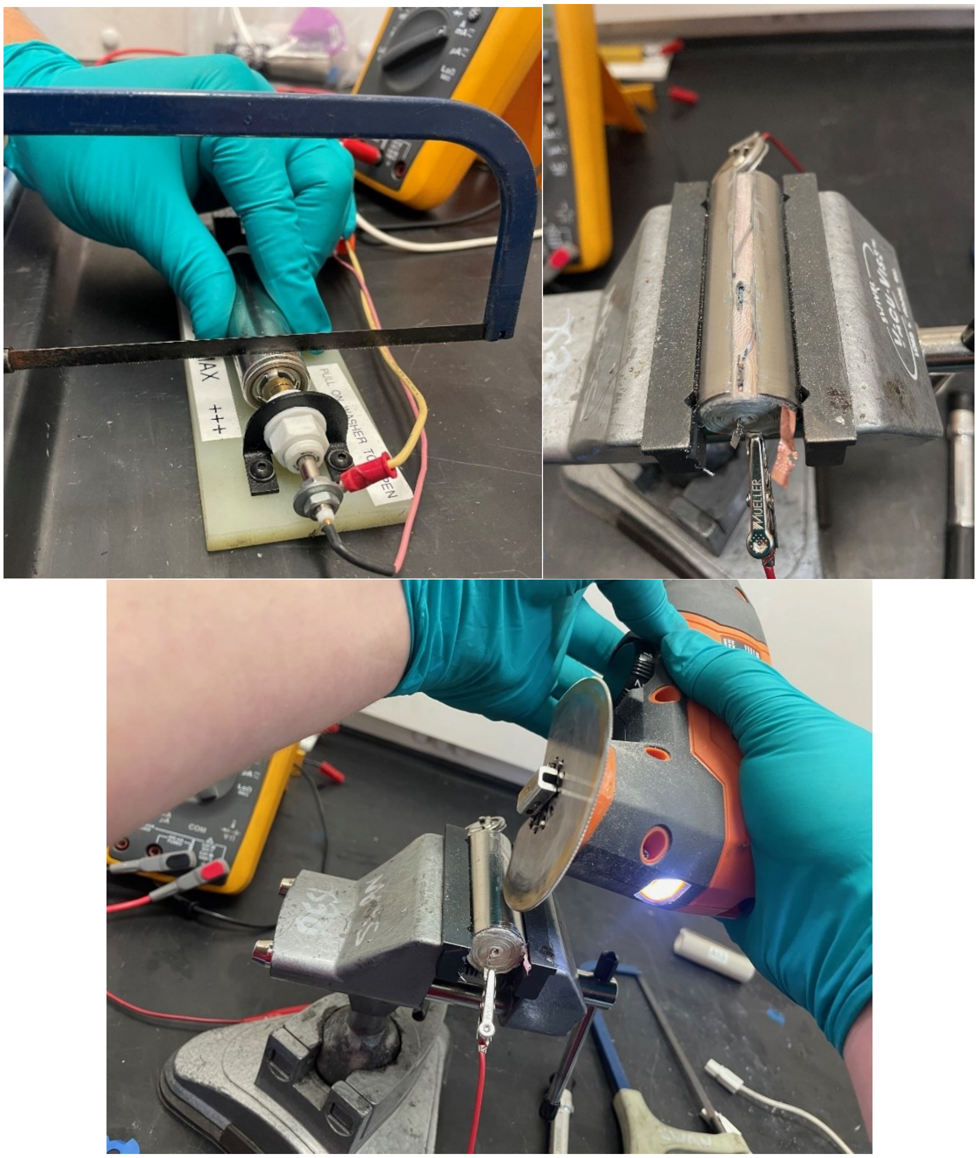

Figure 25 Cutting of 21-70 cell can

Jellyroll, anode, cathode, tab, thicknesses, and lengths are reported in Table 3, and photos of surfaces were taken. 1 cm by 1 cm samples of both electrodes were cut for SEM analysis. Approximately 5 g of active material was scraped from both electrodes for ICP analysis.

Figure 26 shows the location of tabs when the jellyroll was fully rolled out. During jellyroll inspection the thin active material on the negative electrode flaked off from the current collectors.

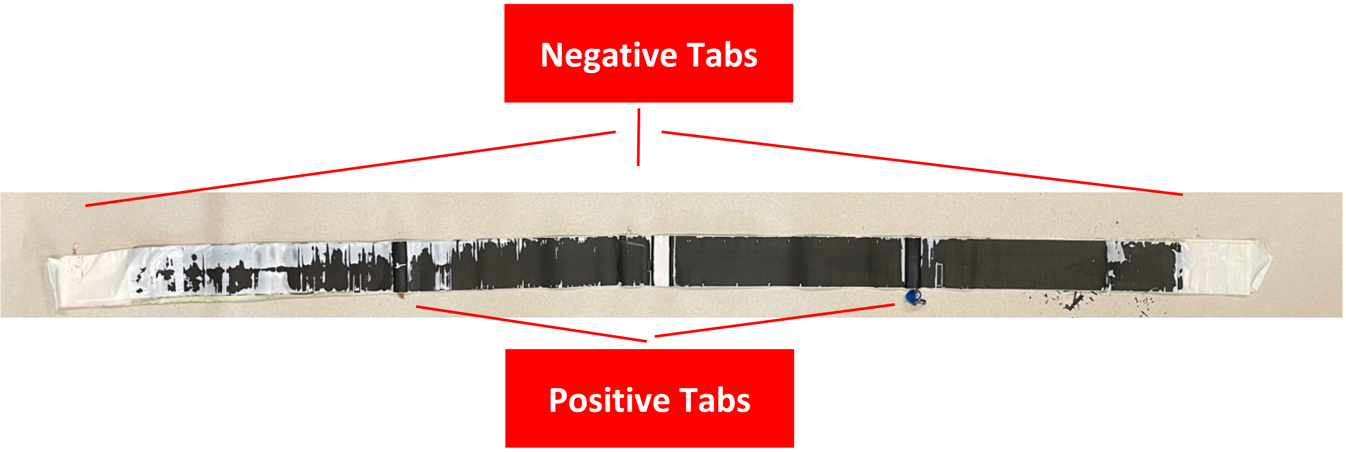

Figure 26 Figure of tab locations on jellyroll

The electrode thickness measurements found the negative electrode active material to be 51 µm and the positive active material to be 39.5 µm thick. These values show they are thin active material coatings, which is representative for high power cells. The negative active material is significantly thicker than the positive which suggests a high N/P ratio.

Table 3 P45B Jellyroll properties

Property	Value (mm)
Length	1440
Width	65
Negative tab thickness (short type)	0.098
Negative tab thickness (long type)	0.303
Negative tab width	4
Negative active material thickness (single sided)	0.051
Positive tab thickness	0.117
Positive tab width	6
Positive active material thickness (single sided)	0.039

Figure 27 shows the negative (a) and positive (b) tab arrangement of the Molicell P45B cell:

Figure 27 Figure of negative (a) and positive (b) tab geometry

Three tabs located at the center, middle, and outer jellyroll is not often used in 21-70 due to the added cost and illustrates how this cell is made for power. All three tabs are spotwelded at the center of the cell. The negative tabs are made of copper and are nickel coated. The negative tabs are 4 mm wide and the positive tabs were 6 mm wide.

The cell has two positive tabs located at the ¼ and ¾ positions along the jellyroll. The more central tab (¾ position) was directly laser welded to the positive terminal whereas the outermost tab was spot welded to the innermost tab before the tab reaches the cap.

4.2 Electrode surface morphology

A Hitachi S-4700 SEM was used in this study at the Dalhousie Engineering Scanning Electron Microscopy – Focused Ion Beam (SEM-FIB) Facility. The SEM is a device which uses an electron beam to image a material sample at extremely high magnification. This technique was used to image active material to identify particle size and surface morphology. The microscope was set to 5 kV accelerating voltage and at magnifications between 1000 to 10,000 times. 1 cm by 1 cm samples of electrode material were removed from dissected cell and transported in air to the SEM facility.

Figure 28 shows surface morphology of the positive active material (a) and negative active material (b) respectively. The PAM is comprised of two sizes of particles where the diameter of the larger particles was approximately 10 µm and the smaller are 2 µm. The negative active material appears to be flaky and of homogenous particle size. Most particles are approximately 10 µm in diameter. The appearance of flat surfaces of nearly all flakes suggests significant calendaring of the negative electrode.

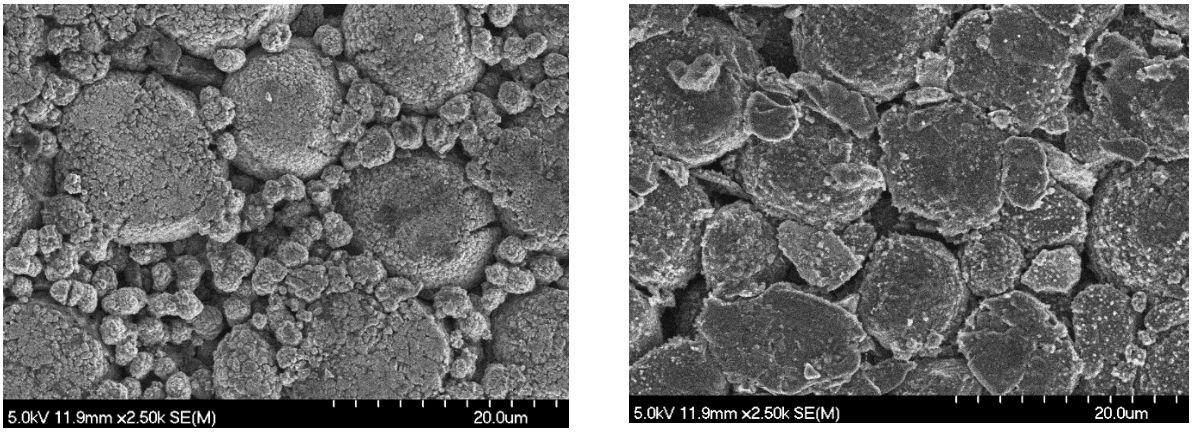

(a) positive electrode

(b) negative electrode

Figure 28 SEM imaging of active materials (a) SEM image of Molicell P45B positive electrode surface (b) SEM image of P45B negative electrode surface

4.3 Electrode material composition

The chemical composition of active material powder was analysed using Inductive Coupled Plasma - Optical Emission Spectroscopy (ICP-OES) at the Dalhousie Minerals Engineering Laboratory. The machine used was a Thermo iCap7400. The ICP-OES functions by exciting atoms in a sample using an argon plasma, measuring the intensity of the light emitted when the electrons in the atoms return to the ground or lower state, and uses a calibration graph to calculate the concentration of elements in the sample. This technique is especially useful for identifying elements that make up the positive active material (PAM) and negative active material (NAM). This technique analyses the bulk material making up the electrode. The PAM sample was processed prior to measurement with a near total acid digestion. The negative active material sample was ashed at 950 ˚C, fused with Li-borate then analysed with ICP-OES.

4.3.1 Electrode material composition results

The following tables describe the electrode material composition as measured by ICP. Table 4 presents all samples within the positive active material and Table 5 shows a comparison of only the nickel, cobalt, and aluminium.

Table 4 Positive Active Material Composition

Element	Percentage of sample by mass (%)
Ni	47.9
Co	5.08
Li	6.21
W	0.548
Al	0.392
P	0.250
Zr	0.237
Other	39.38

The other materials accounting for 39.38 % of the positive active material can be attributed to oxygen which is not detectible using this technique.

Table 5 Mixed Metal Oxide Ratio Analysis

Element	Atomic mass M (g/mol)	Sample (mg/kg)	Relative % Mass of Total	% Mol
Ni	58.693	479745	89.75	89.022
Co	58.993	50878	9.52	9.393
Al	26.982	3926	0.73	1.585
Total		534549		

The results confirm that the positive electrode chemistry is a high nickel content NCA. The results differ from the standard NCA chemistry breakdown of 85 % Nickel, 10 % Cobalt, and 5 % Aluminium. Although the aluminium is less than tradition specifications, the results are similar to other published findings which found aluminium content around 1.4 % by mass (Ohneseit, 2023). The graphite based negative active material was found to contain 3.15 % silicon using the ICP-OES process.

4.4 Computed tomography

CT imaging illustrated the impact that drilling has on the tabs, it verified thermocouple location, and it identified jellyroll irregularities in a fresh cell.

Computed tomography (CT) uses a beam of X-rays and digital detector to capture sectional images of the cell. Post processing of images results in a 3-dimensional re-construction of the cell. A Bruker Skyscan 1272 was used to image internal features before and after probing the cell with a temperature sensor. Knowledge of cell internal negative terminal tab locations is helpful for avoiding them when drilling for thermocouple probe insertion. The Bruker Skyscan 1272 used is shown in Figure 29.

Figure 29 Bruker Skyscan 1272

4.4.1 Jellyroll irregularities

In cylindrical cells, maintaining the cell core is especially important to ensuring long cycle life and safety. The cell core can collapse resulting in separation of active materials from current collectors, increased SEI growth, and poor cell performance.

Figure 30 shows a disrupted jellyroll in the area surrounding the central negative tab of a new cell. The disrupted jellyroll may be indicative of a future a core collapse caused by physical degradation of electrode and SEI growth. Cyclical thermal expansion of the electrode could cause shifts in the jellyroll which pose a short circuit risk due to the presence of folds. Further, jellyroll disruptions are present near all other tabs. Although larger gaps between electrodes are observed in affected areas, their impact on cell capacity is not known. These gaps may be artifacts of this cell design and may be present in all cells manufactured in this way. However, these gaps are known to affect performance through increased SEI growth.

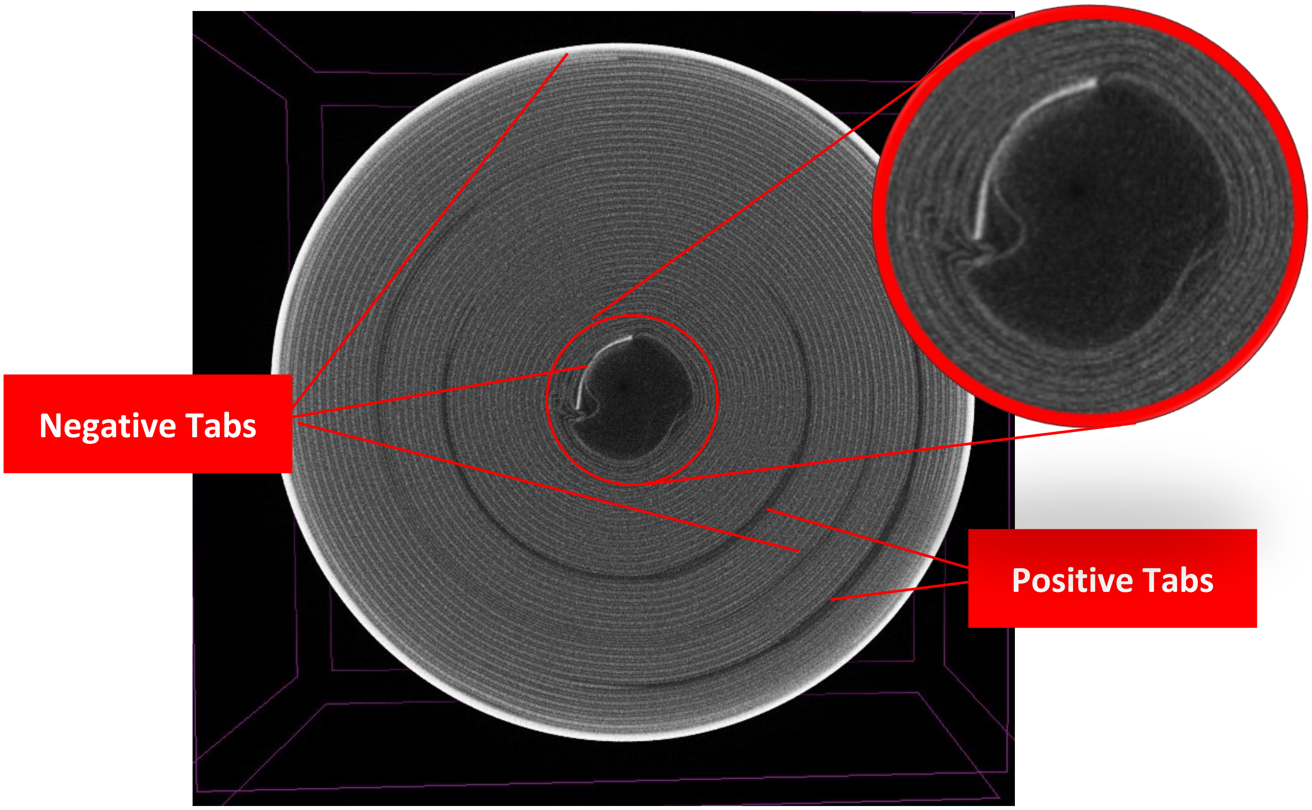

Figure 30 CT scan of Moli P45B cell

This CT imaging method will later be used to locate the internal temperature sensor following sensor insertion.

Chapter 5 Performance mapping in isothermal conditions

Battery performance during charging is highly dependent on current and temperature conditions. Mapping battery performance against charge condition provides battery system designers with valuable understanding of how cell performance metrics respond to independently changing conditions. With respect to fast charging, the most important performance surfaces include those with charge time, capacity, and energy efficiency on the third axis. Comparing the charge time or capacity during the CC and CV phases provides significant insight into how temperature impacts a cells ability to accept current throughout its usable capacity range.

This chapter outlines a test protocol for mapping performance over a range of charge rates and temperatures, and then it analyses the dependency of key metrics on charge rate and temperature. First, data from full 0 to 100 % SOC charges under different rate and temperature conditions is analysed identifying how charge condition impacts total charge time. Second, CC and CV stage contributions dependency on charge condition is presented. Opportunities for optimizing CC and CV charge stage performances are discussed including the quantification of performance trade-off with cell temperature. Recommended charge conditions are identified and discussed for both CC and CV stages. Finally, the impact that state of charge limitations has on charge time and capacity discussed with the trade-off identified. The trade-off between charge condition, termination SOC and charge time is contextualized with practical charge session constraints. This dataset is intended to be used to compare different cell charge performances, identify optimal temperature and charge rate regions, and inform charge profile parameter selection.

5.1 Performance mapping protocol

One of the most important relationships investigated in this study is the cell charge performance as a function of charge rate and temperature. This study develops a rapid testing procedure which creates a multidimensional performance surface that can be used to track cell performance across a range of rates, temperatures, and states of heath. To generate data defining relationships between cell capacity, energy, efficiency, and other parameters with respect to charge rate and temperature, isothermal cycling was conducted with a defined test protocol. The technique used a single discharge rate of 4.5 A to 2.5 V which achieves a consistent fully discharged state before starting each charge. Then, repeated charges at 25 different charge conditions were performed. Temperatures 25, 35, 45, 55, 65 ˚C and CC- CV charge rates 4.5, 13.5, 17, 23, 27 A were used as conditions. The technique created a 5 x 5 matrix of datapoints which can be used to plot 3-Dimensional surfaces with key metrics on the third axis.

The cells that were used for this performance map were first conditioned with twenty 1-hour rate cycles, they were then run through a series of increasing charge rate cycles at each set point temperature. Before each temperature, three cycle reference performance test (RPT) was conducted at the 1 h CC rate at isothermal 25 ˚C to establish a trackable SOH. This cycle determined the capacity degradation throughout the test series. Following the RPT, three cycles at each charge rate were completed. Then, the temperature would be increased to the next setpoint, and the process would repeat again. Table 67 and 8 shows the test ID (TXX) and test conditions used to map performance.

Table 6 Performance mapping test procedure

Test ID	Type	Temperature (°C)	Charge Rate (A)	Description
T01	Conditioning	25	4.5	20 cycles of 1:1 h CC:CC-CV
T02	Fast Charge	25	4.5	3 cycles of 1:1 h CC:CC-CV
T03	Fast Charge	25	13.5	3 cycles of 1:X h CC:CC-CV
T04	Fast Charge	25	17.0	3 cycles of 1:X h CC:CC-CV
T05	Fast Charge	25	23.0	3 cycles of 1:X h CC:CC-CV
T06	RPT	25	4.5	3 cycles of 1:1 h CC:CC-CV
T07	Fast Charge	35	4.5	3 cycles of 1:X h CC:CC-CV
T08	Fast Charge	35	13.5	3 cycles of 1:X h CC:CC-CV
T09	Fast Charge	35	17.0	3 cycles of 1:X h CC:CC-CV
T10	Fast Charge	35	23.0	3 cycles of 1:X h CC:CC-CV
T11	RPT	25	4.5	3 cycles of 1:1 h CC:CC-CV
T12	Fast Charge	45	4.5	3 cycles of 1:X h CC:CC-CV
T13	Fast Charge	45	13.5	3 cycles of 1:X h CC:CC-CV
T14	Fast Charge	45	17.0	3 cycles of 1:X h CC:CC-CV
T15	Fast Charge	45	23.0	3 cycles of 1:X h CC:CC-CV
T16	RPT	25	4.5	3 cycles of 1:1 h CC:CC-CV
T17	Fast Charge	55	4.5	3 cycles of 1:X h CC:CC-CV
T18	Fast Charge	55	13.5	3 cycles of 1:X h CC:CC-CV
T19	Fast Charge	55	17.0	3 cycles of 1:X h CC:CC-CV
T20	Fast Charge	55	23.0	3 cycles of 1:X h CC:CC-CV
T21	RPT	25	4.5	3 cycles of 1:1 h CC:CC-CV
T22	Fast Charge	65	4.5	3 cycles of 1:X h CC:CC-CV
T23	Fast Charge	65	13.5	3 cycles of 1:X h CC:CC-CV
T24	Fast Charge	65	17.0	3 cycles of 1:X h CC:CC-CV
T25	Fast Charge	65	23.0	3 cycles of 1:X h CC:CC-CV
T26	RPT	25	4.5	3 cycles of 1:1 h CC:CC-CV

Table 7 Performance mapping test procedure

Test Completed		**Temperature (°C)**				
		25	35	45	55	65
Rate (A)	4.5	T02,T06,T11, T16, T21,T26	T07	T12	T17	T22
	13.5	T03	T08	T13	T18	T23
	17	T04	T09	T14	T19	T24
	23	T05	T10	T15	T20	T25

5.2 Performance metrics

Table 8 summarizes key metrics, their units, and a brief description.

Table 8 Key charge metrics

Key Metric	Units	Description
CC Charge time	s	Time to complete constant current phase of charge
CV Charge time	s	Time to complete constant voltage phase of charge
Charge time	s	Total time to charge cell
Charge Capacity Ratio	(-)	Ratio of time spent in the CC stage compared to the total charge time and represents the SOC when the charge reaches the CV stage
Charge Time Ratio	(-)	Ratio of time spent in the CC stage compared to the total charge time
% Capacity / Minute	(%)	Ah delivered / Nominal capacity x 100 per minute of time.

The ratio of capacity charged, or time spent in the CC phase divided by total charged capacity (including CV phase) provides insight into the cell resistance as it approaches high SOC. Figure 31 shows the voltage and charged capacity during a 13.5 A CC charge to 4.2 V. The charge results in an 834 second CC phase which delivers 3.12 Ah and a total charge time of 3000 seconds with 4.35 Ah charged capacity. The following calculations show the CC-CV charge capacity and time ratios.

$$Charge\ Capacity\ Ratio = \frac{CC\ Stage\ Charged\ Capacity}{Total\ Charged\ Capacity} = \frac{3.12}{4.3} = 0.72 \qquad (4)$$

$$Charge\ Time\ Ratio = \frac{CC\ Stage\ Charge\ Time}{Total\ Charge\ Time} = \frac{834}{3000} = 0.29 \qquad (5)$$

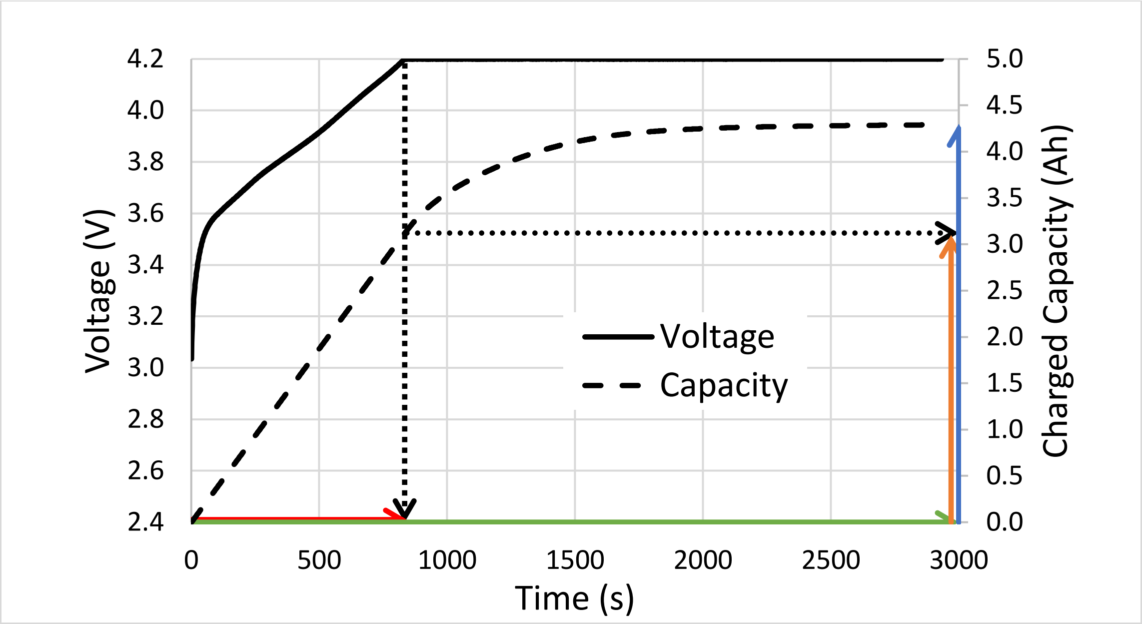

Figure 31 Voltage and Charged Capacity Vs Time During 13.5 A 4.2 V CC-CV Charge at 25 ˚C

5.3 Impact of charge conditions on charge performance

This chapter section will first present the total 0 – 100 % SOC charge time versus current and temperature surface then it will distinguish how the CC and CV charge stage contributions impact the total charge time. In summary of the performance map, Figure 32 gives the total charge time when charging from 0 to 100 % SOC at different charge current and temperature conditions. Excel was used to fit power trendlines for each temperature.

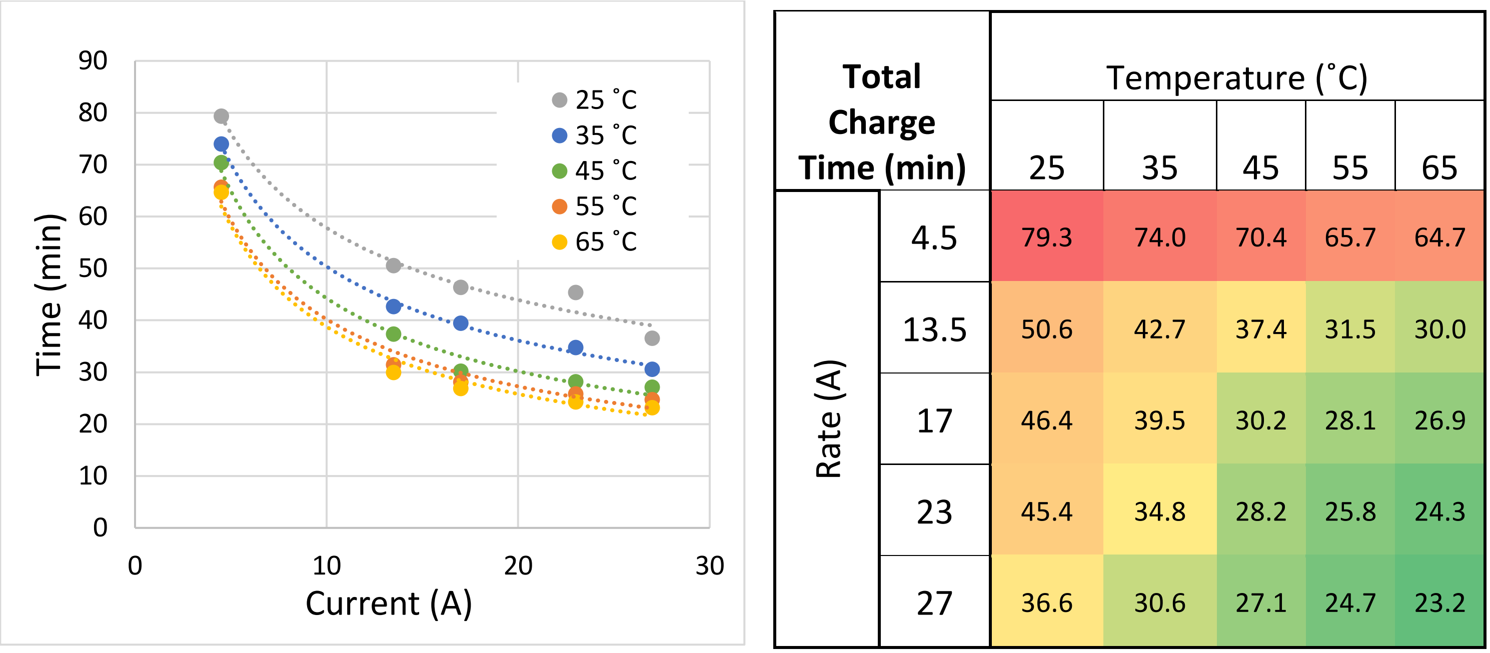

Total Charge Time (min)		Temperature (˚C)				
		25	35	45	55	65
Rate (A)	4.5	79.3	74.0	70.4	65.7	64.7
	13.5	50.6	42.7	37.4	31.5	30.0
	17	46.4	39.5	30.2	28.1	26.9
	23	45.4	34.8	28.2	25.8	24.3
	27	36.6	30.6	27.1	24.7	23.2

Figure 32 Total charge time for different CC charge rates and temperatures

From Figure 32 it can be determined that:

- At all rates, increasing temperature reduces charge time.
- At all temperatures, increasing rate reduces charge time
- Both temperature and rate relationship to charge time is nonlinear, and each have diminishing return with further increase.
- The fastest charge time of 23.2 min was measured at the 27 A, 65 ˚C condition.
- At 13.5 A, increasing temperature from 25 ˚C to 65 ˚C reduces charge time from 50 minutes to 30 minutes.

- Charging at 13.5 A and 45 ˚C results in the same charge time as charging at 27 A and 25 ˚C.

While Figure 32 gives the total charge time, analysing how the components of time spent in CC and CV stages provide additional context to how charge time changes with charge condition. Figure 33 distinguishes the individual contributions of the CC and CV phases have on the total charge time and quantifies their relationship with charge rate and time.

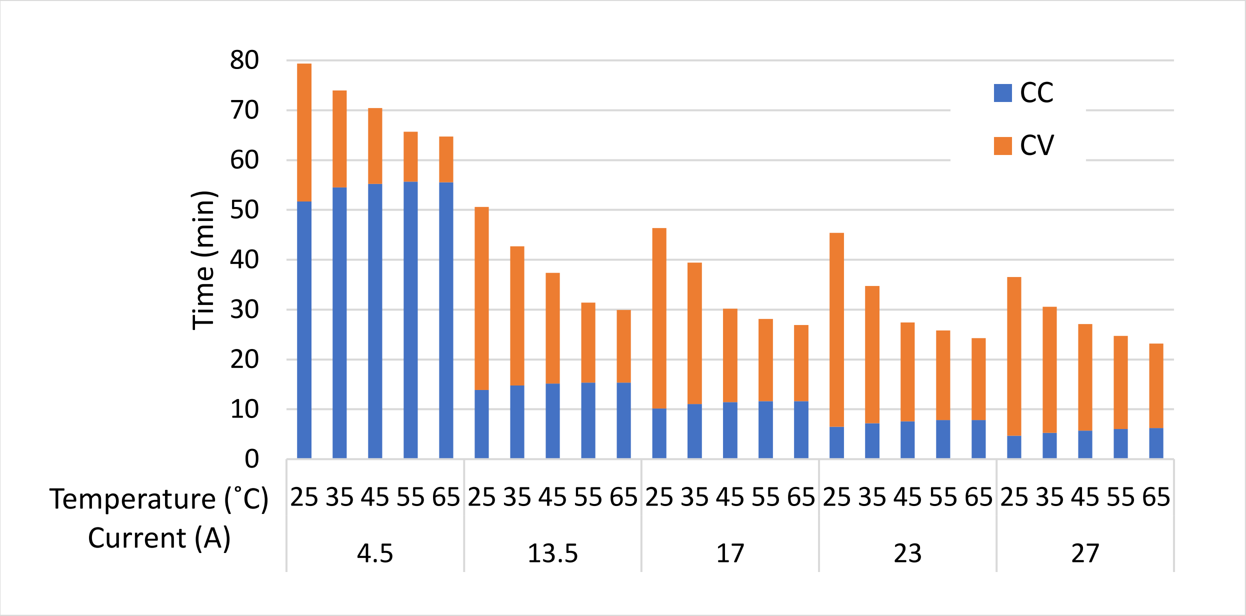

Figure 33 CC and CV Stage Charge Time Vs CC-Rate for Different Temperatures

The following observations can be made from Figure 33:

- Increasing temperature increases CC phase time. CC phase time is increased by 2 minutes when heated from 25 to 45 C but the CC stage charge times from 45, 55 and 65 C are within 0.5 minutes. Thus, diminishing returns on increased temperature occurs resulting in a flatlined performance. **This suggests that to lengthen the CC stage charge time and achieve the lowest charge time for a given rate, the cell should be conditioned to at least a temperature of 45 ˚C during CC stage.**

- Increasing temperature decreases CV stage time to a significant extent. For any given rate, increasing temperature from 25 ˚C to 65 ˚C reduces time in CV phase by at least 15 minutes. This is significant because 15 minutes is up to half the total charge time for some conditions. Unlike the CC stage charge time dependency on temperature, the CV stage time reduction with increased temperature does not flatline at the range of temperatures tested here. **This suggests that to minimize CV stage charge time, the cell should be conditioned to the maximum permissible cell temperature.**

- Increasing current reduces CC stage time to a diminishing extent and the relationship flatlines as rates approach the maximum tested. Elevated current increases the voltage drop across the cell and causes the cell to reach 4.2 V which terminates the CC stage earlier. Increasing current reduces CC stage time by about 4.5 minutes/A at low rates and 0.5 minutes/A as the rate approaches 27 A. The reduction of CC stage charge time is small in comparison to the charge time reduction achieved by increasing the rate. **This suggests that to minimize charge time, charge current should be maximized even though doing so results in reduced return at high rates.**

- Increasing current increases CV time to a small extent. Since increased current causes the CC stage to end earlier, the CV stage must deliver more capacity which takes more time. For low temperatures, increasing current from 4.5 A to 27 A increases CV stage charge time by 3 minutes and at high temperatures the CV stage is increased by 5 minutes. The small increase in CV time due to increased current is countered by the decrease in CC stage time due to increased current and thus a net reduction in charge time is observed. **Thus, the net charge time reduction observed suggests that increased currents should be used to minimize charge time regardless of increased CV time.**

5.3.1 Impact of CC charging on charge performance

Previously, charge performance analysis has centered on charging to full 100 % SOC, another perspective is to consider charging only in the CC stage. Table 9 provides the % capacity charged in the CC stage, CC stage charge time, and % capacity / minute. The charge capacity ratio gives the % SOC that the CC stage terminates which clearly shows how significant current and temperature impact capacity delivered during the CC stage. The CC stage charge times show that ultra fast charge times can be achieved if the CV phase is not used.

Table 9 CC charge capacity ratio (a), CC charge time (b), and % Capacity/minute VS temperature and rate

a) % Capacity Charged in CC Stage (%)		Temperature (˚C)				
		25	35	45	55	65
Rate (A)	4.5	90.2	93.6	95.0	95.9	96.2
	13.5	72.9	76.5	78.4	79.7	80.4
	17	67.5	72.0	74.5	76.1	76.7
	23	58.5	63.6	67.1	69.5	70.5
	27	51.0	56.7	60.7	63.6	65.7

b) CC Charge Time (min)		Temperature (˚C)				
		25	35	45	55	65
Rate (A)	4.5	51.7	54.5	55.3	55.7	55.5
	13.5	13.9	14.8	15.2	15.4	15.4
	17	10.2	11.1	11.4	11.6	11.6
	23	6.5	7.2	7.6	7.9	7.9
	27	4.7	5.3	5.7	6.0	6.2

c) % Capacity/ Minute (%/min)		Temperature (˚C)				
		25	35	45	55	65
Rate (A)	4.5	1.7	1.7	1.7	1.7	1.7
	13.5	5.2	5.2	5.2	5.2	5.2
	17	6.6	6.5	6.5	6.5	6.6
	23	9.0	8.8	8.9	8.8	9.0
	27	10.9	10.7	10.6	10.6	10.6

The following observations can be made based on the data in Table 9.

- Increasing charge rate reduces charge time and charged capacity in the CC stage. When the charge rate is in increased from 13.5 A to 27 A, the charge time is reduced from 14 minutes to 5 minutes. In this case the charged capacity reduces from 73 % to 51 %. **Increasing charge rate causes the cell to terminate the CC phase earlier which severely limits the capacity charged but can deliver substantial usable capacity a very short period of time.**

- Temperature is shown to impact the CC charge time and capacity to a lesser extent than the charge rate however increasing temperature does improve charge performance substantially. When charging at 27 A, increasing temperature from 25 C to 65 C results in a 1.5-minute extension to the 5-minute charge time which delivers 14.7 % more capacity than the 51 % delivered at 25 ˚C. **Thus, Increased temperature can considerably improve charged capacity even in the CC phase.**

- Charging only the CC phase is favoured because of the increased charge rate. However, remaining in the CC phase limits the accessible capacity. Charging to the commonly referred 80 % SOC in CC phase is only possible at the 13.5 A 65 C condition. **In most ultra fast charge conditions, CV phase is necessary for charging to 80 % SOC.**

- The % Capacity/minute is dominated by the charge current. Higher currents proportionally deliver capacity at higher rates and are not impacted by temperature. When temperature is increased, cell resistance reduces and extends the CC phase and maintains the same charge rate.

5.3.2 Impact of CV charge performance

To evaluate the impact on charge time that CV charging has, this chapter first plots the charge current vs capacity for multiple charge currents and temperatures.

Figure 34 gives the charged capacity on x-axis and the charge current on y-axis for each test condition. For each CC rate, plotting the charge current versus charged capacity highlights how for any rate, there is a maximum CV current as a function of charged capacity. The slope is related to temperature.

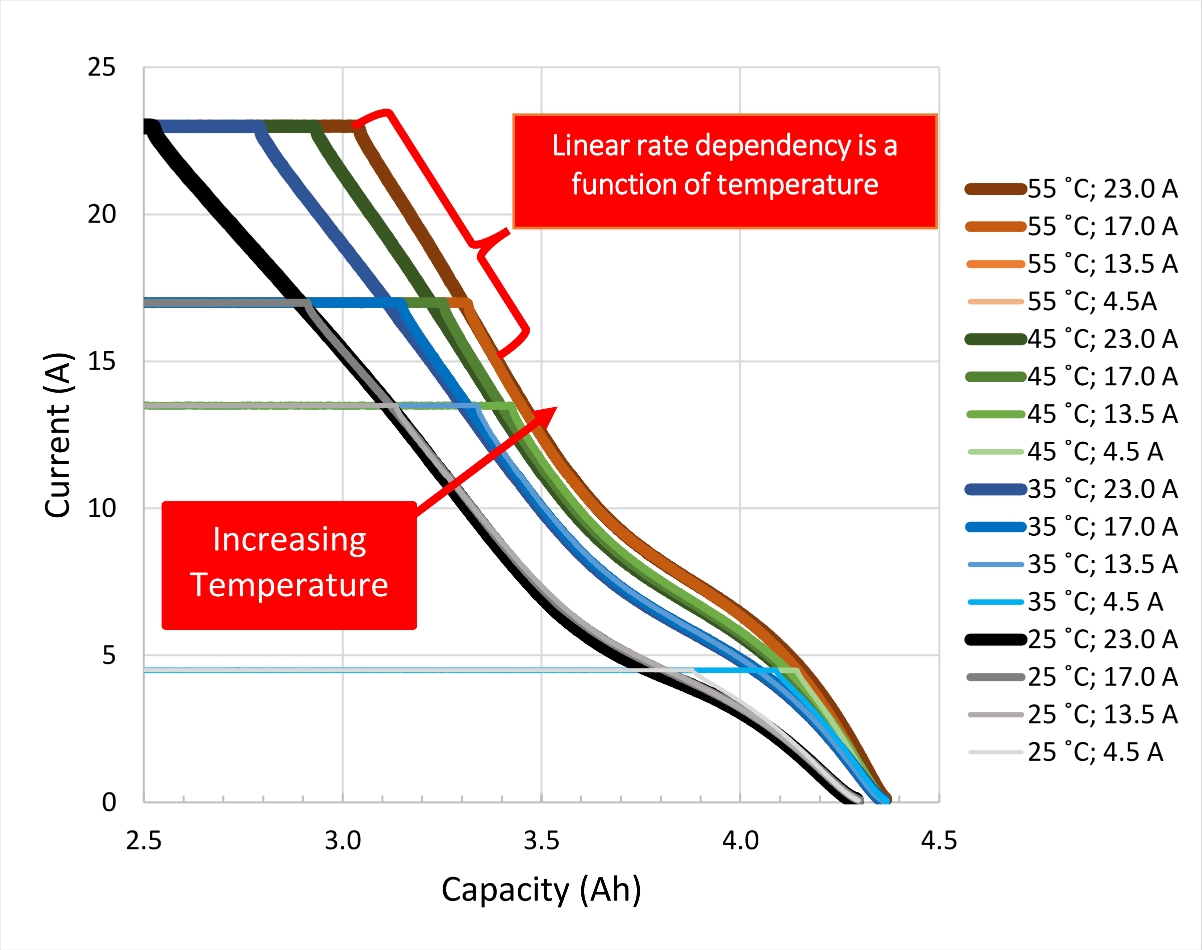

Figure 34 Charge current VS Capacity for Different Charge Conditions

The following observations are made regarding the linearized CV stage charge limits:

- When charging in CV at a given temperature, there is a corresponding linearly decreasing current limit as a function of charged capacity. **For a given temperature, the current limit VS charged capacity is the same regardless of what initial CC limit was used.**

- At higher temperatures the CV stage current rate decreases faster and begins to reduce at higher state of charge. More capacity is delivered in the CC phase at higher temperatures, so the cell is at a higher state of charge when CV initiates which causes the rapid reduction of CV stage charge rate.

- An S-curve in the charge rate is observed above 80% SOC. A reduction of the charge rate limit slope is observed between 80 and 90% which can be explained by relaxing electrolyte gradients supporting increased diffusion.

- At high charge rates (>13.5 A), the CV charge rate linearly decreases until approximately 3.5 Ah (~80 % SOC) where the rate at which the charge rate decrease reduces before rapidly decreasing again near 4.15 Ah or (95%). When charging above 90% SOC it is expected that charge transfer resistance dominates the current profile.

Figure 34 shows how the charge rate reduces with additional capacity when CV charging at a given temperature. However, the context of time is required to evaluate the difference between charge conditions. Table 10 gives the charged capacity and charge time in the CV stage.

Table 10 % capacity charge in CV stage (a) CV stage charge time (b), and % capacity/minute (c) VS temperature and rate

a) % Capacity Charged in CV Stage (%)		Temperature (˚C)				
		25	35	45	55	65
Rate (A)	4.5	9.8	6.4	5.0	4.1	3.8
	13.5	27.1	23.5	21.6	20.3	19.6
	17	32.5	28.0	25.5	23.9	23.3
	23	41.5	36.4	32.9	30.5	29.5
	27	49.0	43.3	39.3	36.4	34.3

b) CV Charge Time (min)		Temperature (˚C)				
		25	35	45	55	65
Rate (A)	4.5	27.7	19.5	15.2	10.0	9.2
	13.5	36.7	27.9	22.2	16.1	14.6
	17	36.2	28.4	18.8	16.5	15.3
	23	38.9	27.6	19.9	18.0	16.4
	27	31.9	25.3	21.4	18.7	17.0

c) % Capacity/min in CV Stage		Temperature (˚C)				
		25	35	45	55	65
Rate (A)	4.5	0.4	0.3	0.3	0.4	0.4
	13.5	0.7	0.8	1.0	1.3	1.3
	17	0.9	1.0	1.4	1.5	1.5
	23	1.1	1.3	1.7	1.7	1.8
	27	1.5	1.7	1.8	1.9	2.0

The following observations can be made based on the data in Table 9.

- Increasing temperature reduces the amount of time and capacity delivered in the CV stage. Increasing temperature from 25 to 65 ˚C reduced CV stage charge time from 27.7 to 9.2 minute.

- Increasing temperature during high-rate charging has a considerable improvement on the % capacity charged in the CV stage. For the 27 A case, increasing temperature from 25 to 65 ˚C shifts 14.7 % capacity to the CC stage and reduces CV stage charge time by 14.9 minutes. **Increasing temperature improves CV stage performance the most at high charge rates.**

- **The high temperature and high charge rate condition has the greatest % Capacity/ minute.** This can be explained by the increased average CV stage current at higher currents. High temperatures cause the average to increase by initiating the CV current taper later in the SOC. More capacity is delivered at a higher current for longer.

5.4 Impact of charge termination condition

When fast charging from 0 to 100 % SOC it has been established that the time spent in CV stage significantly influences the total charge time. By reducing the upper SOC limit, overall charge time will be reduced but less capacity will be delivered. This trade-off will be explored here to determine incremental benefits, and disadvantages, of terminating charge before reaching 100 % SOC.

In the personal electrical vehicle, light commercial use, or heavy commercial use cases, a charge session may be terminated for a variety of reasons. The socioeconomical and application specific constraints on charge termination condition are outside of the scope of this thesis but generic termination conditions will be considered here. Two of the most popular include terminating based on reaching a high SOC such as 80 or 90 % SOC or terminating based on reaching a reduced charge rate such as 50 % of initial charge rate. These termination conditions provide three critical states of charge which will be used to evaluate the charge time under different charge conditions. Next, the SOC, charge rate, and SOC delta (SOCΔ) versus time is compared at critical states of charge. Here the SOCΔ is the difference in state of charge between each temperature condition to that of the 25 ˚C case.

Figure 35 shows the state of charge, charge rate, SOCΔ versus time for a 23 A charge at four temperatures.

The charge rate is expressed in % capacity/ minute for convenient interpretation.

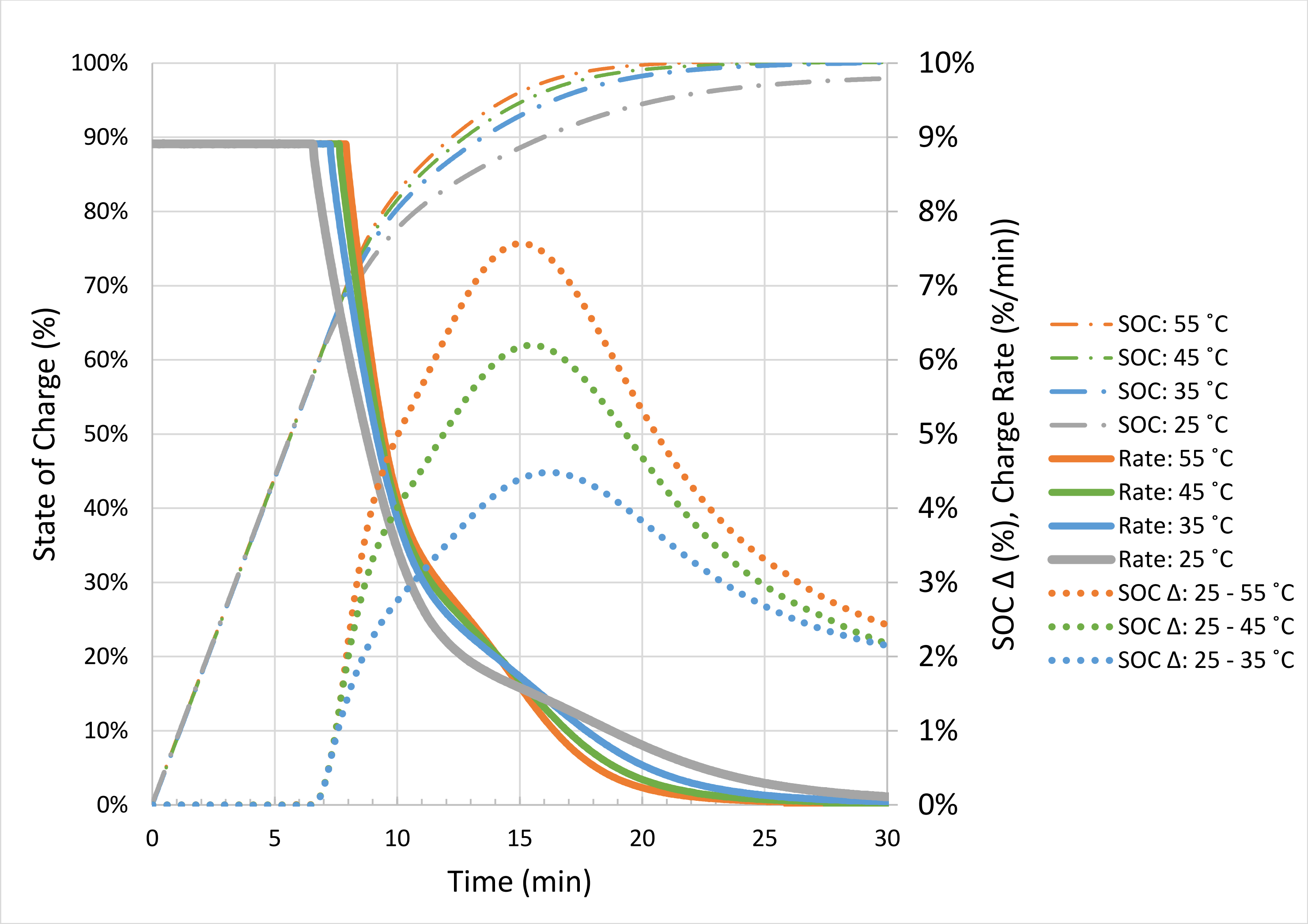

Figure 35 State of charge and state of charge difference to 25 ˚C versus time for 23 A charge.

The following observations of Figure 35 were made:

- Since all charges have the same CC stage current, the SOC of each profile increases at the same rate of 9 %/min during the CC phase and the SOCΔ is 0 for the first 6.7 minutes. The 25 ˚C condition reaches 60 % SOC before transitioning to the CV stage. **Elevating cell temperature does not improve charge times when the charge termination falls within the CC stage for conditions with the same CC current.**

- **The 55 ˚C 23 A charge condition results in the greatest SOCΔ of 7.5 % occurring at 15 minutes.** For the 35 and 45 ˚C cases maximum SOCΔ are found to be 4.5 and 6.1 % occurring at 16 and 17 minutes respectively. The delay in maximum SOCΔ for the lower temperature cases is in part due to the later onset of CV stage initiation. After 15 minutes the SOCΔ rapidly reduces and approaches 0. The time of maximum SOCΔ corresponds to the time at which the 25 ˚C condition current surpasses the current of the respective case.

- When charging to 80 %, increasing temperature from 25 to 55 ˚C reduces charge time from 10.4 by 1.1 minutes to 9.3 minutes.
- When charging to 90 %, increasing temperature from 25 to 55 ˚C reduces charge time from 15.3 minutes by 3.4 minutes to 11.9 minutes.
- The SOC that the charge rate reaches 50 % of initial rate is between 73 – 83 % SOC for all cases. At this point the SOCΔ is 5 % for the 55 ˚C case. **10 % more capacity is charged when the temperature is increased from 25 to 55 ˚C if the charge is terminated based on reaching a 50 % charge rate reduction**

Analysis of how much time each charge condition takes to reach a given SOC summarizes the tradeoff between charge time and capacity, for different temperatures, charge rates, and termination conditions. Figure 36 shows how charge time is impacted by selecting the end of charge termination SOC below 100 % for different charge rates at 25 and 55 ˚C. These results quantify the charge time benefit achieved by charging at high temperature for different rates.

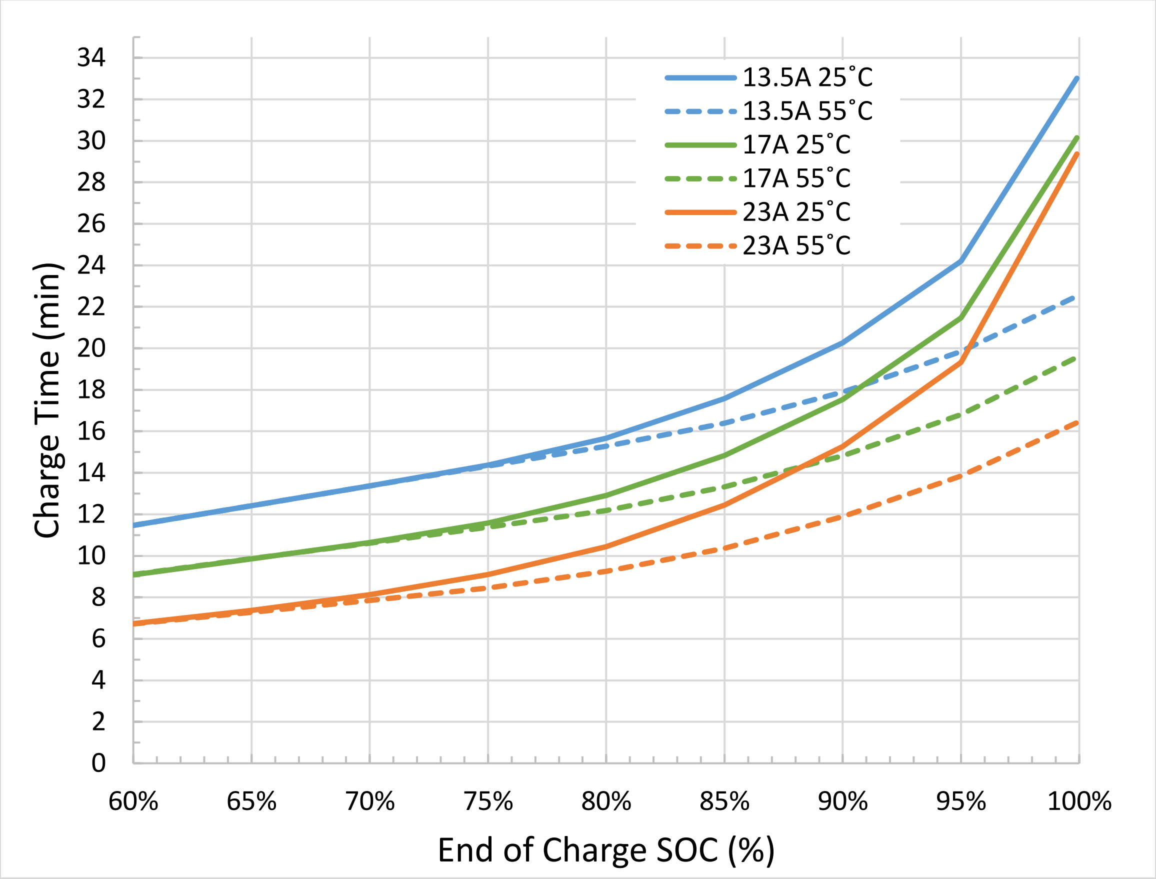

Figure 36 Comparison of Charge Time VS End of Charge SOC For Different Conditions

The following observations can be made regarding Figure 36:

- It takes the 25 ˚C case 10.6 minutes to get to 80 % and 15 minutes to reach 90 %. Whereas the 55 ˚C case takes 9.2 minutes to reach 80 % and 12.3 minutes to reach 90 %. **If charging to 90 %, heating to 55 ˚C can reduce charge time by 2.7 minutes (18 %) when compared to charging at 25 ˚C.**

- The charge time reduction from increasing temperature is greatest when charging to high states of charge (>95 % SOC). 13.5 A charging at 25 ˚C reaches 73 % capacity in the CC phase and when the temperature is increased to 55 ˚C, 79 % capacity is reached in CC phase. In comparing the charge times for 13.5 A at 25 ˚C to 13.5 A at 55 C shows that they have nearly identical (<1 minute difference) charge time at 80 % SOC but the 55 ˚C reaches 100 % SOC 10 minutes sooner. **Thus, the charge time reduction achieved by increasing cell temperature grows as the end of charge SOC is increased beyond the CC to CV transition point.**

5.5 Conclusions

This chapter presented results of charging a cell in various temperatures and at different fast charging rates which resulted in generation of performance surfaces useful for assessing the impact of charge conditions on the key charge metrics. Elevated temperature increases the average charge current and reduces charge time under all charge currents. During CC stage charging, cell wall temperature should be at least 45 ˚C to minimize charge time. During CV stage charging, cell wall temperature should be the maximum permissible. Maintaining high temperature in CV stages reduces total charge time by over 50 % in comparison to charging at 25 ˚C. Selecting charge termination SOC at or below 90 % can significantly reduce the total charge time.

Chapter 6 Response to thermal profile during fast charging

Performance mapping in chapter 5 identified that elevated temperature can significantly reduce the total charge time by reducing time spent in the slow charging CV stage. However, performance mapping was conducted in isothermal conditions and did not consider the impact of dynamic cell temperature changes before or during the charge. In this chapter, these effects will be explored by comparing the result of applying a step change the cell temperature at 3 different points during a charging session. One isothermal condition and three unique step change temperature profiles were applied. Condition 1 was isothermal at 25 ˚C, condition 2, 3, and 4 were a step change in temperature from 25 °C to 45 °C initiated 5 minutes before starting charge, at the start of charge, and 1 minute before the start of CV respectively. Dynamic thermal profiles used are summarized in Table 11:

#	Test	Charge Condition	Discharge Condition
1	Isothermal 25 ˚C	Constant 25 ˚C ; 13.5 A 4.2 V CC-CV to 0.1 A	25 ˚C; 4.5 A CC to 2.5V
2	5 min precondition	25 to 45 ˚C step change five minutes prior to initiation of CC charge stage; 13.5 A 4.2 V CC-CV to 0.1 A	25 ˚C; 4.5 A CC to 2.5V
3	CC Stage heat	25 to 45 ˚C step change at initiation of CC charge stage; 13.5 A 4.2 V CC-CV to 0.1 A	25 ˚C; 4.5 A CC to 2.5V
4	1 minute prior to CV stage heat	25 to 45 ˚C step change 1 minute prior to initiation of CV charge stage ; 13.5 A 4.2 V CC-CV to 0.1 A	25 ˚C; 4.5 A CC to 2.5V

Table 11 Test procedure for evaluating affect of asymmetric temperature modulation.

The isothermal condition was selected to provide comparison and to benchmark the temperature dependant CV stage current limit. Condition 2 reflects the most common existing method for fast charging where the battery is pre-conditioned prior to initiating charging. This method is simple but does require communication between vehicle operator and BMS to know when to initiate pre-heating. This method is common because existing systems have low temperature ramp rates which take considerable time to increase cell temperature. Heating at the start of CC charge in condition 3 is the simplest method but in recent practice is also the most performance limited because it may reach BMS programmed limitations. Initiating heating at the start of charge does not permit time for the cell to reach an elevated temperature prior to applying high current. Initiating charge at low temperature may cause charge rate limitations caused by either reaching the CV phase early or by reaching elevated risk conditions for lithium plating. Initiating the step change 1 minute prior to the CV phase ignores risk of plating at low temperatures and represents the option with minimal energy and time input dedicated to preconditioning. Theoretical temperature setpoint and measured cell wall temperature timeseries is compared in Figure 37.

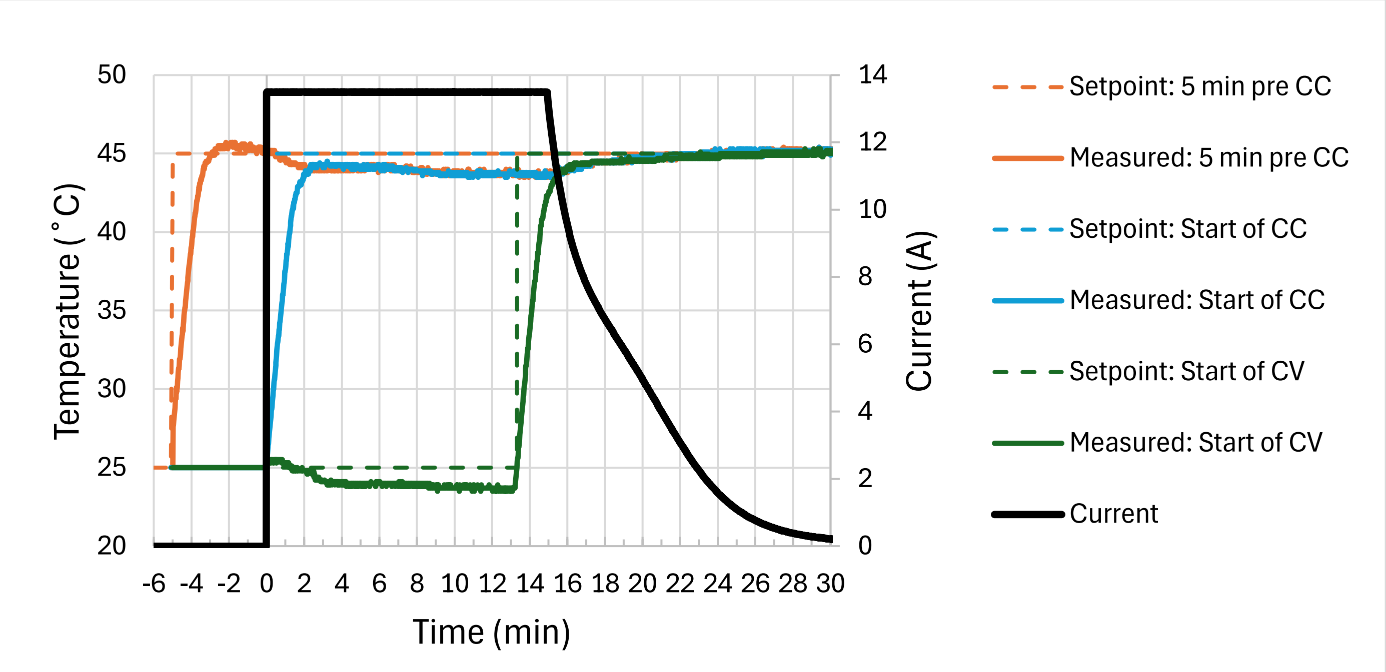

Figure 37 Measured Temperature and current VS time for 13.5A Charge with Different Thermal Conditions

The step change from 25 to 45 °C reaches within 2 standard deviations in less than 1.5 minutes for all tests. Conditions 3 and 4 have the step change occur during the CC stage. For these cases, the step change is completed within 0.5 Ah (10 % SOC) window. The temperature overshoot and offset observed after reaching the setpoint is due to the experimental setup and PID control over cell holder. Offset deviations from setpoint temperature that occur and are limited to within 1.5 ˚C.

The manufacturer rated 13.5A was selected as the CC charge rate. All discharges were 4.5 A CC to 2.5V and conducted at isothermal 25 ˚C. For each condition, the cell was first cycled three times isothermally at 25 ˚C to benchmark performance and to confirm repeatable cycle capacity. Then a thermal profile was applied for the next three cycles. Following the thermal profile cycling the cell was subjected to 3 isothermal cycles to reset and prepare for thermal profile cycling again.

6.1 Comparison of thermal profiles

Figure 38 shows the charge current, state of charge, and state of charge delta (SOCΔ) versus time during the charge for each thermal profile. The SOCΔ is the difference between the state of charge for each condition and the 25 ˚C isothermal condition.

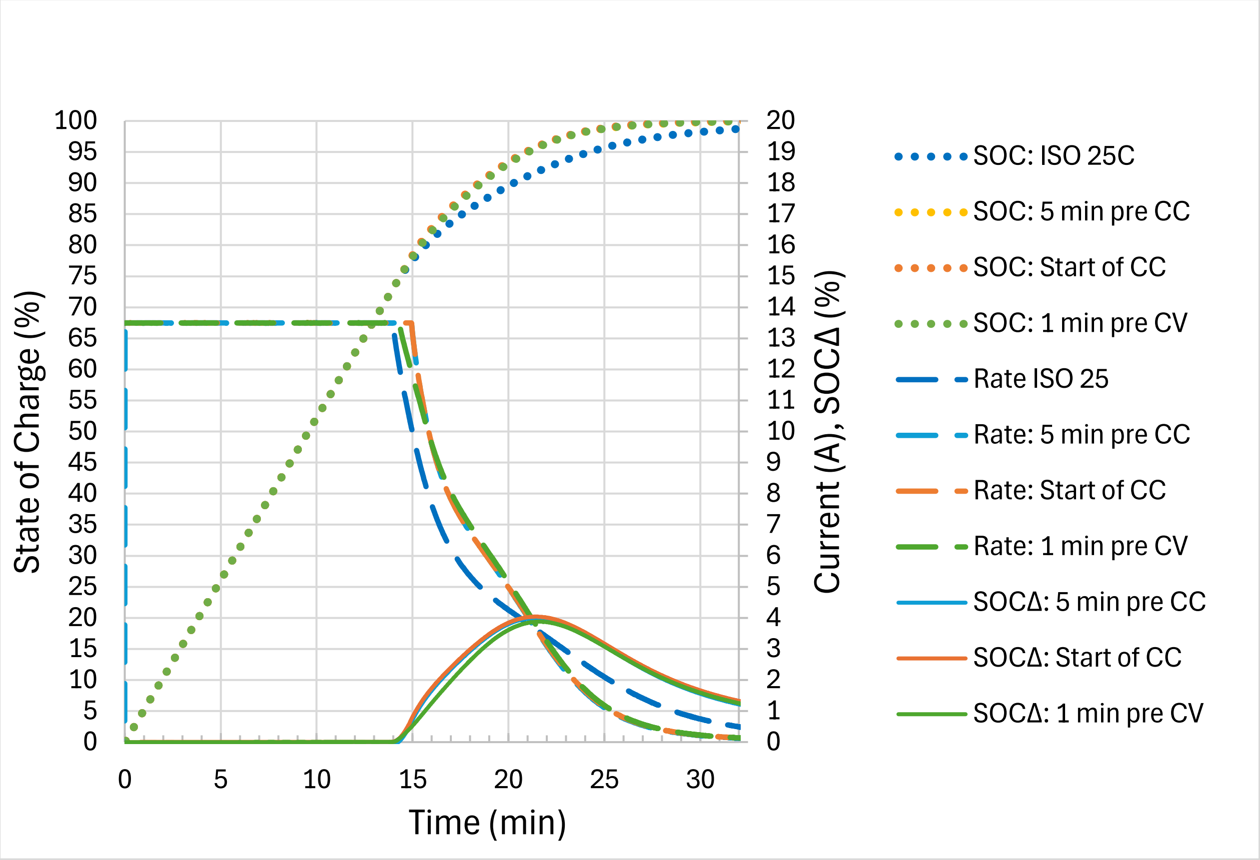

Figure 38 Charge Rate and State of Charge VS time during 13.5 A Charges with Different Thermal Profiles

Comparing the charge current and state of charge versus time for the different thermal profiles shows that increasing temperature 1 minute before the CV phase results in an equivalent charge time with equivalent charged capacity in comparison to charge profiles which are at elevated temperature for both CC and CV. 25 ˚C isothermal condition (Condition 1) is the first case to transition to the CV phase after 14 minutes because it is the case with the highest cell resistance due to lower temperature. The current rapidly drops to 50 % of the initial 13.5 A two minutes after starting the CV phase. Conditions 2 and 3 show identical current and state of charge profiles suggesting that the cell operates with the same temperature distribution throughout the entire charge. Therefore, no difference between heating 5 minutes before or heating at the start of CC charging is observed with respect to charge time or capacity. Conditions 2 and 3 remain in the CC phase for an additional 1 minute longer than the 25 ˚C case which demonstrates how charging at elevated temperature can briefly extend the CC phase.

Condition 4 (heated 1 minute prior to CV) transitions from CC to CV 25 seconds after condition 1 and its current reduces at a lower rate. Aside from the earlier CV initiation and current reduction, the current profile of condition 4 is similar to conditions 2 and 3. During the CV stage between 80 and 90 % SOC the charge current of condition 4 is slightly (~0.1A) higher than conditions 2 and 3. The difference in current is enough to cancel out the earlier CV initiation that condition 4 experiences. The previously introduced temperature dependant CV charge rate limit is observed to be followed. Increasing cell temperature during CV results in the cell following the 45 ˚C CV rate limit resulting in reduced charge time and equivalent charged capacity.

The SOCΔ shows how after condition 1 reaches CV, conditions 2, 3, and 4 remain at a higher SOC for the duration of the charge reaching a maximum SOCΔ of 4 % occurring at 21.5 minutes. Condition 4 lags behind conditions 2 and 3 by at most 0.5 % and catches up to within 0.1 % by the maximum SOCΔ point. At the maximum SOCΔ point condition 1 is at 92 % SOC whereas conditions 2-4 are at 96 % SOC. After the SOCΔ maximum point, the charge current in condition 1 is greater than the other conditions and therefore the SOCΔ gradually reduces to 0.

Table 12 summarizes the charge capacity and time for the 5 different thermal profiles:

Table 12 Summary of dynamic thermal charge profiles

Condition	Iso 25	5 min preheat	Start of Charge	1 min prior to CV
#	1	2	3	4
Charged Capacity (Ah)	4.2838	4.297	4.304	4.300
Average of conditions 2-4 (Ah)		4.300		
Delta From Average %	-0.02	-0.08	+0.08	0.00
Time (min)	41.97	32.95	33.05	32.97
Average of conditions 2-4 (min)		32.99		
Delta from Average %	+8.98	-0.12	+0.18	-0.07

For the CV heated case, the total charge time and charged capacity was identical to the start of charge and 5 min pre heat cases. This important observation suggests that a significant reduction in charge time can be realized by heating right before the transition to the CV stage which may enable reduced lifetime degradation through reduced time at elevated temperatures. Further studies are required to investigate if the reduction of short-term exposure to elevated temperatures during high charge rates is significant enough to reduce degradation. Previously developed models which consider both calendar and cycling degradation should be applied to this scenario (Bui, 2021).

Improved fast charging performance achieved by heating in only the CV phase suggests that **charge thermal profiles should be adapted to allow the cell to reach elevated temperatures just in time for the CV phase to start.** This approach could reduce time waiting for pre-conditioning to start and make use of internal cell heating to reduce energy spent by the TMS to condition the battery.

6.2 Conclusions

This investigation of dynamic temperature profiles demonstrated that by heating the cell immediately before it reaches 4.2 V a reduction of cell resistance occurs enabling extension of the CC phase and maintaining elevated temperature during CV phase reduces total charge time significantly. Heating in only the CV phase results in 4 % more capacity charged after 21-minute charge when compared to charging in the isothermal 25 ˚C condition. Future work should investigate the degradation effects of dynamic charge profiles including evaluating the impact of time spent at elevated temperatures on capacity and resistance degradation.

Chapter 7 Internal temperature during high-rate charging

A primary relationship of interest is the radial temperature gradient between internal temperature of the cell to the wall temperature with respect to charge condition. It is expected that higher charge rates result in higher radial temperature gradients. The temperature gradients at high rates may cause uneven electrode resistance and electrode use which may lead to accelerated degradation or core overheating. Thus, techniques are needed to measure internal cell temperature to evaluate its relationship to charge conditions.

This chapter first presents an internal temperature sensor instrumentation technique and verifies sensor insertion does not impact cell performance using temperature, capacity, and efficiency analysis of 1 hour CC-CV cycles. Cycle metrics including maximum temperature, discharge capacity, and efficiencies are compared before and after instrumentation.

This chapter also investigates the ability to maintain cell temperature to a setpoint for a traditionally used air chamber and a new isothermal cell holder. To compare the charge performance in air chamber and isothermal cell holder, cells were subjected to three CC-CV charge rate conditions (4.5, 9.0, 13.5 A) and three wall temperatures (10, 25, 45 ˚C) while instrumented with an internal temperature sensor. Cell wall and internal temperature are compared during the 9 conditions. The resulting datasets quantify the relationship between charge rate, wall temperature, and internal temperature rise.

7.1 Instrumentation technique

Prior to temperature sensor insertion, benchmarking of cell performance was completed using the standard twenty conditioning cycles. Following cell drilling, the twenty cycles was conducted again to permit comparison of cell temperature and efficiencies before and after drilling. An Omega TJ36-CPSS-020U-12 thermal probe was used for internal cell temperature measurement. The thermocouple is contained within a 0.508 mm diameter stainless steel probe. The temperature was recorded at 1 Hz using T-type thermocouple ports on the Neware cycler.

Temperature sensor insertion begins with instrumenting the cell wall with an Omega SA1-TI-1M T type pad mount sensor and connecting voltage sensing leads to a Fluke 289 multimeters. Both temperature and voltage are recorded using the Fluke meters for 12 hours prior to, during, and following sensor insertion.

To instrument cells with the thermocouple a repeatable procedure was used:

1. Nickel strip was spot welded to the negative and positive tabs as shown in Figure 23.
2. Location of the drill hole was marked based on previous cell dissection and inspection. The hole was offset from the center by 0.7 mm to avoid drilling through the negative terminal spot weld.
3. A #0 (0.793 mm equivalent) center drill was used to drill through the steel case stopping when copper foil was visible. A vacuum was used to remove filings during drilling
4. The copper negative terminal current collector was punched with a dental tool. The hole was visually inspected to be at least 0.5 mm in diameter. Cells which had been cycled released gas when punched. Gas release was not heard in fresh cells.
5. The thermocouple was inserted to pre-determined depth. In this study the thermocouple was inserted to mid cell location (35 mm from the cell negative terminal). The location was later verified with CT scanning technique. A slight bow over the 35mm section was made such that the sensor would contact the inner jellyroll wall.
6. The thermocouple was supported in location and Permatex steel weld epoxy was applied surrounding thermocouple for structural support and sealing electrolyte. The epoxy was let to harden such that it was tacky to touch and not liquid. If liquid epoxy is used, gas within the cell

could bubble out. The support was shown to maintain thermocouple location even during probe movement outside of the cell.

Figure 39 shows the drilling apparatus and an instrumented cell.

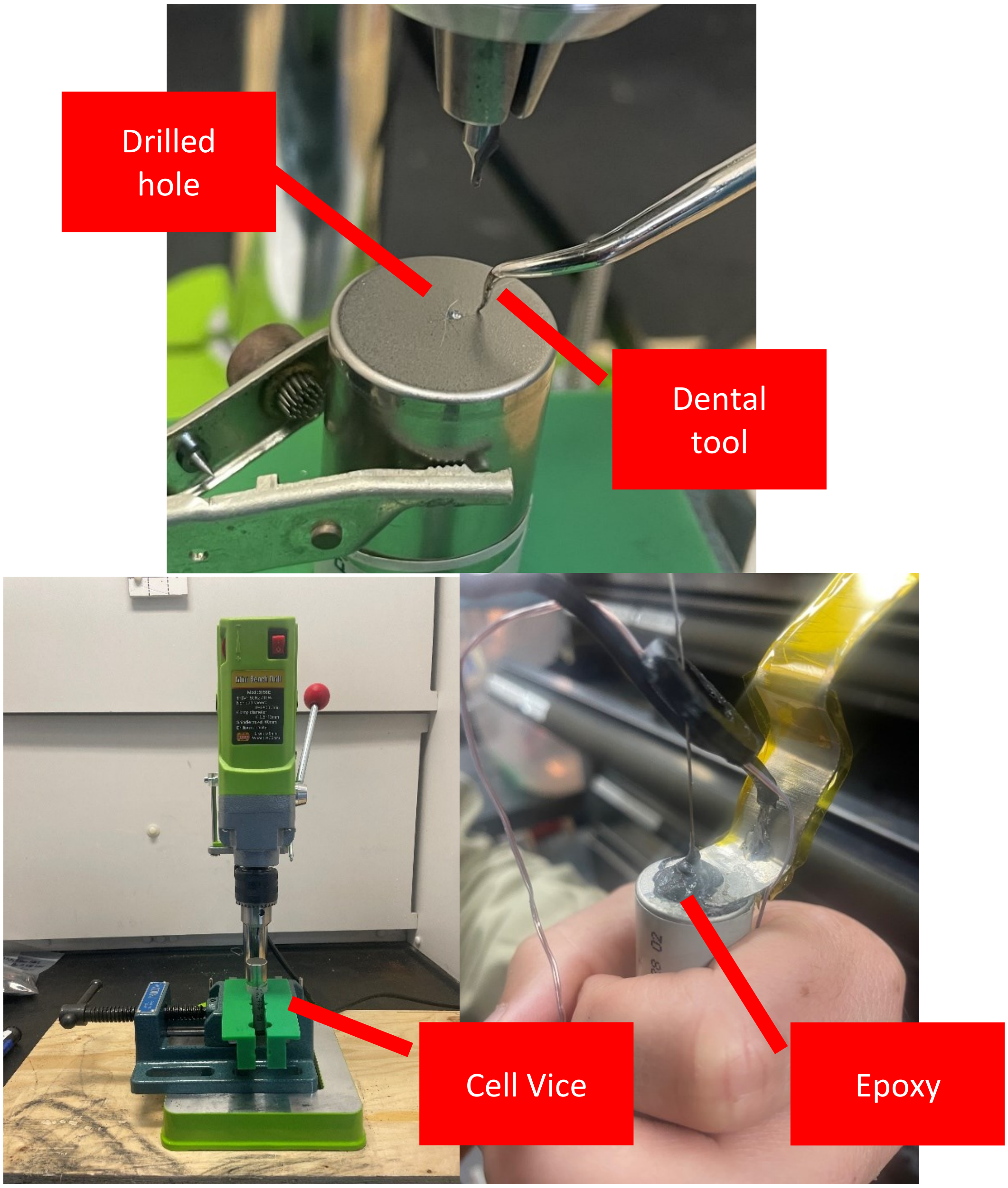

Figure 39 Cell drilling apparatus and instrumented cell

To identify the location of internal thermocouple and its impact on the negative tabs, a cell was drilled, probed, and carefully dissected to remove the jellyroll without disturbing the tabs. The processes used to insert the sensor, where a drill removes the steel can material and a dental tool punctures the copper tab prohibit intrusion of metal filings. A probed cell was dissected an no filings were found. Figure 40 shows a thermocouple in position.

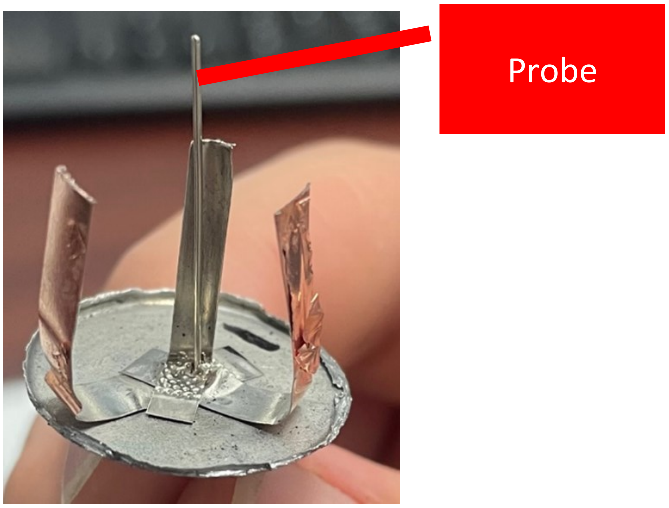

Figure 40 Thermocouple impact on cell tabs.

7.2 Evaluation of instrumentation impact

To evaluate the impact of temperature sensor instrumentation on cell tabs and jellyroll, CT scanning and a cycling was conducted prior to and following instrumentation. CT scanning determined the precise location of the thermocouple and cycling determined that the instrumentation did not impact performance.

7.2.1 CT scanning of instrumented cell

CT scanning cells was difficult due to size constraints (35 x 70 mm) within the Brukker Scanner. To mount the instrumented cell within the volumetric constraints of the brukker, the thermocouple wire was folded and wrapped around the cell. Figure 41 through Figure 43 show CT scans of an instrumented cell. Figure 41 shows the cell cross section at the location of the insertion.

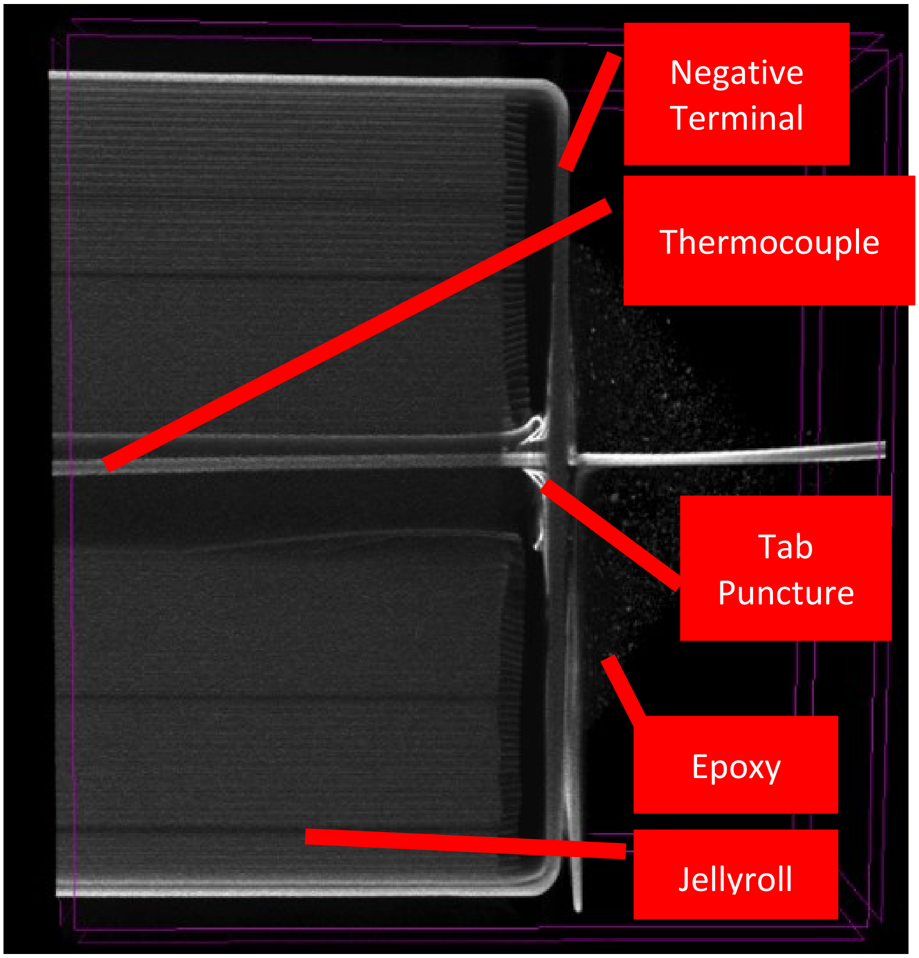

Figure 41 Axial Cross section of cell after temperature sensor instrumentation.

Figure 41 shows the impact that drilling and inserting a temperature sensor has on the cell tab. One concern with drilling through the negative terminal is that the reduction in tab cross sectional area could increase the tab resistance. The drill hole and sensor were narrowly within the open 2.8 mm diameter jellyroll core and the probe does not impact the jellyroll or tabs. The punctured copper tab does appear to protrude into the jellyroll core and is close to impacting the jellyroll (~0.2 mm clearance). The punctured copper tab does appear to rely on the lack of jellyroll in the first 1.5 mm of cell. Viewing the protrusion with a radial cross section in Figure 42 shows that the punctured copper does maintain adequate distance from the jellyroll radially.

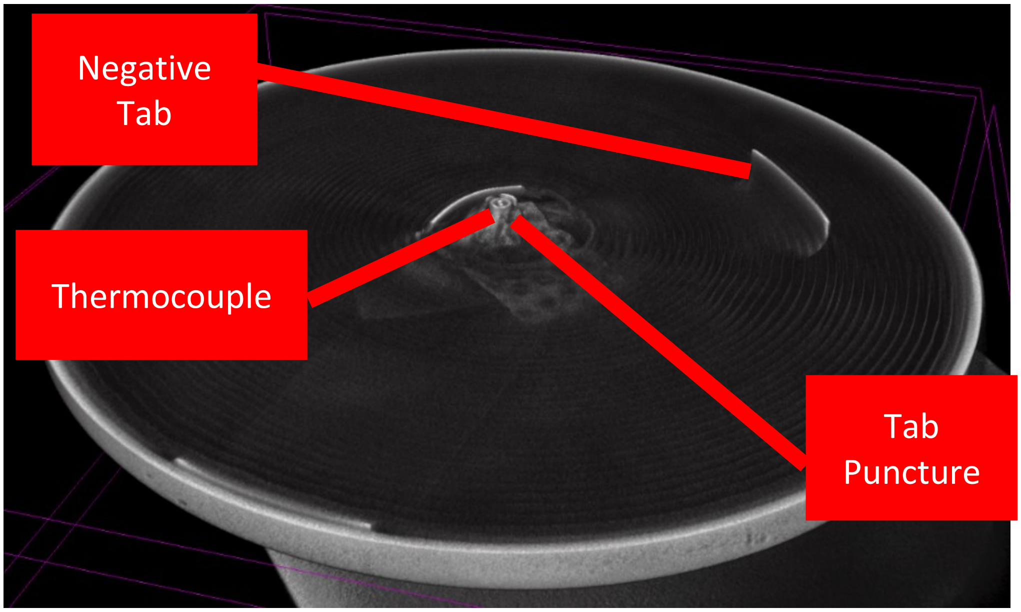

Figure 42 Radial cross section of cell after temperature sensor instrumentation

Since the temperature sensor is a thermocouple and measures at the tip of the probe, understanding the location of the thermocouples tip is critical. Figure 43 shows the cell cross section at the location of the thermocouple tip.

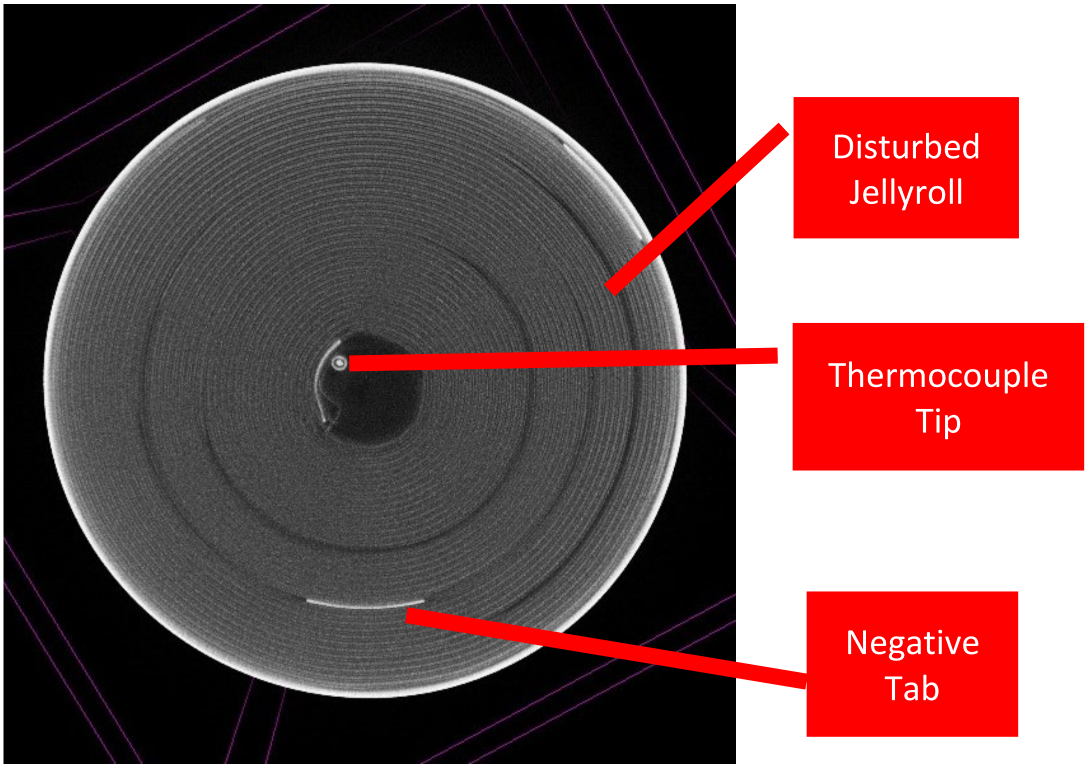

Figure 43 Cross section of cell at thermocouple location

Figure 43 shows the thermocouple does contact the jellyroll at the tip. This is due to a purposefully placed slight bend in the thermocouple wire prior to insertion.

7.2.2 Cycle performance analysis

To verify cell performance is not impacted by instrumentation, a series of cycle tests were run on the instrumented cells. Following cell drilling, the set of tests is run again to permit comparison of cell temperature and efficiencies before and after drilling.

The set of benchmarking tests conducted is described in Table 13.

Table 13 List of tests for comparing internal temperature to external temperature with and without isothermal wall

Name	Description
Conditioning cycling	Twenty 1 h CC cycles. Used to ensure SEI is fully formed on new cells. Monitoring capacity and efficiency evolution confirms formation.
Reference Performance Test (RPT)	Three 1 h CC cycles. Useful for identifying cell capacity over lifetime.
Increased rate cycling	CC-CV charging at 4.5, 9.0 and 13.5 A at 25 ˚C and discharging at 4.5A. This test identifies changes in cell internal heating.

Each instrumented cell was cycled twenty times before and after instrumentation in air chamber set to 25 ˚C at 4.5 A rate. Instrumentation of the cell occurred after completion of cycle 20. The following results investigate the cell capacity and temperature during cycles before and after instrumenting. The energy efficiency, coulombic efficiency, discharge capacity, and maximum cell temperature during cycle are indicators of cell performance and are plotted in the following figures. Figure 44 gives cell energy and coulombic efficiency before and after drilling.

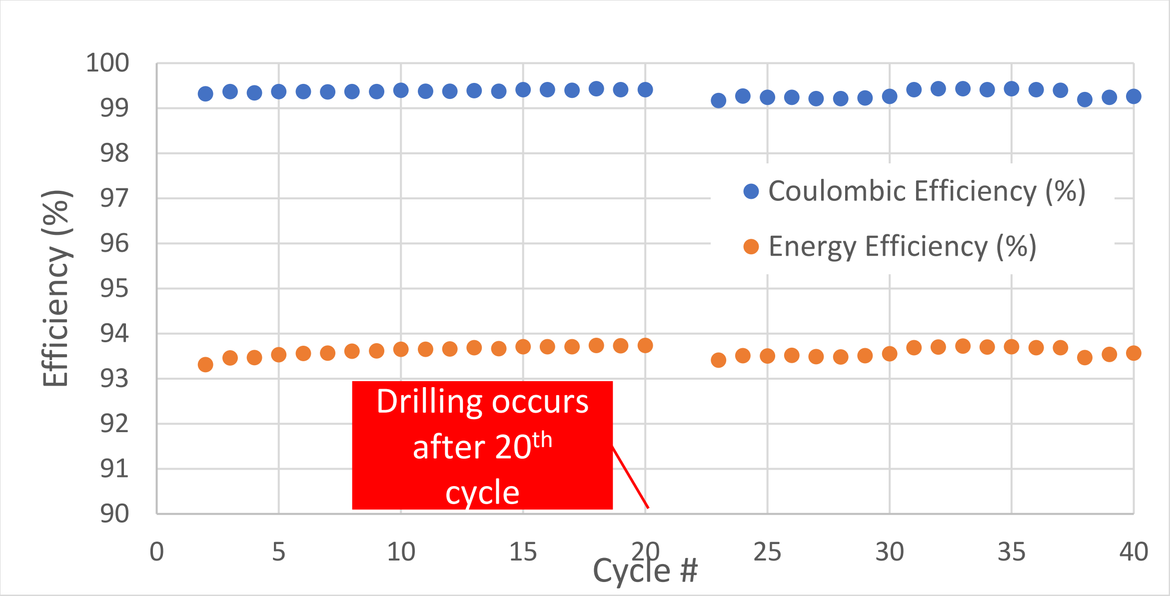

Figure 44 Cell efficiency before and after temperature sensor instrumentation

The cell efficiencies are noted to vary more after drilling. The 0.25 % variance in efficiency after drilling can be attributed to the use of the spot-welded nickel strip for the negative terminal connection. This experimental setup and cycling protocol were sensitive to slight inconsistencies in the cell positioning.

Another measure of cell performance useful for comparing cell temperature before and after drilling is the maximum temperature at the end of a cycle. Cell temperature is strongly related to internal resistance and therefore essentially tracks the stability of cell resistance. Figure 45 shows the maximum temperature reached during the 4.5 A CC discharge and discharge capacity during 40 cycles.

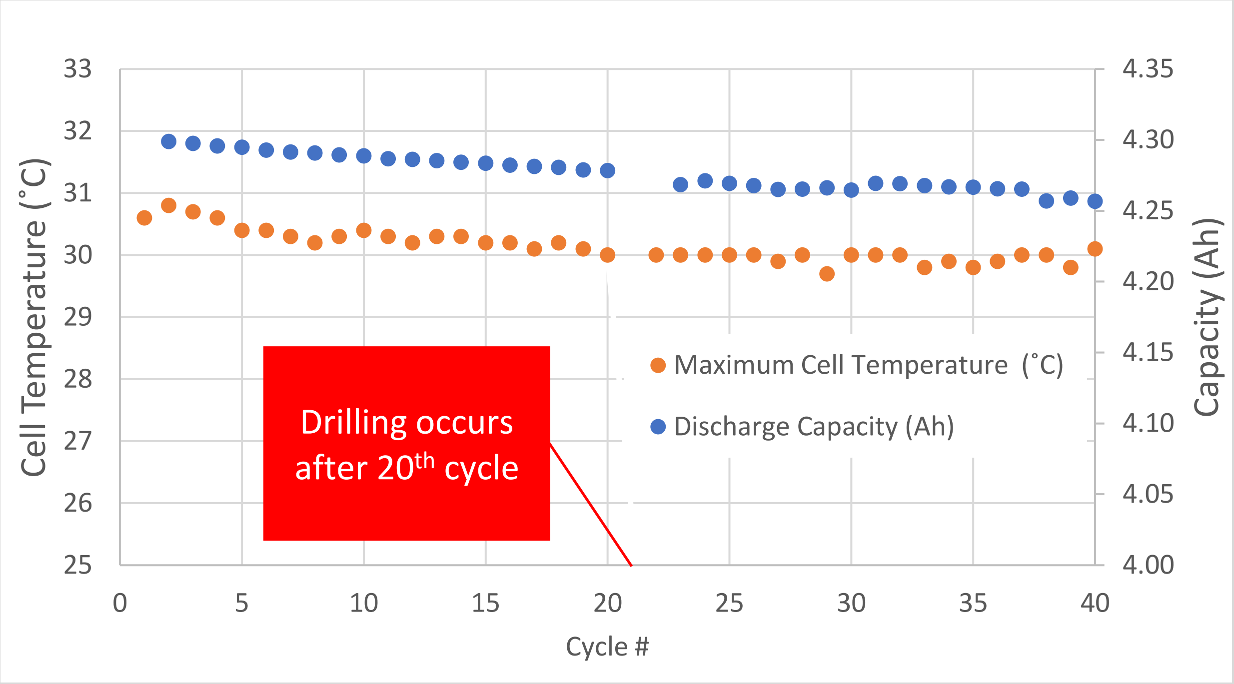

Figure 45 Maximum temperature reached and discharged capacity during 4.5A CC discharge

Figure 45 shows the maximum temperature during 4.5A discharge remains constant during before and after drilling. A decaying temperature followed by a consistent temperature is expected as the fresh cell completes its conditioning. The reduction in temperature follows the observed increase in energy efficiency. This is an indicator that the drilling did not adversely affect the cell since if the resistance were to increase, it is expected that the cell would produce more heat and reach a higher temperature at end of discharge. In summary, analysis of cell discharge capacity, efficiencies, and maximum temperature during discharge demonstrates that the drilling procedure does not affect the cells performance.

7.3 Convective and isothermal condition cycling

An internal temperature sensor instrumented Moli P45B cell was cycled in both air chamber and isothermal cell holders both set to 25 ˚C. Three cycles of CC-CV charging at rates 4.5, 9.0, and 13.5 A up to 4.2 V with 0.1 A CV cutoff current was conducted. Constant current discharges were at 4.5 A to 2.5V.

This chapter first presents results in the convective conditions, then follows with isothermal condition. The convective condition thermal control method used here was shown to poorly control cell wall temperature during high-rate charges whereas the isothermal cell holder was capable. The chapter concludes with analysis of how charge condition impacts internal temperature.

7.3.1 Convective condition

Figure 46 shows cell internal and wall temperature versus charged capacity for three charge rates in air chamber set to 25 ˚C.

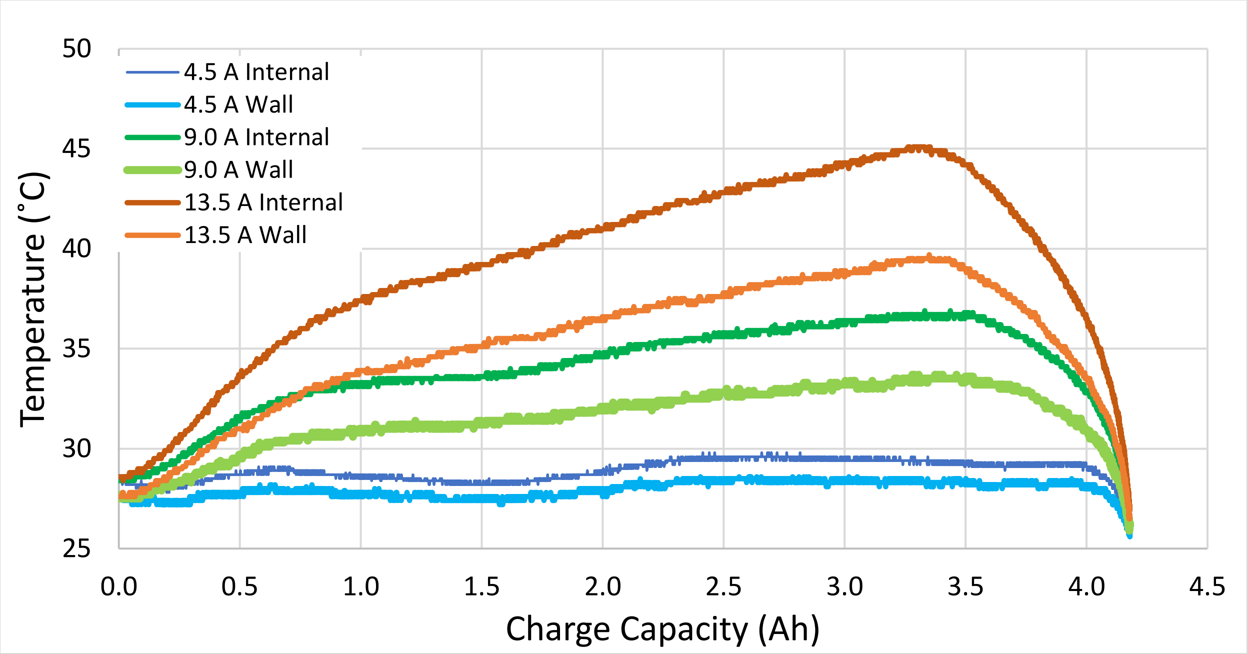

Figure 46 Cell Wall Temperature VS Charged Capacity for Different Rates

Figure 46 shows that for rates above 4.5 A, cell internal temperature is substantially higher than the environmental temperature of 25 ˚C and increases throughout the charge as heat generated is stored in the cells thermal mass. The cell wall temperature increases to 40 ˚C during the 13.5 A charge which is a 15 ˚C delta from the environmental air. At ~3.3 Ah, the internal to wall temperature difference is 6 ˚C. For the 4.5 A charge, the cell wall temperature increases to about 27 ˚C and maintains a 1 ˚C difference. Based on the considerable temperature increase at the 13.5 A rate, the air chamber is demonstrated here to not be able to maintain the cell temperature when high currents are applied. Increased rates beyond 13.5 A such as those needed to reach sub 10-minute charging times can not be reliably tested in the air thermal chamber as tested in this experiment.

Although at high charge rates the air chamber has been proven to not adequately isothermally control cell wall temperature, the comparison of cell internal temperature to wall temperature can still be made. The radial temperature gradient is due to internal thermal properties and not the heat transfer on the outside of the cell. However, the internal properties like heat generation are expected to change as the internal resistance reduces due to the average cell temperature rising above the setpoint. Figure 47 shows the radial temperature gradient. Here the thermal gradient from cell external wall to jellyroll core reaches up to 5.8 ˚C at the 13.5 A rate, 4.5 ˚C at the 9 A rate, and 1.5 ˚C at the 4.5A rate.

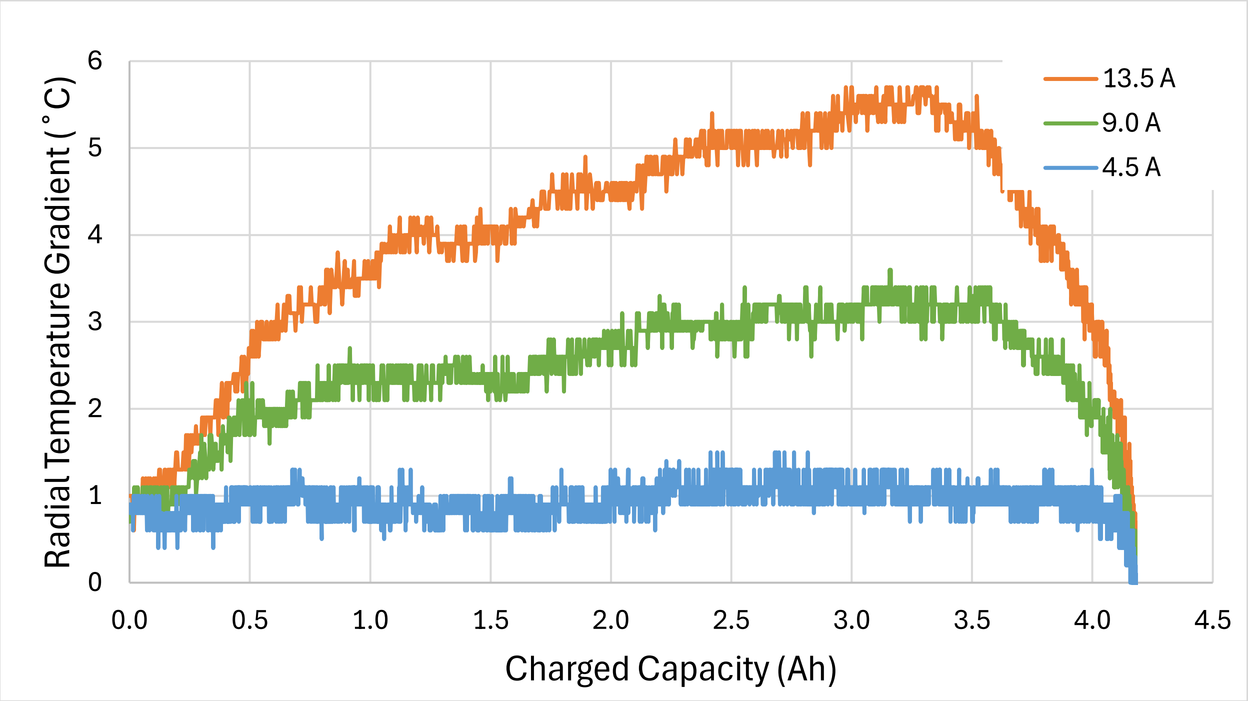

Figure 47 Radial temperature gradient for three current rates in air chamber set to 25 ˚C

7.3.2 Isothermal condition

The results in the isothermal condition differ from the air chamber. Figure 48 shows the cell wall and internal temperature during charges at 4.5, 9.0, and 13.5 A in the isothermal cell holder.

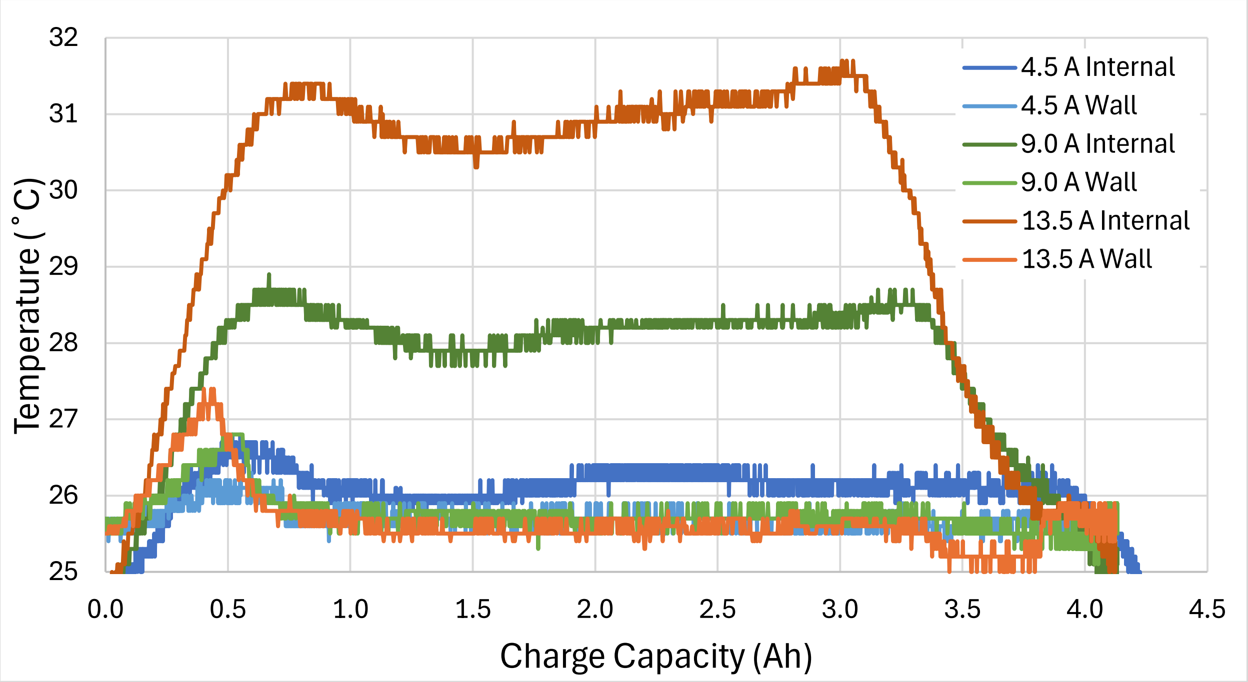

Figure 48 Cell internal and wall temperature during isothermal wall cycling at different rates at 25 ˚C setpoint

The isothermal cell holder was shown to hold cell wall temperature to within 1 ˚C of setpoint temperature on average. However, at the start of the 13.5 A charge, the cell wall temperature is observed to rise above the setpoint. The magnitude of temperature rise is dependant on the charge rate. At the 13.5A rate, the wall temperature reached 27.5 C briefly. The brief temperature deviation from the setpoint near the start of charge can be attributed to the isothermal PID controller. The controller exhibits a delay in the cooling of the isothermal block resulting in the cell temperature rise. Improved PID tuning could reduce the temperature delta further. Reducing the temperature rise to maintain improved isothermal conditions could affect the cell internal temperature. In all cases, the brief temperature rise is rapidly reduced and setpoint temperature is maintained throughout the bulk of the test. Thus, the isothermal rig can adequately control isothermally control cell temperature at high charge rates. Further analysis of internal temperature response to charge condition follows in chapter 7.4.

7.4 Cell internal temperature response to charge condition

The radial temperature gradient versus charged capacity for different charge current rates and isothermal wall temperatures is given in Figure 49.

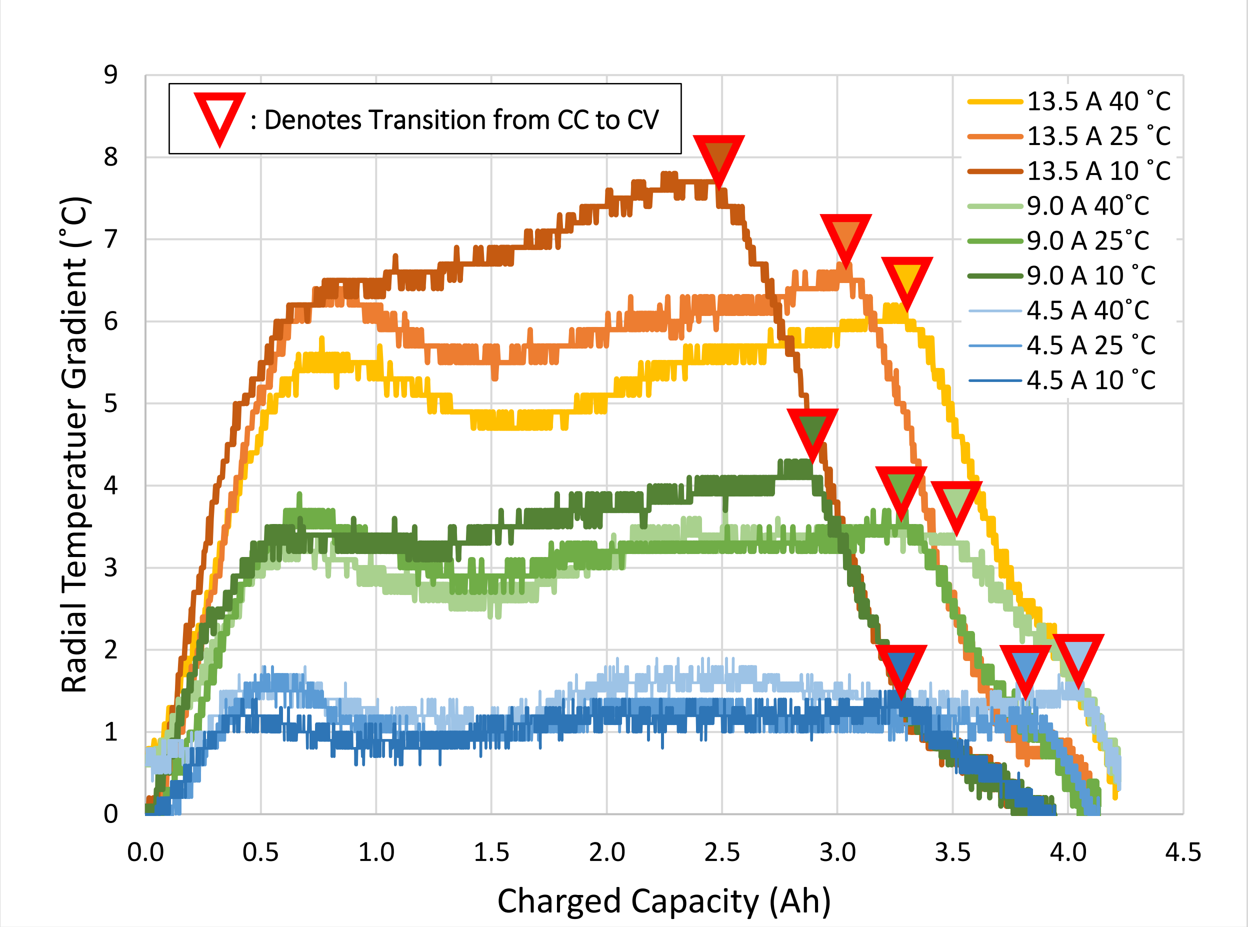

Figure 49 Radial temperature gradient versus charge capacity for different charge currents and isothermal setpoint temperatures

The following observations can be made:

- Charges with the same temperature follow the same temperature versus capacity curve during the CV stage. This is due to the strong temperature dependence of resistance which limits the current and heat generation during the CV stage.
- The greatest radial temperature gradient was 7.8 ˚C which was observed at the 13.5 A and 10 ˚C case. This is to be expected as the greatest heat generation occurs at high rates and low temperatures.
- Comparing the maximum temperature for the 13.5 A cases highlights the importance of increasing cell temperature at high charge rates. The 13.5 A 40 ˚C case had a maximum core rise of 6.2 ˚C which is a 1.6 ˚C improvement on the 13.5 A 10 ˚C case which had a maximum rise of 7.8 ˚C.
- Under all conditions at the 4.5 A rate, core temperature rose less than 2 ˚C. This suggests that electrode temperatures are uniform at the 4.5 A rate.
- Initially the cell core temperature rises at a rate of 2, 6, 10 ˚C/Ah for 4.5, 9.0 and 13.5 A charges respectively. Between 0.5 and 3.0 Ah the temperature becomes more stable and remains within 1-2 ˚C. Deviations in this range may be a direct measurement of the irreversible heating evolution throughout the charge.

The relationship between radial temperature gradient and charge rate is expected to be nonlinear and dependant on charge current, electrode temperature, resistances, electrochemical gradients, and other factors. As the charge rate approaches zero, the temperature difference should be eliminated. As the current increases the radial temperature gradient is expected to nonlinearly increase as heat generation increases with current squared. The maximum radial temperature difference versus charge current for the three temperatures is given in Figure 50.

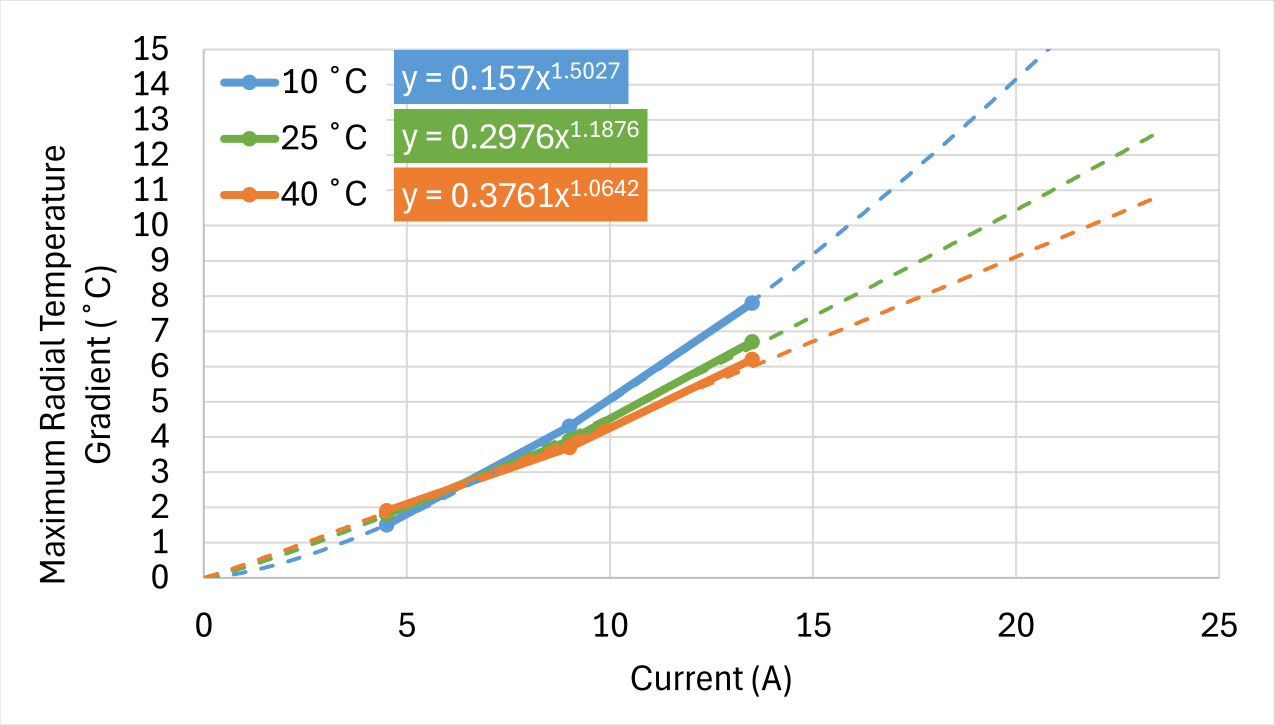

Figure 50 Maximum radial temperature gradient versus charge current for different temperatures

The trendlines in Figure 50 approximate the radial temperature gradient relationship to charge current to be exponential. The trendline equations give the exponents of 1.5, 1.2, and 1 for temperatures 10, 25 and 40 ˚C temperatures, respectively. This suggests that the higher the cell temperature, the less the radial temperature gradient increases with increasing current. Thus, increased cell temperature promotes more uniform cell temperature.

Further, the exponent of 1 for the 40 C case suggests a near linear relationship between radial temperature gradient and current. Quantifying the relationship by locally linearizing about the 9 A case results in a 0.70, 0.54 and 0.48 ˚C/A relationship at isothermal wall 10, 25 and 40 ˚C temperatures, respectively.

7.5 Conclusions

Significant wall temperature deviation from control setpoint was observed in the convection condition but not in the isothermal condition. Using an air chamber for isothermal testing is not recommended for high rates because it is not able to maintain cell wall and consequently internal temperature for parameterization purposes. Thus, traditional cell holders do not adequately control cell temperature when used to characterize key cell performance metrics at high currents.

Further, the results also show that the isothermal cell holder can maintain isothermal wall temperature even at ultra high charge rates. The internal temperature is 7.8 ˚C higher than wall temperature during data sheet rated 13.5 A charge at 10 ˚C. Increasing cell temperature was shown to reduce the radial temperature gradient.

Chapter 8 Conclusions and recommendations

This thesis used numerous characterization techniques to investigate high power cell performance response to ultra fast charge profiles. Three limiting factors to ultra fast charging were identified as lithium plating, maximum cell voltage, and temperature limitations. The research approach quantified cell material properties, measured performance under numerous charge conditions, evaluated how thermal control profiles impact charge performance, and measured the cell internal temperature during fast charges at different cell wall temperatures. Each evaluation technique provided new information useful for optimizing the charge session to improve fast charging of lithium ion cylindrical cells. Next, conclusions are summarized, their relevance during a charge session is contextualized, and recommendations for future work are described.

8.1 Conclusions

CC Stage temperature control

To improve charge time, the CC stage should end at a temperature greater than 45 ˚C which prevents reaching CV stage early. Heat generated during the CC phase could be used to elevate cell temperature and reduce reliance on external thermal control systems.

CV stage temperature control

The highest possible temperature should be achieved when using the CV stage to reach high states of charge quickly. Solid state ion diffusion in the active material is the limiting factor during CV stages and high temperatures improve diffusion. High temperatures prolong the CC stage and increase the average current in the CV stage resulting in reduced charge time overall. However, if the charge termination is set to equal to or less than 80 % SOC then heating above 45 ˚C will not significantly reduce charge time and high temperatures should be avoided. Selecting the thermal profile for optimized charging is highly dependent on charge termination conditions.

Temperature gradient

Cell charge time sensitivity in conditions between 10 to 35 ˚C and improved radial temperature gradient uniformity at elevated temperatures suggests that during the CC stage a radial temperature gradient based current limit should be applied especially as the cell passes through the sensitive temperature region. It is expected that accelerated degradation occurs when the cell operates with significant radial temperature gradient in the sensitive temperature region.

8.2 Recommendations

8.2.1 Develop plating model using measured material properties and in situ measurement of anode voltage

This thesis did not consider current limitations imposed by lithium plating. Future works should investigate how cell design influences the potential for lithium to plate at ultra fast rates and across dynamic temperature profiles. A model should be created to produce a charge current limit as a function of cell temperature and state of charge based on real cell material properties and verified with in situ measured anode potential. In situ anode reference voltage could be obtained with a reference electrode. Electrode half cell reference voltage curves can be obtained using samples of active materials to measure the active material loading ratio. Electrolyte saturation/depletion and concentration gradients should be considered. Electrolyte composition can be measured with gas chromatography -mass spectrometry.

8.2.2 Evaluate temperature gradient based degradation

Un-even electrode use contributing to accelerated degradation should be evaluated in the context of the radial temperature gradient. A degradation study which repeatedly cycles cells with and compares the degradation rate to the radial temperature gradient at different isothermal wall temperatures should be conducted. The study should determine if radial temperature gradient alone causes degradation or if the wall temperature is related to degradation. Further, the study should produce a current limit profile based on degradation caused by the radial temperature gradient or wall temperature.

8.2.3 Heat generation model

Heat generation in the CC phase is considerable at ultra-fast charge rates. Techniques for rapidly quantifying reversible and irreversible heat generation over wide range of temperatures and at ultra-fast charge rates should be developed to support investigating ways to optimize efficient cell temperature conditioning in the CC phase. The model should be verified experimentally then used to determine the most efficient thermal profile considering charge rate, initial temperature, termination SOC and temperature. One method to measure heat generation would be to drive Newtons law of cooling with measurements of the wall and core temperatures and measured radial thermal conductivity. This method may have considerable uncertainty. An improved heat generation measurement method would be to use an isothermal calorimeter. The isothermal cell holder used here could be adapted for this purpose.

8.2.4 Charge termination condition based thermal profile selection

This thesis quantified the relationship between basic thermal profiles and charge times from 0 to 100 % state of charge. A trade off model should be produced to select the optimal thermal profile based on initial temperature and state of charge for a range of charge termination conditions. Energy efficiency, degradation, and charge time should be considered and their sensitivity of impact evaluated.

An improved charge method could include preconditioning with a multistage thermal profile which is adapted to best suit charge conditions like initial temperature, start of charge SOC, end of charge SOC, and target charge time.

The first stage conditions the battery prior to the CC stage to minimize plating. The temperature requirement here is heavily dependant on cell design properties anode loading, electrolyte transport, and electrode resistance. The methods used here only considered a cell starting at 25 ˚C which is in a conditioned state in comparison to a cold soaked battery. Therefore, further research should be applied to quantify the relationship between temperature, charge current, and anode lithium plating risk across the spectrum of cell power design.

The second stage conditions the battery during CC charging for optimal CC to CV transition and CV stage performance. This thermal profile is similar to the adiabatic case investigated by (Teng Liu, 2021). Results in Chapter 5.3 suggest that for high SOC termination conditions, very high temperatures (60 ˚C) should be reached. For middle (50 %) to high SOC (90 %) termination conditions, moderate temperatures (45 ˚C+) should be reached depending on charge rate. This method where the bulk of the cell temperature increase is conducted within the CC stage could utilize heat generation within the cell to reduce thermal control system input and improve efficiency. Further, energy from fast charger could be used by the onboard thermal control system to transfer additional heat as required instead of using onboard energy on approach to the charger.

The third stage increases cell temperature to the maximum permissible during CV charging to high states of charge or begins cooling to reduce cell temperature if terminating charge below 80 %.

In summary, this work identified three different critical points during a charge session that impact charge performance and recommends optimizing the charging protocol with a multistage thermal profile which improves reduces degradation, improves charge time, and increases efficiency.

Bibliography

Ahmadian-Elmi, M. Z. (2024). Review of Thermal Management Strategies for Cylindrical Lithium-Ion Battery Packs. *Batteries*, 10.

Aiken, C. P. (2023). Tracking Electrolyte Motion in Cylindrical Li-ion Cells Using Moment of Inertia Measurements. *Journal of the Electrochemical Society*, 170.

Al-Hanahi, B. A. (2021). Charging Infrastructure for Commercial Electric Vehicles: Challenges and Future Works. *IEEE access*, 121476-121492.

Anastasiia, M. O. (2023). Resolving high potential structural deterioration in Ni-rich layered cathode materials for lithium-ion batteries operando. *Journal of Energy Storage*, 106211.

Bandhauer, S. G. (2011). A Critical Review of Thermal Issues in Lithium-Ion Batteries. *Electrochem*.

Bedürftig, B. O. (2021). Measuring the reversible heat of lithium-ion cells via current pulses for modeling of temperature dynamics. *Journal of Power Sources*, 506.

Bhoir, S. S. (2021). Experimental comparison of fast-charging protocols for NMC and NCA Li-ion batteries. *2021 IEEE Vehicle Power and Propulsion Conference*, -.

Bui, T. M. (2021). A Study of Reduced Battery Degradation Through State-of-Charge Pre-Conditioning for Vehicle-to-Grid Operations. . *IEEE Access*, 155871–155896. .

Carter, R. K. (2021). Directionality of thermal gradients in lithium-ion batteries dictates diverging degradation modes. *Cell Reports Physical Science*.

Cheng, Z. J. (2021). Direct Observation of Reversible Heat Absorption in Li-ion Battery Enabled by Ultra-Sensitive Thermometry. .

Chien, Y. L. (2023). Rapid determination of solid-state diffusion coefficients in Li-based batteries via intermittent current interruption method. *Nat Commun*, 14.

Colclasure, A. M. (2020). Electrode scale and electrolyte transport effects on extreme fast charging of lithium-ion cells. *Electrochimica Acta*.

Connor Madden, G. A. (2024). Inferring Battery Current Interrupt Device Activiation in a 18650 Cell under high C Discharge using a foil strain gauge. Columbia: ASNT Research Symposium.

Dae Sik Kim, Y. E. (2019). Improved fast charging capability of graphite anodes via amorphous Al2O3 coating for high power lithium ion batteries. *Journal of Power Sources*, 18-24.

Deep B Shah, H. K. (2019). Comparing Measurements of Limiting Current of Electrolytes with Theoretical Predictions up to the Solubility Limit. *Physical Chemistry*, 23872–23881.

Delong Ma, Z. C. (2014). Si-Based Anode Materials for Li0ion Batteries: A Mini Review. *Nano-Micro*, 347-358.

Drake, S. J. (2015). Heat generation rate measurement in a Li-ion cell at large C-rates through temperature and heat flux measurements. *Journal of Power Sources*, 266-273.

Dubarry, M. Q. (2018). Calendar aging of commercial Li-ion cells of different chemistries – A review. *Current Opinion in Electrochemistry*, 106-113.

Dubey, P. P. (2021). Direct Comparison of Immersion and Cold-Plate Based Cooling for Automotive Li-Ion Battery Modules. *Energies*, 14.

Edge, J. S. (2023). Lithium ion battery degradation: what you need to know. *Physical Chemistry Chemical Physics*, 8200-8221.

Edoardo, C. O. (2021). Experimental data of lithium-ion batteries under galvanostatic discharge tests at different rates and temperatures of operation). *In Science Letter*, 1504-15.

Ezahedi, S. E. (2024). Multi-cell sensorless internal temperature estimation based on electrochemical impedance spectroscopy with Gaussian process regression for lithium-ion batteries safety. *Journal of Energy Storage*, 94.

Eze, C. Z. (2024). Numerical heat generation analysis of the tabbed and novel tabless designs of cylindrical-type lithium-ion batteries. *Applied Thermal Engineering*, 246.

Garcia-Araez., B. R. (2020). A review of gas evolution in lithium ion batteries. *Energy Reports 6*, 10-18.

Gottschalk, L. S. (2023). Influence of different anode active materials and blends on the performance and fast-charging capability of lithium-ion battery cells. *Journal of Energy Storage*, 107706-.

Gulsoy, B. V. (2022). In-situ temperature monitoring of a lithium-ion battery using an embedded thermocouple for smart battery applications. *Journal of Energy Storage*, 105260.

Hanlei Zhang, O. K. (2017). Atomic Insight into the Layered/Spinel Phase Transformation in Charged LiNi0.80Co0.15Al0.05O2 Cathode Particles. *J. Phys. Chem*, 1421-1430.

Haregewoin, A. M. (2016). Electrolyte additives for lithium ion battery electrodes. *Energy & Environmental Science*, 1955-1988.

Harlow, J. E. (2019). A wide range of testing results on an excellent lithium-ion cell chemistry to be used as benchmarks for new battery technologies. *Journal of The Electrochemical Society*, A3031.

Hill, N. R. (2023). *Research for TRAN Committee – Environmental challenges through the.* Brussels: European Parliament, Policy Department for Structural and Cohesion Policies.

Howel, D. e. (2017). Enabling fast charging: A technology gap assessment. *Energy*, 3949-3954.

Hyeon, C.-W. K.-Y.-E. (2022). Thin-shelled hollow mesoporous TiO2 spheres with less tortuosity as fast-charging anode. *Coposites. Part B, Engineering*, 111760.

J. Asenbauer, T. E. (2020). The success story of graphite as a lithium-ion anode material – fundamentals, remaining challenges, and recent developments including silicon (oxide) composites. *Sustainable Engineering*, 4387-4416.

Ji, Y. (2013). Li-Ion Cell Operation at Low Temperatures. *The Electrochemical Society*, 636-649.

Jin, Z. C. (2021). Understanding the correlation between microstructure and electrochemical performance of hybridized pitch cokes for lithium-ion battery through tailoring their evolutional structures from ordered soft carbon to disordered hard carbon. . *Journal of Alloys and Compounds*, 887.

Juarez-Robles, D. A. (2021). Degradation-safety analytics in lithium-ion cells and modules part II. Overcharge and external short circuit scenarios. *Journal of The Electrochemical Society*, 168-173.

Kandler Smith, P. G. (2021). Lithium-Ion Battery Life Model with Electrode Cracking and Early-Life Break-in Processes. *Journal of the Electrochemical Society*, 168.

Kraft, L. (2021). Comparative Evaluation of LMR-NCM and NCA Cathode Active Materials in Multilayer Lithium-Ion Pouch Cells: Part II. Rate Capability, Long-Term Stability, and Thermal Behavior. *Electrochem*, 168.

Kumar, P. A. (2023). A review on anode materials for lithium/sodium-ion batteries. *Journal of Energy Chemistry*, 509–540.

Lain, M. J. (2019). Design Strategies for High Power vs. High Energy. *Batteries (Basel)*, 64-.

Lain, M. J. (2021). Understanding the limitations of lithium ion batteries at high rates. *Journal of Power Sources*, 229690.

Landini, T. S. (2022). Experimental investigation of lithium-ion cells ageing under isothermal conditions for optimal lifetime performance. *Journal of energy storage*.

Li, R. L. (2022). Effect of external pressure and internal stress on battery performance and lifespan. *Energy Storage Materials*, 395-429.

Li, S. K. (2021). Optimal cell tab design and cooling strategy for cylindrical lithium-ion batteries. *Journal of Power Sources*, 492.

Masias, A. M. (2021). Opportunities and challenges of batteries in automotive applications. *ACS Energy*, 621-630.

Michelbacher, C. J. (2017). *Enabling Fast Charging: A Technology Gap Assessment.* United Kingdom: OSTI.

Minseok, S. Y.-Y. (2022). Modeling and Analysis of Heat Generation Rate of a Large Format Pouch-Type Lithium-Ion Battery Considering Degradation. *Journal of The Electrochemical Society*, 169.

Molicel. (2020). *INR21700 P45B datasheet.* Mapleridge: Molicel.

Myall, D. I. (2018). Accelerated Reported Battery Capacity Loss in 30 kWh Variants of the Nissan Leaf. *Preprints*.

Ohneseit, S. F. (2023). Thermal and Mechanical Safety Assessment of Type 21700 Lithium-Ion Batteries with NMC, NCA and LFP Cathodes–Investigation of Cell Abuse by Means of Accelerating Rate Calorimetry (ARC). *Batteries*, 237.

Preger, Y. B.-K. (2020). Degradation of commercial lithium-ion cells as a function of chemistry and cycling conditions. *Journal of The Electrochemcial Society*, 167-179.

R. Tian, S.-H. P. (2019). Quantifying the factors limiting rate performance in battery electrodes. *Nat Commun*, 41467.

Sabri Baazouzi, N. F. (2023). Design, Properties, and Manufacturing of Cylindrical Li-Ion Battery Cells—A Generic Overview. *Batteries* , 309.

SAE, H. -E. (2021, 12 15). *Megawatt Charging System for Electric Vehicles*. Retrieved from SAE.org: https://www.sae.org/standards/content/j3271/

Schmitt, J. M. (2017). Impedance change and capacity fade of lithium nickel manganese cobalt oxide-based batteries during calendar aging. *Journal of Power Sources,*, 183-194.

Sehrawat, P. S. (2021). Recent trends in silicon/graphene nanocomposite anodes for lithium-ion batteries. . *Journal of Power Sources,*, 229709.

Sehrawat, P. S. (2021). Recent trends in silicon/graphene nanocomposite anodes for lithium-ion batteries., . *Journal of Power Sources*, 229709-.

Sheng, L. Z. (2025). Quantitative measurement of thermal performance of a cylindrical lithium-ion battery. *Journal of the International Measurement Confederation*, 239.

Sieg, J. B. (2019). Fast charging of an electric vehicle lithium-ion battery at the limit of the lithium deposition process. *Journal of Power Sources*, 427.

Singh, P. D. (2022). Electrochemical performance of NCA based cathodes for variable thickness of electrode through modelling and simulation. . *Materials Today : Proceedings*, 3742–3748.

Suarez, C. &. (2019). Fast and Ultra-Fast Charging for Battery Electric Vehicles - A Review. *IEEE Energy Conversion Congress and Exposition* (pp. 569–575). Baltimore, MD, USA: IEEE.

T. Raj, A. A. (2020). Investigation of Path-Dependent Degradation in Lithium-Ion Batteries. *Batteries & Supercaps*, 1377.

Teng Liu, S. G.-G.-Y. (2021). Effect of thermal environments on fast charging Li-ion batteries. *Journal of power sources*.

Thakur, A. K. (2023). A state-of-the art review on advancing battery thermal management systems for fast-charging. *Applied Thermal Engineering*, 226.

Thusitha, T. A. (2022). The next generation of fast charging methods for Lithium-ion batteries: The natural current-absorption methods. *Renewable and Sustainable Energy Reviews*, 112338.

Tian, R. A. (2020). Quantifying the effect of electronic conductivity on the rate performance of nanocomposite battery electrodes. *ACS Applied Energy Materials*, 2966-2974.

Todys, G. M. (2020). *"Thermal characterization of a cylindrical Li-ion battery cell.".* Gothenburg: Chalmers.

Tu, H. F. (2019). Extreme Fast Charging of Electric Vehicles: A Technology Overview. *IEEE Transactions on Transportation Electrification*, 861-878.

Vincent, B. G. (2021). Development of an in-vehicle power line communication network with in-situ instrumented smart cells. *Transportation Engineering*, 100098.

Waldmann, T. S.-M. (2023). Effects of Tab Design in 21700 Li-Ion Cells: Improvements of Cell Impedance, Rate Capability, and Cycling Aging. *Energy Technology*, 11.

Wang, C. Y. (2022). Fast charging of energy-dense lithium-ion batteries. *Nature 611*, 485-490.

Wenlong Xie, Z. Z. (2024). Understanding the limitations of thick electrodes on the rate capability of high-energy density lithium-ion batteries. *Electrochemica Acta*.

X. G. Yang, Y. L. (2017). Modeling of lithium plating induced aging of lithium-ion batteries: Transition from linear to nonlinear aging. *J. Power Sources*, 28-40.

Xiao-Guang Yang, Y. L.-Y. (2017). Modeling of lithium plating induced aging of lithium-ion batteries: Transition from linear to nonlinear aging. *Journal of Power Sources*, 28-40.

Yang, G. L. (2013). Real-time temperature measurement with fiber Bragg sensors in lithium batteries for safety usage. *Measurement: Journal of the International Measurement Confederation*, 3166-3172.

Yang, X. G. (2017). Modeling of lithium plating induced aging of lithium-ion batteries: Transition from linear to nonlinear aging. *Journal of Power Sources*, 28-40.

Zhang, S. S. (2020). Identifying rate limitation and a guide to design of fast-charging Li-ion battery. InfoMat, 2(5), . *InfoMat*, 942-949.

Appendix A Supplemental data

Total Charge Time (Min)		Temperature (˚C)				
		25	35	45	55	65
Rate (A)	4.5	79.3	74.0	70.4	65.7	64.7
	13.5	50.6	42.7	37.4	31.5	30.0
	17	46.4	39.5	30.2	28.1	26.9
	23	45.4	34.8	28.2	25.8	24.3
	27	36.6	30.6	27.1	24.7	23.2

CV Charge Time (Min)		Temperature (˚C)				
		25	35	45	55	65
Rate (A)	4.5	27.65	19.47	15.18	10.02	9.17
	13.5	36.70	27.90	22.22	16.07	14.60
	17	36.17	28.40	18.77	16.48	15.32
	23	38.87	27.55	19.87	17.97	16.43
	27	31.88	25.28	21.40	18.70	16.98

CC Charge Time (Min)		Temperature (˚C)				
		25	35	45	55	65
Rate (A)	4.5	51.68	54.52	55.25	55.67	55.53
	13.5	13.88	14.78	15.17	15.37	15.35
	17	10.17	11.05	11.42	11.63	11.60
	23	6.52	7.22	7.58	7.87	7.87
	27	4.68	5.30	5.72	6.02	6.22

CC/CV Charge Capacity Ratio (-)		Temperature (˚C)				
		25	35	45	55	65
Rate (A)	4.5	100.0	100.0	100.0	100.0	100.0
	13.5	91.1	95.6	98.0	99.6	100.0
	17	84.3	90.1	93.1	95.1	95.9
	23	73.2	79.5	83.9	86.8	88.1
	27	63.8	70.9	75.9	79.6	82.1

Cycle En Eff (%)		Temperature (˚C)				
		25	35	45	55	65
Rate (A)	4.5	94.36	94.98	95.65	95.69	96.03
	13.5	91.70	92.68	93.22	93.72	94.11
	17	91.03	91.90	92.48	93.12	93.39
	23	89.76	90.83	91.31	91.85	92.26
	27	89.17	90.07	90.77	91.26	91.60

Appendix B Neware Cycler CT-4008 BTS-5V50A properties

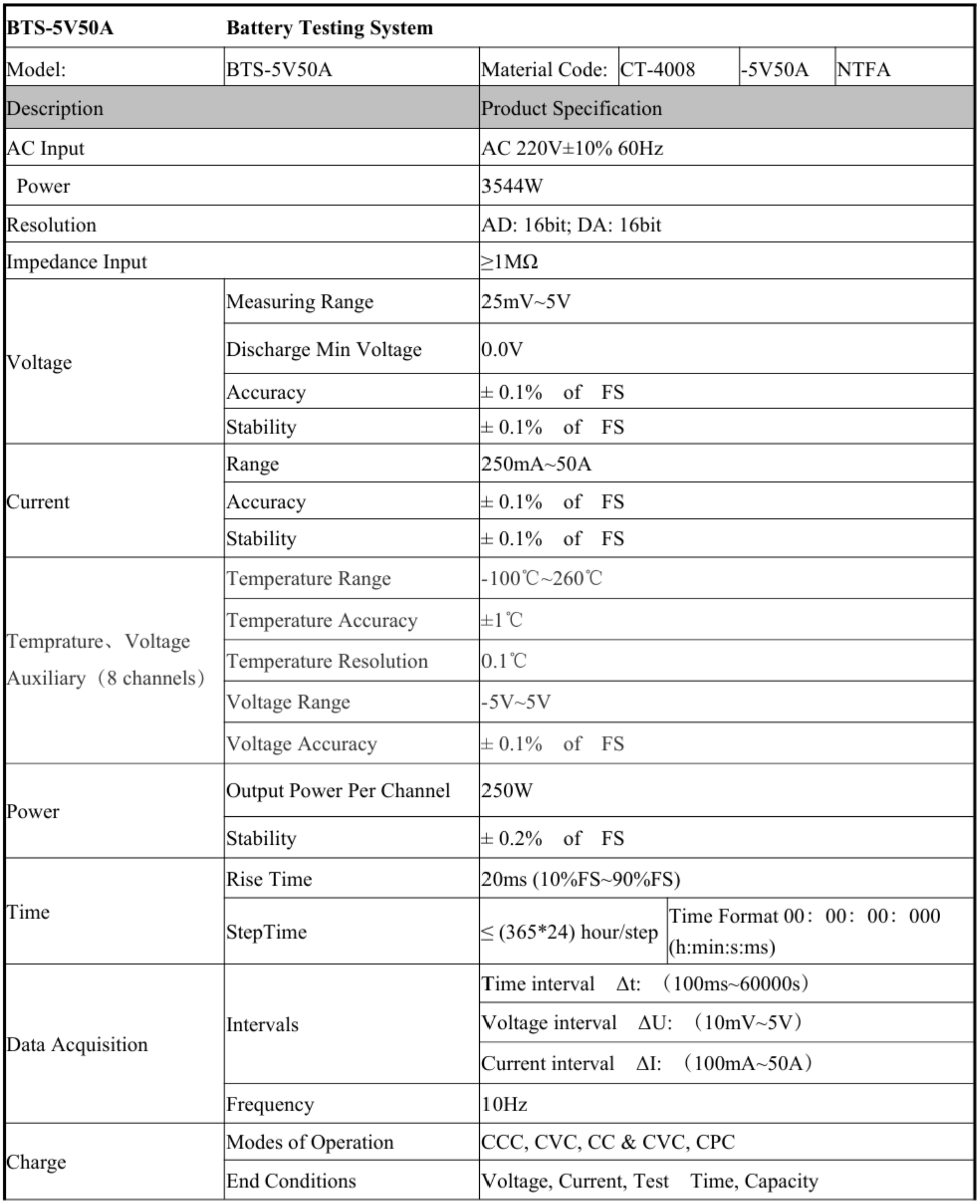

BTS-5V50A	**Battery Testing System**		
Model:	BTS-5V50A	Material Code:	CT-4008 -5V50A NTFA
Description		Product Specification	
AC Input		AC 220V±10% 60Hz	
Power		3544W	
Resolution		AD: 16bit; DA: 16bit	
Impedance Input		≥1MΩ	
Voltage	Measuring Range	25mV~5V	
	Discharge Min Voltage	0.0V	
	Accuracy	± 0.1% of FS	
	Stability	± 0.1% of FS	
Current	Range	250mA~50A	
	Accuracy	± 0.1% of FS	
	Stability	± 0.1% of FS	
Temprature、Voltage Auxiliary（8 channels）	Temperature Range	-100℃~260℃	
	Temperature Accuracy	±1℃	
	Temperature Resolution	0.1℃	
	Voltage Range	-5V~5V	
	Voltage Accuracy	± 0.1% of FS	
Power	Output Power Per Channel	250W	
	Stability	± 0.2% of FS	
Time	Rise Time	20ms (10%FS~90%FS)	
	StepTime	≤ (365*24) hour/step	Time Format 00：00：00：000 (h:min:s:ms)
Data Acquisition	Intervals	Time interval Δt: （100ms~60000s）	
		Voltage interval ΔU: （10mV~5V）	
		Current interval ΔI: （100mA~50A）	
	Frequency	10Hz	
Charge	Modes of Operation	CCC, CVC, CC & CVC, CPC	
	End Conditions	Voltage, Current, Test Time, Capacity	

Appendix C Figure Copyright license

Figure #	Source	Publisher	License #
2A	(Ezahedi, 2024)	Elsevier	5925630139945
2B	(Yang G. L., 2013)	Elsevier	5925630843629
2C	(Vincent, 2021)	Elsevier	5925631216423
2D	(Gulsoy, 2022)	Elsevier	OPEN ACCESS
3	(Thusitha, 2022)	Elsevier	OPEN ACCESS
4	(Minseok, 2022)	Elsevier	OPEN ACCESS
8	(Waldmann, 2023)	Wiley	OPEN ACCESS
9,10	(Colclasure, 2020)	Elsevier	OPEN ACCESS
11	(Deep B Shah, 2019)	American Chemical Society	OPEN ACCESS
12	(Lain M. J., 2019)	Elsevier	OPEN ACCESS
13	(Teng Liu, 2021)	Elsevier	OPEN ACCESS
14	(Thusitha, 2022)	Elsevier	OPEN ACCESS